

SATELLITE INSTRUMENTS
USING SOLID STATE DETECTORS *

by

R. Walker Fillius **

A thesis submitted in partial fulfillment of the
requirements for the degree of Master of Science
in the Department of Physics and Astronomy
in the Graduate College of the State
University of Iowa

August, 1963

Chairman: Professor J. A. Van Allen

* Research supported in part by the National Aeronautics and
Space Administration under grants NAS5-1683 and NAS5-2054.

** Research Fellow, National Aeronautics and Space Administration.

ACKNOWLEDGEMENTS

The author is sincerely grateful to Dr. Carl McIlwain who proposed these detectors and supervised the design of the Relay instruments. Thanks are also due to Dr. James A. Van Allen who directed the EOGO experiment and made this work possible.

Many associates, students, and staff members took part in various aspects of the detector development and calibration. Mr. D. C. Enemark designed all the electrical circuitry and contributed greatly in informal discussions. Staff members G. E. Frohwein, D. L. Chinburg, R. L. Trachta, and E. D. Lawrence handled the mechanical design and many administrative matters. The association with Mr. C. D. Crandall was both friendly and helpful. As an electronics technician Mr. E. W. Strein has done excellent work on the EOGO instrument, and B. A. Randall has handled the task of constructing the foils. Dr. H. Sauer was kind enough to write a computer program for calculating multiple coincidence counting rates. Students who have given their time to operate or assist with accelerators and in the calibrations are D. W. Heikkinen, J. Davidson, J. D. Craven, and R. D. Campbell.

Special thanks are due to the University of Minnesota Linac group for the gift of time on their accelerator. Drs. John Williams and R. P. Featherstone, and Mr. Richard Carlson were very helpful.

1 9983

ABSTRACT

A

Solid state detectors are described which have been used as proton counters in the earth's radiation belts. In a design for low energy protons a single detector does pulse height analysis to classify energies down to $\frac{1}{2}$ MeV. Electrons are eliminated by a combination of thin detector, high discrimination levels, and fast-clipping pulse amplifier. A two-element telescope counts higher energy protons and classifies them in energy ranges from 18 to 60 MeV. The characteristics of solid state detectors and their requisite electronics are discussed, along with the design and calibration of the satellite instruments.

Author

TABLE OF CONTENTS

Chapter	Page
I. Introduction	1
II. The Solid State Detector	3
1. The Space Charge Region	3
2. The Interaction of Charged Particles with Matter:	9
3. Charge Collection, Detector Characteristics, and Diffusion Collection	12
4. Similar Detectors and Specialized Configurations	18
(a) P-N Junction Detectors	18
(b) Lithium-Drift Detectors	19
(c) Totally Depleted Detectors	22
(d) Thin Detectors for Heavy Particle Selection	23
III. Electronic Requirements and Data Systems	26
1. The Charge-Sensitive Amplifier	26
2. Preamplifier Calibration	29
3. Pulse-Shaping and Noise Performance	31
4. Particle Counting and Energy Analysis	34

TABLE OF CONTENTS
(continued)

Chapter	Page
IV. A Single-Element Proton Detector	41
1. Design Features	42
(a) Shielding	42
(b) Geometric Factor	46
(c) Elimination of Electrons	47
(d) Discrimination Levels	49
(e) On-Board Source	51
(f) Light-Tight Foils	52
2. Proton Calibrations	54
(a) Determination of Depletion Depth	54
(b) Energy Ranges	55
3. Response to Electrons	57
(a) A Model for Multiple Coincidence Pileup ...	59
(b) Verification of the Model	63
V. A Two-Element Proton Telescope	65
1. Directionality	65
2. Proton Energy Analysis	66
3. Determination of Detector Parameters	69
4. Calibration in a High-Energy Beam	73

TABLE OF CONTENTS
(continued)

Chapter	Page
VI. Detector Summary and Flight Data	76
1. Detector and Flight Review	76
2. The Relay Magnetometer Scheme	78
3. Relay Flight Data	79
Bibliography	81
Figure Captions	86
Figures 1-37	88-123

TABLE OF TABLES

Table No.		Page
I (a)	Relay Detector B: Design-Center Pulse-Height Channels and Energy Ranges	38
I (b)	EOGO Detector H: Design-Center Pulse-Height Channels and Energy Ranges	39
II	Relay Detector B, Unit 2 Calibrated Pulse-Height Channels and Energy Ranges .	58

I. INTRODUCTION

The discovery of the Van Allen radiation belts revealed that there was a great deal to be measured in space near the earth, and many experiments have since been launched to carry out the exploration. The first investigations were naturally of a rough nature, to learn the spatial extent, intensity, and general character of the radiation. On the basis of the knowledge they have gained, it has become possible to design more sophisticated instruments to gather more refined information. The identification of the particles present, measurement of their energy spectra and intensities, the variation of these quantities with position and time, and their correlation with other geophysical events are current experimental goals.

The Geiger tube, the most successful detector in the exploratory probes, is not sufficiently versatile to meet all of these demands, and experimenters have had to find more selective detectors. One of these new detectors is the solid state diode, or p-n junction. The solid state diode is a recent product of semiconductor technology and research, but it is already the most popular detector in the field of low-energy nuclear physics.

Unlike the Geiger tube, which produces a uniform pulse for ionizing radiation of any kind, the semiconductor diode produces a pulse whose height is related to the particle type and energy. The energy resolution of the device is surpassed only by large magnetic spectrometers, which are clearly unsuitable to fly in a satellite. Furthermore, under selected conditions, a solid state diode can be made to respond to particles of one type, such as protons, while ignoring other, lesser ionizing particles, such as electrons. Advantages gratifying to the satellite engineer are its light weight, small size, versatility of packaging, lack of magnetic-field restrictions, and low voltage and power requirements.

It is believed that the first successful satellite-borne solid state detector was that developed by G. F. Pieper of the Johns Hopkins University Applied Physics Laboratory and flown aboard the State University of Iowa satellite Injun I [Pieper, Zmuda, Bostrom, and O'Brien, 1962]. Other groups to fly solid state detectors have included the Bell Telephone Laboratories [Brown and Gabbe, 1963], the University of California Lawrence Radiation Laboratory [Bloom, Mann, and West, 1961], and the University of Chicago Laboratories for Applied Sciences [Takaki, Perkins, and Tuzzolino, 1961]. This paper will describe the solid-state detector packages which have been developed at the State University of Iowa for the Relay and

EOGO satellites. One Relay satellite has been orbited, with its detector complement working faultlessly. A second and possibly a third Relay launch are planned for the future, and the first EOGO is scheduled for mid-1964. Solid state detectors of like design have been proposed for several future spacecraft, and, thanks to their versatility, are likely to be adapted to many more projects to come.

II. THE SOLID STATE DIODE DETECTOR

The properties of solid state detectors are familiar to most experimenters and are thoroughly covered in the literature [Asheville Conference, 1961; Gatlinburg Conference, 1961; Seventh Scintillation Counter Symposium, 1960; Eighth Scintillation Counter Symposium, 1962; and Symposium on Space Phenomena and Measurement, 1963]. For those having no experience with the devices, a rudimentary explanation will be necessary to understand the applications described here. Such an account follows, the material being selected for our specialized considerations alone.

1. The Space Charge Region
[Brown, 1961A; Statz, 1961;
and Fox, 1961].

A surface-barrier detector is normally made [Fox, 1961] from a piece of n-type silicon. An ohmic contact is made to the back, and the front surface is treated to produce surface states, that is, electrons bound in localized energy levels at the surface. A very thin ($75\mu\text{ gm/cm}^2$) layer of gold is flashed to the front surface to provide electrical contact. Figure 1 (a) shows schematically the conduction and valence bands and the charge distribution in such

a device in cross-sectional perspective. The surface states trap the conduction band electrons immediately beneath the surface, leaving a region of positive donor ions to equalize the charge. The repulsive potential of the surface charge bends the energy bands upwards, and gives rise to an intrinsic barrier potential, ϕ_o , between the front and back contacts.

Figure 1 (b) shows the effect of applying a positive external voltage ϕ_a to the back contact. This polarity back-biases the diode, drawing the conduction band electrons farther away from the front and depositing more negative charge on the surface. The electrons will drift toward the back until the electric field falls to zero. The distance at which this occurs is called the depletion depth, and the region devoid of electrons is called the electron depletion region or the space charge region.

It is a simple matter to calculate the electric field as a function of distance and derive a formula for the depletion depth. The geometry is shown in Figure 2 (a), where χ , the space charge density, is equal to the donor concentration times the absolute value of the electronic charge: $\chi = N_d |e|$. Integrate the first Maxwell equation

$$\nabla \cdot \vec{D} = q \quad (1)$$

over the Gaussian surface shown, and use the constitutive relation

$$\vec{D} = \epsilon \vec{E} . \quad (2)$$

The surface integral is zero over sides I, II, and III, and on side IV it is

$$\int \vec{D} (x) \cdot d\vec{A} = - A \epsilon E (x) .$$

The charge enclosed by the volume is $\sigma A + \chi Ax$. Thus

$$- E (x) = \frac{\sigma}{\epsilon} + \frac{\chi x}{\epsilon} . \quad (3)$$

The boundary condition is that

$$E (d) = 0 . \quad (4)$$

This gives

$$\sigma = - \chi d , \quad (5)$$

$$E (x) = \frac{\chi}{\epsilon} (d-x) . \quad (6)$$

Equation (5) shows that the space charge just cancels the surface charge, and equation (6) gives the electric field profile in the space charge region. The potential

$$\phi = \phi_o + \phi_a$$

is related to these parameters by the integral

$$\phi = \int_0^d E(x) dx = \frac{\chi}{\epsilon} \frac{d^2}{2} \quad (7)$$

and the potential distribution is given by

$$\phi(x) = \int_0^x E(x) dx = \phi - \frac{\chi}{2\epsilon} (d-x)^2. \quad (8)$$

The potential and potential gradient are drawn in Figures 2 (b) and 2 (c). Equation (7) gives the key formula for the depletion depth,

$$d = \left[\frac{2\epsilon\phi}{N_d |e|} \right]^{1/2} = \sqrt{2\mu\epsilon} (\rho\phi)^{1/2} \quad (9)$$

where the resistivity, ρ has been introduced:

$$\rho = \frac{1}{N_d |e| \mu} = \frac{1}{N_n |e| \mu}$$

(μ = electron mobility)

(N_n = electron concentration)

[Sproull, 1956].

This equation shows that, for a given material, the depletion depth may be varied by changing the potential. The variability of the depletion depth is one of the useful features of the solid state diode.

Another important parameter of the space charge region is the dynamic, or small-signal, capacitance, measured with an applied voltage already on the detector:

$$C = \frac{dQ}{dV} .$$

The charge on the front electrode is σA , and the voltage, referred to the back, is $-\phi$. Using equations (5) and (7), we can write the voltage at this electrode as a function of charge:

$$V = - \frac{\sigma^2}{2 \epsilon} = - \frac{(\sigma A)^2}{2 \epsilon A^2} \quad (10)$$

$$\frac{dV}{d(\sigma A)} = - \frac{(\sigma A)}{\chi \epsilon A^2} = \frac{d}{\epsilon A} .$$

Therefore

$$C = \frac{\epsilon A}{d} . \quad (11)$$

It is a useful memory device to note that this is the formula for the total capacitance of a parallel plate condenser. The electrostatic configuration is not the same, though, and it is not correct to "derive" the detector capacitance as a simple application of the parallel plate formula.

Equations (9) and (11) are used often and are repeated below for numerical calculations.

$$\text{p-type silicon: } d \text{ (microns)} = 0.3 \sqrt{\rho \text{ (ohm-cm)} \phi \text{ (volts)}} \quad (9a)$$

$$\text{n-type silicon: } d \text{ (microns)} = 0.5 \sqrt{\rho \text{ (ohm-cm)} \phi \text{ (volts)}} \quad (9b)$$

$$C = 1.06 \times 10^4 \frac{A \text{ (cm}^2\text{)}}{d \text{ (microns)}} . \quad (11a)$$

The following constants have been used [Blankenship and Borkowski, 1960; Brown, 1961A]:

$$\mu_n = 1200 \text{ cm}^2/\text{volt-sec}$$

$$\mu_p = 450 \text{ cm}^2/\text{volt-sec}$$

$$\frac{\epsilon}{\epsilon_0} = 12 .$$

The electric field also deserves consideration in detector applications [Brown, 1961B]. Equation (6) can be rewritten in terms of the potential, giving

$$E = \frac{2\phi}{d^2} (d-x) . \quad (6a)$$

At the surface

$$E_0 = \frac{2\phi}{d} . \quad (6b)$$

These equations are easily solved with the aid of a nomograph.

Figure 3 is a Silicon Diode Nomograph similar to that of Blankenship [1960]. The dotted line shows a typical example: An n-type detector of 3000 ohm-cm material biased to 200 volts has a depletion depth of 400 microns and a surface electric field of 10,000 volts/cm. This graph sums up the properties of the space charge region and is very useful for detector design.

2. The Interaction of Charged Particles with Matter.

It has not yet been shown here that this device will act as a charged particle detector. To understand how this comes about, one must consider what happens when a charged particle bombards a detector. The subject is well understood and has been successfully treated theoretically and experimentally. Reviews that have been written on the subject include Bethe and Ashkin [1953], W. Whaling [1958], and Katz and Penfold [1952]. Elementary treatments can be found in such textbooks as Green, Nuclear Physics [1955], and Leighton, Principles of Modern Physics [1959]. This paper will merely state their results and exhibit graphs which can be used for calculations.

For charged particles in a broad energy range, 0.1 to 1000 MeV, there is only one process to be considered: the coulomb interaction

between the primary particle and individual electrons in the material. Such encounters result in the transfer of energy from the primary particle to the electrons, exciting and ionizing atoms of the absorber and slowing down the energetic primary. Heavy particles of energy above 1 BeV suffer additional energy loss by Cerenkov radiation and bremsstrahlung, and positive ions below 100 keV exhibit less efficient loss because of charge exchange interactions, in which electrons from the absorber attach themselves to the primary and screen its charge.

For heavy charged particles, the rate of energy loss from ionization and excitation is expressed analytically by the following formula [Green, 1955]:

$$-\frac{dE}{dx} = \frac{4\pi e^4 z^2}{m v^2} \frac{N_A \rho Z}{A} \left\{ \log \frac{2m v^2}{I} - \log(1-\beta^2) - \beta^2 \right\}$$

$$I \approx K Z$$

(12)

where e = the charge of an electron
 m = the mass of an electron
 z = the charge of the primary particle
 v = the velocity of the primary particle
 β = v/c
 N_A = Avogadro's number

ρ = the absorber density
 Z = the atomic number of the absorber
 A = the atomic weight of the absorber

Several features are notable:

1. The only parameters of the incident particle are its charge and velocity.
2. If one divides through by ρ and defines a new length unit $x' = \rho x$ (expressed in gram-cm⁻²), the formula becomes rather insensitive to the type of absorber. The absorber now enters only in the terms Z/A , which decreases slightly at high Z , and I , which also causes a small decrease for higher Z .
3. The dependence on the incident particle energy is close to E^{-1} for low energies, and becomes less steep as the relativistic terms enter. At an energy near the particle's rest-mass energy there is a minimum followed by a slight rise to a plateau. The divergence indicated by the formula for very high energies does not occur because of other physical effects not included in this theory.

The last two features are illustrated by Figure 4 which shows dE/dx vs E for protons in several materials. The dropoff at low energy is due to the charge-exchange interaction named earlier.

It is often important to know how far a particle of a given initial energy will travel before it is brought to a stop. This

distance is called the particle range and can be calculated by integrating equation (12):

$$R(E) = \int_E^0 - \left(\frac{dE'}{dx} \right)^{-1} dE' . \quad (13)$$

Figure 5 shows curves of $R(E)$ vs E for several types of particles in different absorbers. Calculations for silicon detectors can be done using the aluminum curve because of the small difference in Z and A for these elements.

3. Charge Collection, Detector Characteristics, and Diffusion Collection.

Graphs like Figures 4 and 5 can be used to calculate how much energy a charged particle will lose in a detector of any given dimensions. This energy goes into ionization and excitation of absorber atoms, and, in semiconductor materials, the creation of hole-electron pairs. The amount of energy required to create pairs in silicon has been measured with bombarding particles ranging from 20 keV electrons to 200 MeV heavy ions [Bromley, 1961]. The production rate is one pair for every 3.5 eV [Brown, 1961B] lost

by the primary particle, and it is the same for all particles and all energies. This is one of the most important facts associated with the solid state detector for it enables one to relate the amount of energy lost in a crystal and the number of carriers produced.

Measuring the number of carriers created in a given volume of silicon thus determines the amount of radiation striking the material. Early crystal counters had no rectifying barrier, and merely consisted of a block of crystal with electrodes at opposite ends. A voltage impressed between the electrodes caused the carriers to drift in the electric field until they reached the electrodes or recombined. By measuring the pulses produced by the radiation one could estimate the intensity in the crystal. These devices had several defects [Mayer, 1961; Brown, 1961B] resulting from the low electric field obtainable between the electrodes. Charges polarized along the track of a particle, cancelling the impressed field. The collection was very slow; and recombination occurred between carriers, so that calibration was difficult.

Refer to Figure 2 (b), showing the electric field distribution across a back-biased diode. The field is extremely high in the space-charge region, typically 10^3 or 10^4 volts/cm. Radiation-

produced carriers are snatched apart by the field and collected instantly ($< 10^{-8}$ sec), before recombination can take place. Thus a charged particle moving through the space charge region produces a pulse of charge proportional to the energy lost in the region.

As a first approximation one can consider the collection efficiency in a diode detector to be 100% in the space charge region and zero elsewhere [Brown, 1961B; Mayer, 1961]. Then the charge pulse produced by a particle moving along the x-axis is given by

$$Q = \frac{1.6 \times 10^{-19}}{3.5} \int_0^d \left(- \frac{dE}{dx} \right) dx . \quad (14)$$

The above equation gives the pulse height in coulombs. It is usual to express the pulse in energy units simply as the integral,

$$P = \int_0^d \left(- \frac{dE}{dx} \right) dx . \quad (15)$$

A detector characteristic curve gives the pulse height as a function of initial energy for a given particle type. A family of characteristic curves is shown in Figure 6 for protons in detectors of the indicated depletion depths. A characteristic curve

has two distinct parts. The first part is the output from particles whose range is less than the detector depletion depth. Figure 7a depicts this case. The particle loses all of its energy in the space charge region, and equation (15) becomes

$$P = \int_0^R \left(- \frac{dE}{dx} \right) dx = E. \quad (16)$$

The pulse output is equal to the particle energy, and the characteristic is linear. As this is an extremely desirable case, there is much effort to produce deeper detectors which will stop faster particles.

The other part of the characteristic arises from particles which penetrate the depletion region (Figure 7b). In this case the integral in equation (15) has to be evaluated. The upper limit of the integral is d for particles incident head-on, but for particles incident at an angle θ the limit becomes $d' = d \sec \theta$ (Figure 7c). Therefore the second part of the characteristic curve is usable only if θ is uniform. Because of this restriction the detector must be made directional for the analysis of penetrating particles.

The assumption was made in equation (15) that the charge collection efficiency was 100% in the space charge region and zero

elsewhere. In actual practice this is not the case. Carriers produced beyond the depletion depth will diffuse about for many microseconds before recombining [Brown, 1961B; Mayer, 1961]. If their random paths should take them into the space charge region, they will be snapped up and will contribute to the pulse height. To be accurate, then, one should consider a collection efficiency, $\epsilon(x)$, as drawn in Figure 8 [Amsel, 1961]. The pulse height caused by a penetrating particle will be given by

$$P = \int_0^{\infty} \left(- \frac{dE}{dx} \right) \epsilon(x) dx . \quad (17)$$

In practice, however, determining the efficiency is too difficult to be worthwhile, and so one uses an idealized efficiency with empirical corrections.

The amount of diffusion collection which takes place will be partly determined by the pulse-amplifying circuitry [Amsel, 1961]. If the amplifier responds to charge arriving long after the initial rising edge of the pulse, as does a slow-clipping amplifier, the collection efficiency will be high. If, on the other hand, the electronics amplifies only the fast initial step, the diffusion collection will be decreased.

The occurrence of diffusion collection is evident in Figure 9. The depletion depth of a detector was varied by changing the applied voltage, and pulse heights monitored for 6.05 and 8.78 MeV alpha particles from a Thorium source. At a high applied voltage the depletion depth is greater than the particle ranges, and the total energies are collected (equation (16)). As the depletion depth is lowered below the particle range, the output pulse given by equation (17) is reduced. The first-approximation pulse height, equation (15), has been calculated over this range of d for comparison. Three curves can be traced for each alpha energy. The first shows the idealized pulse height, or the energy deposited up to but not beyond the depth d . The second shows the pulse height observed by a fast-clipping amplifier having a fall time of about 0.1 microsecond, and the third shows the pulse height observed by a slower-clipping amplifier, with a fall time of about 3 microseconds. As expected, the slow-clipping amplifier gives a higher pulse for penetrating particles than does the fast-clipping amplifier and, as fast as it is, the latter amplifier produces a higher pulse than the idealized calculation. Of further interest is the uniformity of the pulse heights from both amplifiers when the depletion depth exceeds the particle range.

4. Similar Detectors and Specialized Configurations.

Besides the silicon surface barrier diode there are many other types of semiconductor nuclear particle detectors. Most of them are made from silicon and almost all use a rectifying barrier or junction.

(a) P-N Junction Detectors [Brown, 1961A].

Diffused junction diodes are usually made from high-resistivity p-type silicon by diffusing a donor impurity (such as phosphorus) in from the surface at elevated temperatures. A thin layer of n-type silicon is formed, and beneath it there is a rectifying p-n junction. This junction performs the same function as a surface barrier and, operationally, the two types of detectors perform in exactly the same manner. Thus the discussion of the space charge region, charge collection, and detector characteristics can be carried over from one case to the other with changes only to give the correct type of material and polarity. As the rectifying barrier is not at the surface, but is inside the bulk of the material for a diffused diode, one would expect a space charge region to be formed on both sides of the barrier. This is

indeed the case, but the resistivity of the diffused layer is so low that the depletion depth in the direction of the n-type material is truly negligible. Because the diffusion region exhibits zero collection efficiency, it constitutes a dead layer, or "window", on the face of the detector [Williams and Webb, 1962]. Very thin diffusions are used, though, and in practice the dead layer is observable only when counting heavy ions.

- (b) Lithium-Drift Detectors
 [Pell, 1961; Ziembra, Pelt, Ryan,
 Wang, and Alexander, 1962].

Lithium ion-drift techniques have been developed to meet the demand for deeper depletion depths. The key to this approach is equation (9), whereby the depth is proportional to the square root of the resistivity. If one can make the resistivity of a detector higher, one can also increase the depth. The ultimate would be the intrinsic resistivity of the material, which is 260,000 ohm-cm at room temperature in p-type silicon [Kittel, Introduction to Solid State Physics, 1956]. As the purest ingots obtainable are no more than 10,000 ohm-cm, there is clearly room for improvement.

The principle behind the lithium ion-drift techniques is the cancellation, or compensation, of the impurities existing in the

material. The useful properties of the lithium ion are, first, that it is a donor impurity in silicon, and, second, that it is an interstitial impurity, able to diffuse rather freely and to position itself without altering the existing crystal structure. Injected into p-type material, the lithium donors cancel the acceptors that are already present. Coulomb forces between ions regulate the distribution so that the compensation is even throughout the crystal. The balance between donors and acceptors places the Fermi level at the center of the band gap, and the material becomes effectively intrinsic.

Fabrication procedures are still being improved. One of the first manufacturers to develop a successful technique was Solid State Radiations, Inc., of Los Angeles. Some of their earliest units were obtained by the State University of Iowa for the proton telescope described in section V of this paper. These units were fabricated with an aluminum alloy back contact and a lithium diffusion in the front. The lithium was first evaporated on the front surface of the wafer and diffused in to a depth of 100 microns. The wafers were then placed in an oven and a high reverse voltage was applied. Their mobility enhanced by the high temperature, lithium ions from the front drifted into the intermediate region,

compensating the material and making it intrinsic. The drift was not carried all the way to the back contact, so that a layer of low resistivity silicon remained in the rear. When a back voltage is applied to the diode, the space charge region extends from the front junction through the intrinsic region up to the rear layer.

The units fabricated by this technique have several disadvantages. First, there are dead layers of considerable thickness on the front and back. This thickness is not controllable, and varies from unit to unit even among detectors in the same batch. Furthermore, the space charge region is not controllable and also varies from unit to unit. The active volumes in these detectors were not particularly deep by current standards, averaging around 400 microns.

Those shortcomings are offset by the following advantages. Although not considered deep nowadays, the detectors were the thickest that could be obtained at the time. The dead surfaces protect the more sensitive junctions and space charge region, making a very rugged detector. And finally the depth of the active region has proved to be very stable in time, in contrast to other types of lithium-drift detectors.

As implied, other techniques for manufacturing lithium-drift diodes have been developed and much deeper detectors are now available. The manufacturer who supplied the diodes described above has recently made units two millimeters thick with no dead layer on the front and a very small dead layer on the back.

(c) Totally Depleted Detectors.

The difficulties of uncertain diffusion collection, and of unknown or unstable depletion depths and dead layers are all nicely eliminated by totally depleted detectors. These are conventional diffused junction or surface barrier detectors in which the silicon wafer is cut thin enough so that the electron depletion region can be extended to the back contact. These diodes are usually made in transmission mounts having no material in front or behind, and the rear surfaces are prepared specially to prevent breakdown when the depletion region reaches the back. When one applies sufficient voltage, one has a windowless detector whose active volume is fixed by the physical dimensions of the silicon crystal itself.

Totally depleted detectors are made as thin as 25 microns [Inskeep, Eidson, and LaSalle, 1962] and as thick as 500 microns [ORTEC]. They are often called dE/dx detectors when they are used

to detect fast particles for which the energy loss in the detector is much less than the total particle energy. In such cases a pulse is just proportional to dE/dx for the incident particle, i.e., from equation (15)

$$\begin{aligned}
 P &= \int_0^d (- dE/dx) dx \approx (- dE/dx) \int_0^d dx \\
 &= (- dE/dx) d .
 \end{aligned}
 \tag{18}$$

These detectors are a late development, but they offer advantages which are of especial value in satellite instrumentation.

- (d) Thin Detectors for Heavy Particle Selection [Amsel, Baruch, and Smulkowski, 1961].

Rewriting equation (12) reveals that for different particles with the same energy, the rate of energy loss is approximately proportional to the particle's mass. It follows immediately that, under the conditions stated on page 15 for dE/dx detection, the heaviest particles will produce the highest pulses. One can assure this preference for heavy particles by making the active volume sufficiently thin. "Sufficiently thin" means much thinner than the range of the particles one wishes to eliminate, but still thick

enough to stop the heavier particles one is looking for.

This aspect of detector design can be presented quantitatively with the aid of the following theorem:

If heavy charged particles of the same type and all energies strike a solid state detector head on, the largest pulse will be produced by a particle whose range is equal to the depletion depth of the detector, and the pulse height will be the total energy of the particle.

This statement follows from equation (15) and is almost self-evident upon inspection of Figure 6. The highest pulse on the characteristic is equal to the energy of the fastest particle which stops within the detector. This is the case named above.

Now if one is looking for heavy particles against a background of light particles, one must make the detector so that the maximum pulse a light particle can leave will not interfere with the pulses one is looking for. The theorem stated above indicates the depth needed. As an illustration, suppose alpha particles are present in a background of protons. A 5 mg/cm^2 depletion region will stop 3.9 MeV alphas but only 1.2 MeV protons.

Then one can work with the alpha spectrum from 1.2 to 3.9 MeV.

The detector described in part IV of this paper applies this design principle to protons in a background of electrons.

III. ELECTRONIC REQUIREMENTS AND DATA SYSTEMS

Part II has presented the mechanics by which energetic particles produce charge pulses in a solid state detector. The present section will deal with the conversion of these pulses into information.

1. The Charge-Sensitive Amplifier.

To start with, consider the magnitude of the initial pulses. A 3.5 MeV particle will release one million electrons in a detector, or 1.6×10^{-13} coulombs of charge. Given a typical detector capacitance of 10 pf, this charge will produce a voltage of 16 mV. Clearly amplification is needed before such pulses can be handled by a data system.

Before solid state detectors became popular, laboratory amplifiers were universally of a voltage-sensitive type; i.e., they produced an output voltage proportional to an input voltage. In 1956 a configuration was pointed out in which the output voltage is proportional to the input charge [Cottini, Gatti, Gianelli, and Rozzi, 1956]. The advantage of the charge-sensitive amplifier is that the output signal is independent of the input capacitance. Since the capacitance of a solid state detector

varies when the applied bias is changed, the voltage pulse varies also; but the charge does not. As it is the charge pulse that one wants to measure, the charge-sensitive amplifier is the more stable configuration. It is now common to use a charge-sensitive first stage with a solid state detector. At its output the signal is presented in volts, and conventional voltage-amplifying stages follow.

As an approach toward visualizing the operation of a charge-sensitive amplifier, consider a method for the impulsive injection of a known amount of charge onto a capacitor C_1 . A capacitor C_p , ($C_p \ll C_1$), is placed in series with C_1 and an instantaneous voltage step V_p applied to the series combination of $C_1 + C_p$ (see Figure 10a). The voltage generator sees a capacitive load of $C_1 C_p / C_1 + C_p$ and transfers a quantity of charge Q_p given by

$$Q_p = V_p \frac{C_1 C_p}{C_1 + C_p} = \frac{1}{1 + \frac{C_p}{C_1}} C_p V_p \approx C_p V_p . \quad (19)$$

Then as long as $C_p \ll C_1$ the injected charge equals $C_p V_p$ and does not depend on the value of C_1 .

It is evident that the charge pulse from a detector is electronically indistinguishable from the injected charge described

above. Now consider the amplifier pictured in Figure 10b. C_1 in this case is the dynamic input capacitance of the amplifier plus the capacitance of the detector. The feedback capacitor C_f , ($C_f \ll C_1$), is the element that converts this into a charge-sensitive configuration. Let a charged particle dump a charge Q_p onto the input, producing an instantaneous voltage step V_1 :

$$V_1 = \frac{Q_p}{C_1 + C_f} \quad (20)$$

The amplifier puts out a voltage step,

$$V_o = -A \frac{Q_p}{C_1 + C_f} \quad (21)$$

whose rise time is required to be very fast. This step injects charge Q_f back onto the input by the mechanism described above, so that

$$Q_f = V_o C_f = - \frac{A}{C_1 + C_f} Q_p C_f \quad (22)$$

This charge is opposite in sign to the original Q_p , and tends to cancel it out. In fact, it can be seen that if $|Q_f| < |Q_p|$, the output voltage must have greater magnitude, and if $|Q_f| > |Q_p|$, the output voltage must have smaller magnitude. Evidently, the input charge must be restored to zero, and

$$Q_f = - Q_p . \quad (23)$$

Using equation (22), it is immediately deduced that

$$V_o = - \frac{Q_p}{C_f} . \quad (24)$$

Thus the circuit behaves as if all the detector charge were deposited on C_f and an output voltage pulse generated to just cancel it through the feedback loop.

More rigorous analyses of the circuit, including discussions of the design criteria, have been given elsewhere [Enemark, 1962; Fairstein, 1961; Emmer, 1961; Chase, Higinbotham, and Miller, 1961]. The preamplifier used with the Iowa solid state detectors was designed by D. C. Enemark and is shown in Figure 11. Figure 12 [Enemark, 1962] compares this with a voltage amplifier for sensitivity to input capacitance. As most detectors have less than 30 pf capacitance, the charge-sensitive configuration is clearly effective.

2. Preamplifier Calibration.

The method described above for injecting a precise amount of charge onto a capacitor provides a very convenient means for calibrating and testing the charge-sensitive preamplifier. C_1 is

once again the total capacitance at the input of the amplifier, and C_p is a built-in precision capacitor that can be connected to an external voltage-step generator. The requirements on the step generator are a very fast fall (or rise) time, low output impedance, and a linear amplitude control. Mercury relay pulsers having a fall time of less than 10 nanoseconds and 1% to 0.1% linearity are commercially available and are excellent for the purpose.

The pulse is used to inject a precise, and linearly adjustable, amount of charge on the input. To calibrate, one sets the amplitude control so the injected charge is just equal to the charge freed in the detector by a particle of known energy (commonly from an alpha source). The comparison can be made at the amplifier output, to $< 3\%$ uncertainty by viewing the pulses with a scope, and to less than $.5\%$ uncertainty by using a multichannel pulse-height analyzer. Knowing the pulser amplitude which is equivalent to a particle of a given energy, and taking advantage of the linearity of the pulser, one can then set the pulser to duplicate particles of any energy. Alternatively, if the detector is measuring unknown particles, one has but to match them with the pulser in order to determine their energy. As the matching is

done at the input of the preamplifier, the only assumptions upon which the method relies are (1) the linearity of the pulser, and (2) the stability of the capacitor C_p . Linearity and drift in the amplifier and in the pulse-height analyzer are notably irrelevant.

3. Pulse-Shaping and Noise Performance.

Preamplifier noise performance is important because of its effect on resolution. Whereas the ultimate resolving power of a solid state detector is limited by the statistical deviation in the number of carriers created by monoenergetic particles, the practical limit is determined by random noise generated by the detector and the preamplifier. In the SUI EOGO packages the surface barrier detectors are rated by their manufacturer (ORTEC) to give 25 keV resolution for 5 MeV alpha particles, and better for protons. The preamplifiers, handling monoenergetic impulses from an electronic pulser, produce a spread of 30 keV. The two together, measuring 6.05 MeV alpha particles, have a width of 45 keV (see Figure 13). In proton measurements the width will be determined almost entirely by the preamplifier.

Preamplifier noise performance is, of course, dependent on the bandwidth of the circuit, and this, in turn, is determined

by the pulse shaping. Generally, the best signal-to-noise ratio is obtained with a slow clipping time [Elmore, Electronics, 1949] which produces slowly falling pulses. When the ultimate in low-noise performance is desired, vacuum tubes are used in the amplifier, as they generate less noise than transistors [Fairstein, 1961], and the detector is cooled to reduce thermal noise. These techniques have brought experimenters to within a factor of 5 of the intrinsic statistical limit to resolution for internal conversion electrons [Blankenship and Borkowski, 1962].

Satellite instruments must be designed for transistors, though, and other constraints on the SUI detectors required the use of a very fast pulse. The rise time is that of the preamplifier, less than 100 nanoseconds, and the clipping time is determined by a shorted 0.1 microsecond delay line. The resulting pulse is symmetrical, with a total width of about 0.25 microsecond. The resolution of consecutive, nearly simultaneous, particles is far better with this circuit than with slower RC-clipped amplifiers. The discussion of the low energy proton detector in part IV of this paper will reveal the importance of this feature.

Preamplifier performance can be rated in several ways. One is to measure the dispersion produced in monoenergetic impulses

using a pulser and a multichannel pulse-height analyzer. This result was quoted above and is illustrated in Figure 13. Another method is to measure the rms noise at the input of the circuit [Fairstein, 1961]. This can be done by measuring the noise level after several stages of amplification and dividing by the gain. Note that with a charge sensitive amplifier this gives a result in units of charge or, more conveniently, electrons. The preamplifiers on Relay have an input noise rating of 3600 electrons and those built for EOGO have a rating of 2600 electrons. The difference is attributed to a change in transistors and to improved packaging.

A third method of evaluation is useful when the amplifier is followed by a pulse-height discriminator. An external signal is injected with a pulser and the pulse height is stepped past the discriminator threshold. The ratio of output to input counting rate, plotted against input signal height, traces an integral profile of the system noise. The 12% and 88% intercepts determine the full width at half maximum (FWHM), and the 50% intercept determines the midpoint of the discrimination level. It is easy to fit this data to a Gaussian curve by plotting it on probability coordinate graph paper. By such a fit the FWHM and the 50%-probability level can be determined with only two data

points. Figure 14, from an EOGO unit, demonstrates the Gaussian distribution and exhibits an FWHM of 19.5 keV.

Intercomparison of the results obtained by different methods should be possible. Specifically, for a Gaussian distribution given by

$$N(x) dx = \frac{1}{\sigma \sqrt{2\pi}} \exp\left(-\frac{x^2}{2\sigma^2}\right) dx, \quad (25)$$

the $\text{FWHM} = 2.35 \sigma$. Method 2 measures σ directly ($q_{\text{rms}} = \sigma$), and so one can convert the results of method 2 into an expected FWHM.

$$\text{FWHM (eV)} = (3.5) (2.35) q_{\text{rms}} = 8.2 q_{\text{rms}}. \quad (26)$$

For the EOGO units the FWHM's measured by methods 1, 2, and 3, respectively, are 30, 21, and 19.5 keV. This is typical of the best performance to be obtained from transistor circuits. Although vacuum tube circuits can be quieter by about a factor of 5, the next section will show that the difference is quite unimportant for the detector systems to be described.

4. Particle Counting and Energy Analysis.

By conventional voltage amplification the signal from the pre-amplifier can be brought to any desired magnitude. The amplifier then

presents a usable pulse whose height is calibrated in terms of particle energy. In this way every particle that strikes the detector indicates its presence and reveals its energy.

Straightforward counting and analysis can be done by the system diagramed in Figure 15. A pulse-height analyzer follows the amplifiers, and its output channels register pulses whose heights fall within an assigned range. Gating or logic may be applied to these output lines to obtain some desired information, and then the counts are fed to a memory, which accumulates and stores them until a readout is desired.

The number of channels may range from one, for a simple trigger-level discriminator, to 512 or more, used in many nuclear laboratories. It is easy to see that a single detector, with high resolution and a wide dynamic range, can make use of many channels. As a modest example, the EOGO system, whose resolution has already been quoted, is linear for protons up to 1.5 MeV. This range could be broken up into 50 to 100 channels with no overlap of information. In the satellite field this many channels is not worthwhile at the present time. In the first place it would require an unreasonable amount of telemetry to transmit this much information to the ground; and in the second place the data

would serve no purpose. The EOGO system referred to utilizes only two channels, which are sampled alternately to conserve telemetry space.

The Relay and EOGO detectors employ pulse-height analyzers of both integral and differential types. Integral pulse height analyzers count all pulses which are above a given level: $P > L$. Differential, or "window" analyzers count all pulses between two levels, that is, above one and below the other: $L_2 < P < L_3$. Examples of these types are commercial multi-channel analyzers, which are of the differential type, and single level discriminators such as the Schmidt trigger circuit, which are of the integral type. A series of integral discrimination channels can be converted into differential channels by performing anti-coincidence logic between consecutive levels: $P > L_2$ and $P < L_3$ means $L_2 < P < L_3$. It is evident that, as the number of levels increases, the number of circuits required by this method will become very large. For this reason commercial multi-channel systems use a different approach, performing analog to digital conversion of the pulse height and digital routing to the proper channel. The differential analyzers for Relay have only a few levels, though, and they use integral discriminators followed by anticoincidence circuits.

Figures 16 and 17 demonstrate the differential and integral pulse height schemes used by the Relay and EOGO low energy proton detectors. The Relay scheme, Figure 16, has three differential pulse-height channels defined by four integral discriminators and three anticoincidence circuits. The energy bands determined by these channels are listed in Table I (a).^{*} The EOGO scheme, Figure 17, has two integral pulse-height channels alone, defining the two partly redundant energy bands listed in Table I (b).

Comparison of the schemes shows that, even with the different number of channels taken into account, the integral plan of EOGO is simpler. Furthermore, for the determination of energy spectra, integral channels contain as much information as the same number of differential channels. This statement is based on the assumption that the data will be fitted to an energy spectrum which has adjustable parameters. Each data channel enables one to write an equation in terms of the spectral parameters, and the solution of the equations provides the spectrum. This procedure is valid for both integral and differential channels, provided only that

* The dE/dx energy levels given in Table I are calculated, and do not take diffusion collection into account. The corrected levels must be determined experimentally and are in Table II.

Table I (a)

Relay Detector B
Design-Center Pulse-Height Channels and Energy Ranges

	Pulse-Height Range	Energy Range
Channel 1	0.78 < P < 1.4 MeV	1.0 < E < 1.5 MeV and 6* < E < 11.5* MeV
Channel 2	1.4 < P < 2.2 MeV	1.5 < E < 2.25 MeV and 4* < E < 6* MeV
Channel 3	2.2 < P < 3.7 MeV	2.25 < E < 4* MeV
Channel 3'	3.7 < P	Background

Table I (b)

EOGO Detector H
Design-Center Pulse-Height Channels and Energy Ranges

	Pulse Height Range	Energy Range
Channel α	0.42 < P	0.5 < E < 5* MeV
Channel β	0.83 < P	0.9 < E < 2* MeV

*The dE/dx levels given in Tables I (a) and I (b) are calculated, and do not take diffusion collection into account. The actual levels must be determined experimentally and can be found in Table II.

the data are independent. Thus the use of differential channels on Relay does not provide a better energy spectrum, but it does provide advantages which will be mentioned in the next section.

IV. A SINGLE-ELEMENT PROTON DETECTOR

The low-energy proton counters in both the EOGO and Relay package are based on the same, or similar, principles. The detector is a single diode, with several pulse-height discrimination levels to determine energy channels. A shield restricts the solid angle and provides the directionality needed for calibration. The detector is able to distinguish protons in a high flux of electrons by an application of the principle explained in section II.4(c). These design features are described more fully below.

These detectors are pictured in Figures 18, 19, and 20. The Relay low energy proton counter, labeled detector B, is in the top half of the box shown. The upper brass cylinder is the shield, and the electronics deck contains the preamplifier and one postamplifier. Improved packaging techniques, and the greater simplicity of the circuitry, allowed the entire EOGO detector to be fitted inside one box, as shown in Figures 19 and 20.

There are some features of these packages that are worthy of mention. The layout on EOGO was designed to minimize the pickup of stray rf noise, and this effort is headed by an individually shielded preamplifier. The entire EOGO detector is

outstanding for its light weight--only 190 grams--and its compact dimensions. It will count low energy protons in the outer zone and can operate without heavy shielding. By contrast, on Relay the aperture alone weighs 170 grams, but it will operate in the inner zone where heavy shielding is necessary to block the penetrating radiation.

1. Design Features.

- (a) Shielding.

The designer is faced with the fact that in space, unlike a nuclear laboratory, the radiation comes from all directions. Because the detector is calibrated for one direction only, he must assure himself that the particles being analyzed are coming from the right direction. The most straightforward way to do this is to shield the detector in the other directions and let the analyzable particles come unobstructed through an aperture. No finite shield will be absolutely effective, though, for high energy particles will penetrate it and cause an omnidirectional background counting rate. The shield is adequate if the background is much lower than the foreground, or desired, counting rate.

To meet this criterion, one can enlarge the aperture and increase the acceptance angle. However, this compromises

directionality, and thus sacrifices sharp definition of the upper cutoff energy. If one decides to limit the variation in projected detector depth to 15%, the incidence angle must be restricted to 30° . A conical aperture of this half-angle presents an acceptance solid angle of .84 steradian, compared to 11.7 steradians over the background. The ratio of background to foreground geometric factors is then 7:1. (A factor of 1/2 enters because the detector presents a smaller area to particles coming from the side.) It is evident that the back directions must be well shielded to reduce the background flux safely below the foreground. Now the particles which penetrate a shield are those whose range is greater than the shield thickness. Then one can set the shield thickness by demanding that the flux of particles of this energy be sufficiently less than the flux of the particles intended to be counted.

As an example of such a calculation, let us review the problem of shielding the Relay low-energy proton detector. With the aperture fixed at 15° conical half-angle, the ratio of foreground to background geometric factors is 1:28. The ratio of fluxes is more favorable, though, because the detector is sampled only when it is looking in the most intense direction, which is perpendicular to the magnetic field line. The gain by this procedure is typically a factor of 3. To make the background

flux 10% of the foreground flux, then, one needs a factor of 90 from the shield. On the basis of earlier measurements in the inner zone, a guess was made that the total flux of protons of energy greater than E was proportional to $1/E$. As the detector counts protons of energy down to 1 MeV, it is required that the shield stop particles of 90 MeV. A factor that has been left out of this accounting is the effect of pulse-height selection channels and their efficiencies for particles of various energies at different angles. The differential channels used on Relay are unfavorable to particles coming through a shield at high incidence angles, and so an additional advantage is gained of perhaps a factor of 10. The aperture designed for Relay has a wall thickness of 1 cm of brass, which will stop protons up to 85 MeV. It was estimated that the background counting rate due to particles coming through this shield would not be more than 1% of the foreground rate.

The shield for the Relay low energy proton detector is seen in Figure 21. The configuration was chosen with two ends in mind: (1) to get the maximum shielding for the least weight; and (2) to provide a clean, well-defined and calculable geometry. The first end is served by using a heavy material and getting it

in close to the detector. The tiny size of the detector is extremely advantageous in this respect. Clean geometry is obtained by creating a sharply defined acceptance angle and providing a uniform shield thickness over the sides and rear. The acceptance cone would be absolutely sharp if the ratio of aperture to detector dimensions were infinite: for example, if the detector were a point, or if the rim of the shield were infinitely far away. Realistically, the sharpness is not badly compromised with the aperture rim about ten detector diameters from the focus of the cone. The penumbral angles of partial acceptance are minimal, and the geometric factor can be calculated from a simple integration of the projected detector area over the solid angle of the cone.

To make the best distribution of the shielding, one can choose between two criteria: (1) criticality, or (2) calculability. The background counting rate will be lowest if one finds which angles are critical, and bolsters the shielding in these directions. Interpretation of the data and background calculations will be easier, though, if one can find a sufficient shield thickness and use this thickness in all directions. The shield in Figure 21 follows this principle by providing a uniform one cm of brass shielding measured radially outward from the detector.

(b) Geometric Factor.

The geometric factor is the proportionality constant between the particle flux and detector counting rate, so that

$$\phi \text{ (particles/cm}^2\text{-sec-ster)} G \text{ (cm}^2\text{-ster)} = CR \text{ (particles/sec)}.$$

This figure is chosen to obtain as wide a dynamic range as possible.

Thus a large geometric factor is desirable for detecting low particle fluxes, but it must not be so large that the detector saturates, or the accumulators overflow, in the highest fluxes.

The problem of accumulator overflow can be handled by adding prescalers, scaling stages that divide the counting rate down before it is fed to the accumulators; but this solution impairs the sensitivity and resolution for low rates.

The preceding section has covered several constraints which the aperture imposes on the geometric factor. Namely, these are the change of effective detector depth as the angle of incidence increases, and the problem of getting a satisfactory foreground to background ratio. Within these constraints the aperture can be opened up or closed down to set the solid angle as desired. Detector area is a second design variable which can be used to determine the geometric factor. Detectors can be made with

a wide range of areas, from less than one square millimeter to several square centimeters. This flexibility permits solid state detector design to be optimized for a large variety of uses.

(c) Elimination of Electrons.

The most important feature of the Relay and EOGO low energy proton detectors is that they are able to count and analyze protons in the presence of a high flux of electrons. This capability does not depend upon a broom magnet, an advantage which is welcome on spacecraft which are also carrying out magnetic field measurements. Immunity to electrons is achieved by a combination of three measures:

1. The use of a thin detector to minimize energy loss by penetrating electrons.
2. Placing the discrimination levels far above the probable energy loss for individual electrons.
3. The use of an amplifier with a fast pulse resolving time to avoid coincidence of many low pulses which might pile up to the discrimination level.

Points one and two are a simple application of the principle presented in section II.4(d) for analyzing heavy particles with a thin detector. Point three recognizes the additional possibility that many low energy particles, arriving at almost the same time and

not resolved by the amplifiers, could form a single pulse high enough to trigger the discrimination level.

Electrons do not behave in solid state detectors exactly the same as heavy ions. Because of their smaller mass, they can lose more energy in a single collision, and they can be deflected to larger scattering angles in their encounters with the electrons of the stopping material. As a result their energy loss is not so uniform, and their paths in the detector are rather irregular. A pulse-height spectrum taken with monoenergetic electrons of range greater than the detector depth exhibits two principal features. First there is a large dE/dx peak, analogous to that which would be observed with penetrating heavy ions, but much broader because of the nonuniformity of the electrons' energy loss. The other feature is a total energy peak, having no parallel with heavy ions, which represents electrons stopping wholly within the space charge region. This peak consists of "dishonest" electrons which either lose all of their energy in a few catastrophic collisions or else scatter sideways and move through the space charge region parallel to the surface. The published spectra [McKenzie and Ewan, 1961] showing these features were recorded with detectors made exceptionally thick to increase the probability of capturing an electron's total

energy. The thinness of the EOGO and Relay detectors by contrast makes them very inefficient for this process.

(d) Discrimination Levels.

The discrimination levels for the Relay and EOGO low energy proton counters have already been seen in Figures 16 and 17, along with their respective detector characteristics. Some of the general considerations for pulse-height analysis were mentioned in section III.4, but a further discussion of the specific constraints on these detectors is now appropriate.

Determination of the lowest discrimination level was made with regard to the electron pileup problem. In both designs the lowest level was set at about five times the energy loss of an "honest" electron, in order to make the electron efficiency sufficiently low. If the lowest level is dictated by the necessity of counting a given energy proton, it is evident that this consideration determines the depth of the detector.

It is of interest to ask what is the limit on the lower discrimination level if there are no electrons present: for instance, if a broom magnet is used. The determining factor in this case will be detector or amplifier noise. The random motion of electrons in the detector and in the preamplifier input stage

causes a non-vanishing level of noise below which pulses cannot be distinguished. In a test made with an EOGO package electronic pulses were viewed on a multichannel analyzer and compared with the input noise level. It was found that pulses below 100 keV became increasingly engulfed in the noise, so that, with this detector and circuitry, the limit would be around 100 keV.

It is worthwhile to note the highest level, labeled δ , on the Relay scheme (see Figure 16). As this level (3.7 MeV) is comfortably over the maximum pulse on the characteristic curve (3.3 MeV), it is evident that it will not count protons whose path-length in the detector is limited to the depletion depth. To trigger this level, a proton must traverse the detector sideways; i.e., it must be a background particle coming through the shield. Thus the number of counts above this level is a crude measure of the omnidirectional background flux which penetrates the shield. Channel B3', which alternates with channel B3, reads out this counting rate as a check on detector performance.

If the above conclusion is inverted, it is seen that pulses above 3.7 MeV should not be counted with the particles collimated by the aperture. Here is a reason for using a differential pulse-height analysis scheme, so that any channel has an upper, as well

as a lower limit. This reason is enhanced by the effect of a shield, which narrows a differential energy band. Thus the sensitive band from 0.7 to 3.7 MeV on the inside of the Relay shield corresponds to protons from 85.0 to 85.15 MeV on the outside of the shield. The anticoincidence circuits used on Relay take advantage of this gain.

(e) On-Board Source.

The Relay background channel, B3', although insensitive to protons coming through the aperture, is able to count alpha particles of the appropriate energy. This fact enables it to monitor an on-board alpha source of low activity with a minimum of interference from the trapped radiation. Monitoring the on-board source gives a performance check on the detector and much of its circuitry when it is in orbit. Just as the trapped protons produce a minimum of interference with the on-board source channel, the alpha particles, by virtue of the anticoincidence circuits, do not contaminate the proton channels. Figure 22 shows a spectrum of the on-board source for one of the Relay units. To provide a reference grid, the α , β , γ , and δ discrimination levels are marked by monoenergetic pulses from an electronic pulser. The pulse-height spectrum from a Tl 204 beta source is

also shown, to demonstrate the detector's discrimination against electrons.

It is evident that this channel will also count trapped alpha particles if any are present. The energy window for trapped alpha particles is from about 4.3 to 35 MeV.

(f) Light-Tight Foils.

In a satellite of varying orientation, it is inevitable that a detector should sometimes look at the sun. Being very light sensitive, solid state detectors must be shielded to keep the sun from contaminating the particle counting rates. It is increasingly difficult to protect detectors as the particle energy threshold is lowered, because too thick a shield may stop the very particles one wants to detect.

The easiest shield material to use is tough, resilient aluminized mylar, available in thicknesses down to .00025 inches. However, as this is greater than the range of a 900 keV proton, it is too thick for the detectors described here. Nickel foils are available [Chromium Corporation of America] in thicknesses down to a few microinches. For the Relay detector, it was possible to use a rather strong 75 microinch foil, equivalent in particle stopping power to 1.2 mg/cm^2 of air, which subtracts about 280 keV

from the energy of a 1 MeV proton. Even this foil, though, was too thick to use for EOGO, which has to count 500 keV protons. For this detector two 12.5 microinch foils were mounted back to back, so that microscopic defects in one foil would be covered up by the other. As this thickness of nickel is too delicate to be handled, the foil comes with a copper backing. The foils are placed in their mount and then the copper is etched off with chromic acid. These foils are difficult to make, and give a low yield of satisfactory units, but the good ones have a higher light attenuation than those used on Relay, and a thickness equivalent to only 0.2 mg/cm^2 of air.

The foil, the amplifier noise level, and the necessity of discriminating against electrons are the three obstacles to lowering the detection threshold for protons. If electrons below 500 keV were eliminated by a broom magnet, the higher energy electrons would not leave enough energy to be harmful. Then the discrimination level might be lowered to the limit of the noise. It seems reasonable that with a broom magnet and a foil identical to those made for EOGO, the proton threshold could be pushed down as low as 200 keV.

2. Proton Calibrations.

Calibrations were done on the Relay detector using protons generated by the $d(He^3, p)He^4$ reaction. The He^3 was accelerated by the Cockcroft-Walton accelerator at Iowa. The reaction has a Q of 18.3 MeV and produces 14.7 MeV protons at an angle of 90° (lab coordinates).

(a) Determination of Depletion Depth.

With a design that specified a depletion depth of 100 microns, it was first necessary to find what voltage should be applied to the detector. This was done by an application of the theorem stated on page 24. Absorbers were used to reduce the energy of the proton beam and center it close to 3.3 MeV. Landau spread made the distribution broad enough so that it extended from 2 to 4.5 MeV. The spread is illustrated in Figure 23 (a), where it is viewed with a detector thick enough to stop all the protons. The sharp peak, superimposed on the proton distribution by an electronic pulser, marks 3.4 MeV. The applied voltage on the detector was now lowered until the depletion depth corresponded to the range of a 3.3 MeV proton. This point was recognized, according to the theorem referred to above, when the pulse height distribution was

cut off at 3.3 MeV. Figure 23 (b) illustrates a typical cut-off distribution. Because of the finite (but small) width of the cut-off, it was decided to pick the channel where the distribution fell to $1/2$ of its maximum. In the illustration, this channel corresponds to an energy of 3.2 MeV. A slight correction was made to the applied voltage to bring this up to 3.3 MeV.

(b) Energy Ranges.

The calculated energy ranges for each of the Relay channels are depicted in Figure 16 and listed in Table I. It is noted, however, that the energies of the penetrating protons are calculated for the idealized case of no diffusion collection, and they must be corrected empirically, as explained in section II.3.

To determine what these energy cutoffs really are, an experiment was performed using, once again, the 14.7 MeV protons from the $d(\text{He}^3, p)\text{He}^4$ reaction. Absorbers were placed in the beam to adjust the energy of the incident protons, and the counting rates from each channel of a Relay detector were recorded. The energy spectrum of the degraded beam was observed by a spectrum monitor detector thick enough to do total energy pulse-height analysis up to 7 MeV. A third detector monitored the proton

production rate and was used to normalize all runs with the Relay detector and the spectrum monitor detector. The results of the experiment are exhibited in Figure 24. The runs are marked in on the energy scale according to the proton energy as shown on the spectrum monitor detector or as calculated from the absorbers placed in the beam. The first row shows the output of the spectrum monitor detector, recorded by a multichannel analyzer, for the runs below 7 MeV. Row three shows the output of the Relay detector, in counts per channel. These data were used to find the cutoff energies for penetrating protons in each channel of the Relay detector, and these cutoff energies are depicted in row four, which gives the experimental efficiencies for each Relay channel. The accuracy of this result can be checked by multiplying the incident proton spectrum, from row one, by the derived efficiency of each Relay channel, to find the number of incident protons in each energy range. The result of this calculation, given in row two, should agree with the detector B data in row three. The closeness of the agreement is the experimental proof of the efficiencies presented in row four.

The cutoff energies shown for non-penetrating protons are based on electronic calibration of the discrimination levels

according to the method of section III.2, allowing for energy loss in the thin foil covering the detector. The accuracy of this calibration is also confirmed by the two lowest energy runs of the experiment described above.

The calibrated discrimination levels and energy ranges for this Relay unit are tabulated in Table II. This can be compared with Table I (a) to see the effect of diffusion collection in extending the upper limit of the energy ranges. There are also small discrepancies between the intended and actual discrimination levels. Those are due to small differences which occur from unit to unit.

3. Response to Electrons.

An EOGO detector was tested in the beam of the Iowa 150 keV electron accelerator to determine its response to very high fluxes of electrons. The accelerator provided a beam of monoenergetic electrons at energies from 60 to 140 keV and at currents which were varied to give from 10^4 to 10^7 particles per second on the detector. Two important conclusions can be made on the basis of this experiment:

1. For fluxes below the onset of counting by the detector, neither the resolution nor the discrimination thresholds are significantly impaired by the electron background.

Table II

Relay Detector B, Unit 2

Calibrated Pulse-Height Channels and Energy Ranges

	Pulse-Height Range	Energy Range
Channel 1	$0.72 < P < 1.35$ MeV	$1.0 < E < 1.6$ MeV and $7.1 < E < 14$ MeV
Channel 2	$1.35 < P < 2.11$ MeV	$1.6 < E < 2.25$ MeV and $4.75 < E < 7.1$ MeV
Channel 3	$2.11 < P < 3.63$ MeV	$2.25 < E < 4.75$ MeV
Channel 3'	$3.63 < P$	Background

Light-tight foil thickness = 1.22 mg/cm^2 of air (equivalent).

2. For fluxes which produce counts in the detector, the counting rate is due to pileup and obeys a simple model of multiple coincidence probabilities.

Conclusion 1 is established by the data shown in Figure 25.

This graph shows the lower discrimination level, both without electrons, and in a flux that produced a counting rate of two per second. The discrimination level is defined by a counting rate vs pulse height curve obtained with an electronic pulser by stepping the calibrated pulse height past the discrimination level. The FWHM indicated by this curve (see section III.3 on noise performance) increased from 19.5 to 27.5 keV in the electron beam, an unimportant increase, and the discrimination level changed by only 1.2%.

(a) A Model for Multiple Coincidence
Pileup.

To establish conclusion 2 we must first present a model with which we can calculate multiple coincidence counting rates. To make the model workable, idealize the delay-line-clipped amplifier pulse to a square wave of width τ . If a number, n , of particles with energy h arrive within a time interval τ , the pulses will be considered to pile up to a total height of nh . This will be called an n -fold coincidence. If a particle strikes the detector at

time $t = t_1$, the probability, P_n , can be computed that $n-1$ particles will arrive before $t = t_1 + \tau$, forming an n -fold coincidence. This probability times the average flux, ν , gives the rate of occurrence of pulses of height nh .

Since the incidence of particles is a random process, the probability that the interval between two successive events lies between t and $t + dt$ is

$$p(t) dt = \nu e^{-\nu t} dt. \quad (27)$$

Thus the probability of a second event's occurring within a time τ of a previous one is

$$P_2 = \int_0^{\tau} \nu e^{-\nu t} dt = (1 - e^{-\nu \tau}). \quad (28)$$

This gives boundary conditions on P_2 of 0 and 1 for $\tau = 0$ and $\tau = \infty$, which is correct.

An expression can now be developed for the probability of a multiple (say, fivefold) coincidence. The first particle arrives at time $t_1 = 0$. The probability that the second particle arrives at time t_2 is

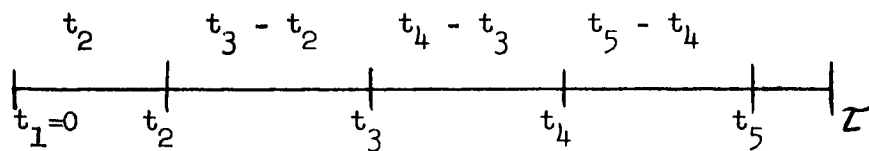
$$\nu e^{-\nu t_2} dt_2.$$

The probability that the third particle arrives after an interval $t_3 - t_2$ is

$$\nu e^{-\nu(t_3 - t_2)} dt_3 .$$

The probabilities for the fourth and fifth events to occur at times t_4 and t_5 are

$$e^{-\nu(t_4 - t_3)} dt_4 \text{ and } e^{-\nu(t_5 - t_4)} dt_5 .$$



The time scale is represented above. The probability for all the events to occur at the given times is the product of the probabilities:

$$\nu^4 e^{-\nu t_5} dt_2 dt_3 dt_4 dt_5 .$$

As times $t_{2...5}$ do not have to be fixed, integrate over all possibilities to get

$$P_5 = \nu^4 \int_0^{t_3} dt_2 \int_0^{t_4} dt_3 \int_0^{t_5} dt_4 \int_0^{\tau} dt_5 e^{-\nu t_5} . \quad (29)$$

Evaluating this integral gives a series which can easily be extended to other multiplicities:

$$P_5 = 1 - e^{-\nu \tau} \left[1 + \nu \tau + \frac{\nu^2 \tau^2}{2} + \frac{\nu^3 \tau^3}{6} \right] . \quad (30)$$

It is convenient to introduce the variable $x = \nu \tau$ in writing these series. Then

$$P_n(x) = 1 - e^{-x} \left[1 + x + \frac{x^2}{2!} + \dots + \frac{x^{n-2}}{(n-2)!} \right] . \quad (31)$$

The rate of occurrence of n-fold coincidences is now given by

$$R_n = \frac{1}{\tau} x P_n(x) . \quad (32)$$

$x P_n(x)$ has been computed for several n's over the interval $.05 \leq x \leq 1$ and is shown in Figure 26. Also noted is the slope of the curve at the intercept where $x P_n(x) = 2 \times 10^{-4}$. This intercept corresponds to 1000 cps if $\tau = 2 \times 10^{-7}$ sec.

The remarkable feature of the slope is that it is only slightly less than the integer identifying the multiplicity and distinctly represents that multiplicity.

(b) Verification of the Model.

The experimental data against which this model is to be checked consists of counting rate vs beam current curves for different settings of electron energy. With the detector biased deep enough to collect the total energy of the electrons, the multiplicity of the pileup needed to trigger the discrimination level of 416 keV is equal to the discrimination energy divided by the beam energy. This is in general a non-integer number, but the theoretical connection between the slope of the counting rate curve and the multiplicity of the pileup can plausibly be extended to non-integers so as to accommodate reality.

The counting rate data are shown in Figure 27 with each slope calculated by an rms best fit. The similarity to the theoretical counting rate curves of Figure 26 is clear, but the best test lies in comparing the slopes. Figure 28 is a plot of slope vs multiplicity, both as theoretically calculated, and as observed. Although the comparison is short of perfect, it is convincing evidence that the slope of the counting rate curve

represents the multiplicity, and that the model of multiple coincidence pileup describes the mechanism by which the electrons cause counts in the detector.

According to section IV.1(c) this detector combats pileup by using a thin depletion depth to cut down the energy loss by electrons, and by setting the discrimination level up to require a highly multiple pileup. As seen by the preceding discussion, we should be able to observe the multiplicity of this pileup by measuring the slope of the counting rate curve taken with a thin detector. Figure 28 includes four points taken for penetrating electrons in the thin detector. The scatter is bad, indicating poor data, but the high slopes confirm the effectiveness of the design.

In discussing this experiment we must mention the critical flux at which appreciable counting starts. Unfortunately, instability of the beam focus caused counting rates to drift and made it impossible to calibrate the beam current in terms of particle flux. However, it appears safe to say that the detector is insensitive to fluxes of over 10^6 electrons per second in the worst energy range from 70 to 130 keV, and that it is even more insensitive to other energies. This should be sufficient to provide clean data anywhere in the radiation belts.

V. A TWO-ELEMENT PROTON TELESCOPE

A second solid state detector package was built for the Relay payload to count and analyze higher energy protons. This counter is a two-element telescope, using the Li-drift detectors described in section II.4(b), and classifies protons from 18 to 60 MeV in three energy bands.

1. Directionality.

It was observed in section II.3 that directionality is required to do pulse height analysis on penetrating particles. The low energy proton detectors are made directional by means of collimation, overcoming the problem of omnidirectional background by shielding. This solution is not so practical for higher energy protons, for the amount of shielding required to stop the particles becomes prohibitive. A new approach is to let all the high-energy particles strike the detector, but to identify those coming in the right direction and count these only. The identification is done by a sentry detector, placed in line with the analyzing detector. A high energy proton coming in the right direction penetrates both detectors, leaving simultaneous pulses. Counts which are coincidental in the two detectors are the only ones recorded.

Such an arrangement of detectors, requiring coincidence for directionality, is called a telescope.

It is easy to see that the size and the separation between the two detectors determines the solid angle of acceptance. The same considerations of foreground-to-background ratio and sharp definition of the energy levels apply here as before, background in this case being the rate of random coincidences. The geometric factor was desired as large as possible, because the fluxes of trapped high energy protons are not high.

The configuration of the telescope, named Relay detector C, is shown in Figure 29. The two 1 cm^2 detectors are placed 2 cm apart, with their faces parallel and their sides rotated at 45° with respect to each other. The brass cylinder holding the detector is mounted next to detector B on the box seen in Figure 18.

2. Proton Energy Analysis.

The rear detector, named C2, performs the most important pulse height analysis, with detector C1 being called upon to resolve the ambiguity between the total energy and the dE/dx parts of the characteristic. The proton analysis scheme is seen in Figure 30.

Two detector characteristics are given for detectors C1 and C2, with the discrimination levels drawn in. The block diagram shows how the pulses are sorted and demonstrates the requirement of coincidence.

As an illustration, consider a 50 MeV proton passing through the telescope from front to back. It leaves a pulse in C1 between the levels $C1_{\alpha}$ and $C1_{\gamma}$, and a pulse in C2 between $C2_{\alpha}$ and $C2_{\beta}$. According to the block diagram, the pulse greater than $C1_{\alpha}$ but not greater than $C1_{\gamma}$ triggers an anticoincidence circuit, and simultaneously the pulse greater than $C2_{\alpha}$ but not greater than $C2_{\beta}$ triggers another anticoincidence circuit. The simultaneous outputs of these anticoincidence circuits trigger a coincidence circuit, and this circuit registers a pulse in channel C3. Notice that the analysis done by detector C1 resolves the ambiguity of the pulse in C2, which might have been left by a 50 MeV proton or an 18 MeV proton. 50 MeV and 18 MeV protons leave the same pulse in C2, but different pulses in C1, and so the proper identity of the proton is established by referring to C1.

The information in Figure 30 is expressed with more elegance by Figure 31. Pulse height in detector C1 is the ordinate and that in detector C2 is the abscissa. Any point in the plane

represents a coincidence between a pulse in C1, whose height is the ordinate of the point, and a pulse in C2, given by the abscissa. The coincidence-anti-coincidence scheme divides this plane up into several blocks, whose areas are bounded by the discrimination levels. The three coincidence channels C1, C2, and C3 are seen as areas, and an alternate channel, C3', which does not require a pulse in detector C1, is an area unbounded in one dimension. The lines labeled "foreground locus" and "background locus" identify the loci of points in the plane that represent pulse pairs created by protons. The foreground locus represents protons incident on the front and traversing front to back, and the background locus represents protons incident from the rear. Several of the points are marked by the appropriate proton energies.

Several characteristics of the telescope are made quite transparent by this chart. For instance, it is reaffirmed that the C2 discrimination levels define the energy ranges, with detector C1 to eliminate the undesired segment of the locus. Also it is seen that protons coming from the back direction can also be counted, although a rear absorber plug (visible in Figure 29) foreshortens the sensitive energy ranges considerably. The extra channel, C3', is read out alternately with channel C3. It is used

as a background monitor, giving a single detector counting rate so that the rate of random coincidences can be estimated.

3. Determination of Detector Parameters.

The telescope described above was designed for totally depleted detectors, which were to be round and $\frac{1}{2}$ mm thick. Execution of the design with these detectors would have been exceedingly straightforward, as there was only one detector parameter to be considered, the depth, and this would have been easy to measure and unquestionably stable. In the fall of 1961, however, when detectors were purchased for Relay, the manufacturers' fabrication procedures for totally depleted detectors were not yet perfected. It was necessary to shop for a substitute, and the design was accommodated to the available Li-drift detectors described in section II.4(b).

The superior features of these detectors are their ruggedness and their depth, needed to obtain substantial pulses from very fast-moving protons. The shortcomings were the necessity of measuring the depth, the front, and the back windows, and of establishing that these would not change. The methods of measuring these parameters are presented in this section.

The tool that was used to probe the live and dead layers of the detector was the 14.7 MeV proton beam from the $d(He^3, p)He^4$

reaction generated on the Iowa Cockcroft-Walton accelerator. The sensitive depth was determined in a manner similar to that used for detector B, again applying the theorem on page 24. In this case absorbers were used to vary the beam energy until, by trial and error, the highest pulse distribution was found. The height of these pulses themselves identified the particles whose range equaled the depletion depth, and the depletion depth was then read from a range-energy chart such as Figure 5. As an example, a maximized pulse height distribution is shown in Figure 32. The sharp peak at 7.25 MeV indicates a depletion depth equivalent to 96 mg/cm^2 of aluminum, as read from the curve.

The window thicknesses were measured by a modified range technique. The most straightforward, but rather uncertain, way of doing this is to place measured absorbers between the proton source and the detector until the protons just stop producing pulses in the active layer. From the initial energy of the protons, one knows the total amount of absorber material between the source and the front of the active layer. By adding up the measured absorbers, one also knows the amount of material between the source and the front of the detector. The difference is the thickness of the dead layer.

The difficulty with this method is the scatter in the proton ranges after they have been reduced from 14 MeV to nearly zero energy. The range listed for a 14 MeV proton is the mean range; half of the protons straggle farther than this and half, not so far. Consequently the range cutoff is not sharp and cannot be identified precisely by monitoring the counting rate.

The very simple solution to this problem is to make the protons stop in the active layer. The energy distribution determined by the pulse heights is synonymous with a range distribution, the mean being at the peak. The mean range of the particles is then known as they enter the active layer, and the same type of addition as before pins down the unknown thickness of the dead layer. Figure 32 illustrates the mean ranges measured by this method for particles entering the detector through the front and rear windows. The accounting of absorber thickness is worked out below:

Front Window	
known absorbers	221.5 mg/cm ² (Al)
mean range	60
<u>front dead layer</u>	<u>x</u>
initial proton range	327
 x = 45.5 mg/cm ² (Al)	

Rear Window	
known absorbers	12 mg/cm ² (Al)
mean range	46
<u>rear dead layer</u>	<u>x</u>
initial proton range	327
 x = 269 mg/cm ² (Al)	

A consistency check is obtained by adding up the front window, active layer, and rear window to find the total detector thickness, which should be the same for all detectors. The example illustrated above adds up to 410.5 mg/cm^2 , as against an average taken over 17 determinations on different detectors of 416 mg/cm^2 with an rms deviation of 12 mg/cm^2 .

A more direct check on each detector is made by measuring the dE/dx pulse height left by the protons, with no absorbers, penetrating the active depth from the front. This pulse height distribution is also in Figure 32, and the result of 3.0 MeV is to be compared with a value of 2.9 MeV predicted on the basis of the previous measurements of the detector parameters. The agreement here is tolerable.

Even after the detector parameters had been measured, it remained to be shown that they would not change with time. Mayer [1961] has reported that the depths of some Li-drift diodes change with time if the applied voltage is removed. This was observed by measuring the capacitance of the diode, which is inversely proportional to the depth, and watching it change.

Two tests were made on the spare diodes not selected for flight. In a short-duration test, a high bias voltage was applied

to several diodes for a period of days, and then removed. The diodes were then exposed to temperatures up to 60°C for several hours, and the capacitance was checked periodically. No change was observed. A long-duration test was made by remeasuring the capacitance of the spare detectors after a year of storage. Again, there was no change. On this evidence it is felt that the detectors are stable in time.

4. Calibration in a High-Energy Beam.

On each of the five telescopes made with measured detectors, the discrimination levels were adjusted to give energy channel cutoffs close to 25, 35, and 60 MeV. One of the units, an SUI prototype, was placed in a high energy proton beam to test the accuracy of these settings and to confirm the operation of the telescope.

The source of protons was the 40 MeV beam of the linear accelerator at the University of Minnesota. The proton energy was controlled below 40 MeV by inserting different thicknesses of aluminum. In order to avoid the primary beam intensity a thin tantalum target was placed in the beam and the elastically scattered protons were viewed at an angle of 20° . A monitor detector placed opposite the SUI detector at 20° to the beam

recorded the beam intensity and energy profile. The geometry of the experiment is shown in Figure 33.

Figure 34 shows the spectra obtained by the monitor detector at each absorber position. The range-energy curve derived from these peaks and the absorber thicknesses fit the handbook values perfectly, proving that the absorber produced the desired variation in beam energy. The scattering foil introduced no appreciable energy degradation, the nucleus being too heavy to rebound, and the foil too thin for ionization losses. The average energy at each absorber position is considered known to within plus or minus 0.1 MeV.

The counting rates from the three channels were recorded at each setting of absorber thickness. As the beam intensity monitor did not give reproducible results, it was not possible to normalize the total counting rates from one run to another, and the data must be interpreted as relative channel efficiencies at each absorber setting. These efficiencies are graphed in Figure 35 alongside the beam profile at each absorber position.

The data traces out two channel cutoffs, with 50% points at 33.5 MeV and 24.5 MeV. This compares quite favorably with the expected values of $34 \pm .5$ and $24.7 \pm .5$ MeV calculated from

the measured detector parameters and discrimination levels.

Other noticeable features of the data are the gradual discrimination edges, which contrast with those of detector B, and the residual efficiency (about 5%) of channel one at high energies.

It seems worthwhile to emphasize the significance of this experiment. It is the only direct test of the detector, a rather complicated instrument claiming exact calibration, with the kind of particles it is built to count. The successful result verifies the design and justifies the means used to calibrate the instrument.

VI. DETECTOR SUMMARY AND FLIGHT DATA

1. Detector and Flight Review.

A summary follows, containing the most important information on the Relay and EOGO proton counters and their orbits.

Relay Satellite

Orbit: Inclination = 47.5°
 Perigee = 1300 km
 Apogee = 7500 km
 Anomalistic Period = 185 Minutes

Launches: First launch 12/14/62 (successful)
 Second launch planned late 1963
 Third launch proposed

Detector B (orbited 12/14/62)

Geometric factor = $.0136 \text{ cm}^2\text{-ster}$
 Foil thickness = $1.115 \text{ mg/cm}^2 \text{ (air)}$
 Electronic discrimination levels:

B_α = 0.872 MeV
 B_β = 1.41 MeV
 B_γ = 2.105 MeV
 B_δ = 3.84 MeV

Proton Ranges:

Range One: 1.1 to 1.6 MeV and
 7.1 to 14 MeV

Range Two: 1.6 to 2.25 MeV and
 4.75 to 7.1 MeV

Range Three: 2.25 to 4.74 MeV

Shielding:

8.5 gm/cm^2 in sides and back

Temperature coefficient:

$\pm 10\%$ from 0° C to $+50^\circ \text{ C}$

Detector C (orbited 12/14/62)

Geometric factor = $0.15^* \text{ cm}^2\text{-ster}$

Proton Ranges:

Range One: 18.2 to 25 MeV

Range Two: 25 to 35 MeV

Range Three: 35 to 63 MeV

Temperature Coefficient:

$\pm 10\%$ from 0° C to $+50^\circ \text{ C}$

EOGO

Orbit: Inclination = 30°
 Perigee = 280 km
 Apogee = 110,000 km

Launches: First launch planned for 1964
 Second and third launches planned

Detector H (unit A)

Geometric factor = $0.011 \text{ cm}^2\text{-ster}$

Foil thickness = 0.20 mg/cm^2 (air)

Electronic discrimination levels:

H_α : 418 keV

H_β : 836 keV

Proton ranges:

Channel α : 490 keV to 7^* MeV

Channel β : 880 keV to 3^* MeV

Prescalers:

Channel α : x 32

Channel β : x 4

Power drain: 180 mw

Weight: 190 grams

Temperature coefficient:

$\pm 8\%$ from -40° C to $+50^\circ \text{ C}$

* Preliminary

2. The Relay Magnetometer Scheme.

The trapped radiation is not isotropic, but is rather disc-shaped, and most intense in the plane perpendicular to the magnetic line of force. Interpretation of the data from a directional detector is then complicated by the detector orientation. On the Relay satellite, both practical and analytical advantages are gained from measuring the fluxes perpendicular to the magnetic line of force.

As the Relay satellite is spinning, the detectors, which are mounted facing radially outward, cross the plane of peak intensity twice per revolution. It is a simple matter for a directional magnetometer, also facing radially outward, to detect the null magnetic field in this plane. The magnetometer then gates the accumulators so that the detector counting rates are recorded only when the detectors are perpendicular to the line of force. The details of this scheme, which was devised by Carl McIlwain, are explained in Enemark's thesis [1962].

As the foreground to background ratio is unfavorable when the detector is looking away from the maximum, and favorable when the detector is looking into the maximum, a gain on the omnidirectional background is obtained. This is the advantage

referred to in section IV 1 (a), and is typically again of about three.

Analytically, the gating scheme yields measurements of the directional intensity perpendicular to the line of force, $j_n(B)$, where B is the local scalar value of the magnetic field. If a set of measurements is obtained at different values of B along the entire length of a line of force, then the angular distribution at any point along the line of force can be obtained by use of the relation

$$j(B, \alpha) = j_n(B/\sin^2 \alpha)$$

where α is the angle to the line of force. The omnidirectional intensity can then be obtained by integration.

3. Relay Flight Data.

Since their launch on December 14, 1962, the detectors aboard Relay I have given every evidence of faultless performance. It seems fitting to end this paper with a look at some of the data obtained on the launch day, to illustrate the capabilities and performance of the Relay detectors.

Figure 36 shows the proton fluxes as a function of time from the six channels of detectors B and C during a pass across the

equator. The data is preliminary in that the detector B results are not corrected for the contributions from the dE/dx ranges, and the detector C geometric factor is a rough calculation. Nevertheless the value of these instruments for measuring the trapped particle fluxes is apparent. Relay I has operated successfully since launch, and continues to send back data at this writing (July, 1963). It is possible that, with long-lived satellites and several flights, a complete map can be made of particle fluxes throughout the earth's inner radiation belt.

Energy spectra of the trapped particles are shown in Figure 37 to illustrate the dynamic range and spectral definition of the detectors. Analysis of this data throughout the inner zone should be of immense value in determining trapped proton source and loss mechanisms.

Use of channel B3' (see section IV 1 (e)) as an alpha particle detector may shed further light on the source of the inner zone.

In conclusion, it is felt that these detectors have proven their worth and reliability, and that they will have a significant impact on the understanding of energetic particle phenomena near the earth and in space.

BIBLIOGRAPHY

- Amsel, G., P. Baruch, and O. Smulkowski, "High Resolution Study of Nuclear Radiations by P-N Junction Detectors", Proceedings of the Gatlinburg Conference, 1961.
- Bethe and Ashkin, Experimental Nuclear Physics, Volume 1, E. Segre, ed. (1953).
- Blankenship, J. L., and C. J. Borkowski, "Silicon Surface-Barrier Nuclear Particle Spectrometer", Proceedings of the Seventh Scintillation Counter Symposium, 1960.
- Blankenship, J. L., and C. J. Borkowski, "Improved Techniques for Producing P^+-I-N^+ Diode Detectors", Proceedings of the Eighth Scintillation Counter Symposium, 1962.
- Bloom, S. D., L. G. Mann, and H. L. West, "Preliminary Report on LRL Discoverer Piggyback Electron Spectrometer Experiment", October 27, 1961.
- Bromley, D. A., "Semiconductor Detectors in Nuclear Physics", Proceedings of the Asheville Conference, 1961.
- Brown, W. L., "Properties of Space Charge Regions", Proceedings of the Asheville Conference, 1961A.
- Brown, W. L., "Introduction to Semiconductor Particle Detectors", Proceedings of the Gatlinburg Conference, 1961B.
- Brown, W. L., and J. D. Gabbe, "The Electron Distribution in the Earth's Radiation Belts during July 1962 As Measured by Telstar", J. Geophys. Research 68, 607-618 (1963).

BIBLIOGRAPHY (continued)

- Chase, R. L., W. A. Higinbotham, and G. L. Miller, "Amplifiers for Use with P-N Junction Radiation Detectors", Proceedings of the Gatlinburg Conference, 1961.
- Chromium Corporation of America, P. O. Box 1229, Waterbury 20, Connecticut.
- Cottini, C., E. Gatti, G. Gianelli, and G. Rozzi, "Minimum Noise Preamplifier for Fast Ionization Chambers", *Il Nuovo Cimento* 3, 473 (1956).
- Dabbs, J. W. T., and F. J. Walter, ed., "Semiconductor Nuclear Particle Detectors" (Proceedings of the Asheville Conference), NAS/NRC Publication 871, Washington, D. C., 1961.
- Elmore, W. C., and M. Sands, Electronics, McGraw-Hill, New York, 1949, p. 154.
- Emmer, T. L., "Low Noise Transistor Amplifiers for Solid State Detectors", Proceedings of the Gatlinburg Conference, 1961.
- Enemark, D. C., "Electrical Design of the Radiation Effects Experiment for the Satellite Relay", Research Report 62-16, Department of Physics and Astronomy, State University of Iowa, 1962.
- Fairstein, E., "Considerations in the Design of Pulse Amplifiers for Use with Solid State Radiation Detectors", Proceedings of the Gatlinburg Conference, 1961.
- Fox, R. J., "Procedure for dE/dx Silicon Surface-Barrier Diodes", Proceedings of the Asheville Conference, 1961.
- Green, A. E. S., Nuclear Physics, McGraw-Hill, New York, 1955.

BIBLIOGRAPHY (continued)

- Inskeep, C. N., W. W. Eidson, and R. A. LaSalle, "Considerations in the Development and Use of Very Thin Junction Counters Suitable for $\Delta E/\Delta x$ Detection", Proceedings of the Eighth Scintillation Counter Symposium, 1962.
- Katz, L., and A. S. Penfold, "Range-Energy Relations for Electrons and the Determination of Beta-Ray End-Point Energies by Absorption", Reviews of Modern Physics 24, 28-44 (1952).
- Kittel, Charles, Introduction to Solid State Physics, 2nd Edition, John Wiley and Sons, New York 1956, p. 358.
- Leighton, R. B., Principles of Modern Physics, McGraw-Hill, New York, 1959.
- Mayer, J. W., "Pulse Formation in Semiconductor Detectors", Proceedings of the Asheville Conference, 1961.
- Mayer, J. W., N. A. Bailey, and H. L. Dunlap, "Characteristics of Ion Drifted P-I-N Junction Particle Detectors", Paper delivered to Conference on Nuclear Electronics, International Atomic Energy Agency, Belgrade, Yugoslavia, May, 1961.
- McKenzie, J. M., and G. T. Ewan, "Semiconductor Electron Detectors", Proceedings of the Gatlinburg Conference, 1961.
- Oak Ridge Technical Enterprises Corp., P. O. Box 465, Oak Ridge, Tennessee.
- Pell, E. M., "The Ion-Drift Process", Proceedings of the Asheville Conference, 1961.

BIBLIOGRAPHY (continued)

Pieper, G. F., A. J. Zmuda, C. O. Bostrom, and B. J. O'Brien,
"Solar Protons and Magnetic Storms in July 1961",
J. Geophys. Research 67, 4959-4981 (1962).

Proceedings of the Seventh Scintillation Counter Symposium, I.R.E.
Transactions on Nuclear Science, Vol. NS-7, No. 2-3, June-
September, 1960.

Proceedings of the Eighth Scintillation Counter Symposium, I.R.E.
Transactions on Nuclear Science, Vol. NS-9, No. 3, June,
1962.

Proceedings of the International Symposium on Space Phenomena and
Measurement, I.E.E.E. Transactions on Nuclear Science,
Vol. NS-10, No. 1, January 1963.

Schottky, W., "Vereinfachte und Erweiterte Theorie der Randschicht-
Gleichrichter", Z. Phys. 118, 539 (1942).

Solid State Radiation Detectors (Proceedings of the Gatlinburg
Conference), I.R.E. Transactions on Nuclear Science,
Vol. NS-8, No. 1, January, 1961.

Sproull, R. L., Modern Physics, Equation (11-7), John Wiley and
Sons, Inc., New York, 1956.

Statz, H., "Semiconductor Surface Effects", Proceedings of the
Asheville Conference, 1961.

Takaki, R., M. Perkins, and A. Tuzzolino, "A Gold-Silicon Surface-
Barrier Proton Range Telescope", Proceedings of the
Gatlinburg Conference, January, 1961.

BIBLIOGRAPHY (continued)

- Whaling, W., "The Energy Loss of Charged Particles in Matter",
Handbuch der Physik Band XXXIV (1958).
- Williams, R. L., and P. P. Webb, "The Window Thickness of Diffused
Junction Detectors", Proceedings of the Eighth Scintillation
Counter Symposium, 1962.
- Ziemba, F. P., G. Pelt, G. Ryan, L. Wang, and R. Alexander,
"Properties of an $n^+ i p^+$ Semiconductor Detector",
Proceedings of the Eighth Scintillation Counter Symposium,
1962.

FIGURE CAPTIONS

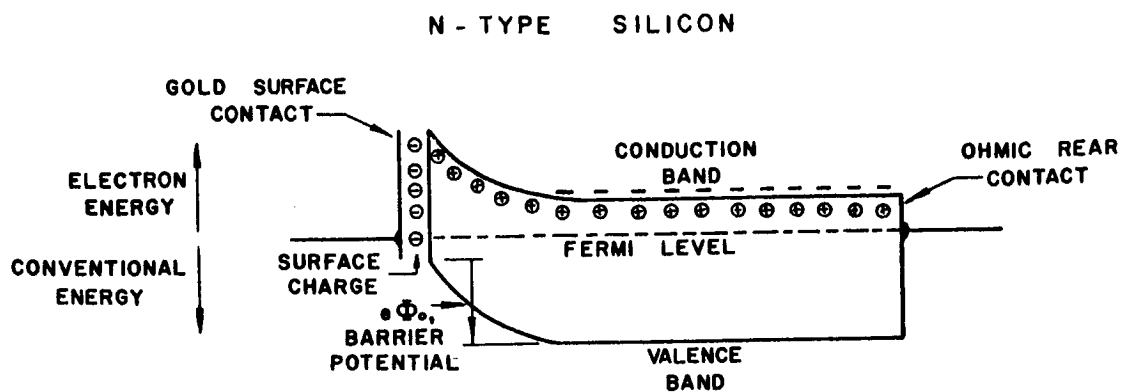
Figure
Nos.

1. Energy bands in a surface barrier detector.
2. The space-charge region.
3. Solid state detector nomograph.
4. Energy loss of charged particles.
5. Range of charged particles.
6. Detector characteristic curves.
7. Particles striking a detector.
8. Collection efficiency profile.
9. Illustration of diffusion collection.
10. Preamplifier block diagram.
11. Preamplifier schematic diagram.
12. Demonstration of charge sensitivity.
13. The resolution of a detector and preamplifier.
14. Profile of a discrimination level.
15. Block diagram for particle counting and analysis.
16. Relay detector B pulse-height analysis.
17. EOGO detector H pulse-height analysis.
18. Relay detectors B and C.
19. EOGO detector H assembly.
20. EOGO detector H.
21. Relay detector B aperture.
22. Relay on-board source and discrimination levels.
23. Determination of detector depth.

FIGURE CAPTIONS
(continued)

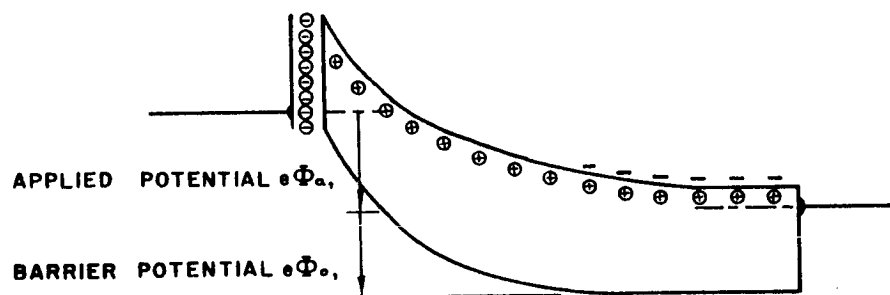
Figure
Nos.

24. Relay detector B calibration experiment.
25. Effect of electron fluxes on a discrimination level.
26. Theoretical curves of multiple coincidence counting rates.
27. Experimental curves for multiple coincidence counting rates.
28. Counting rate slope vs coincidence multiplicity.
29. Relay detector C telescope assembly.
30. Relay detector C pulse-height analysis.
31. Two-dimensional view of telescope proton analysis.
32. Determination of detector parameters.
33. Geometry for high-energy proton calibration.
34. The use of absorbers to degrade the beam energy.
35. Detector C energy channels.
36. Relay I Data: Proton fluxes near the equator.
37. Relay I Data: Proton energy spectra.



**N-TYPE SILICON SURFACE BARRIER DIODE
NO EXTERNAL BIAS**

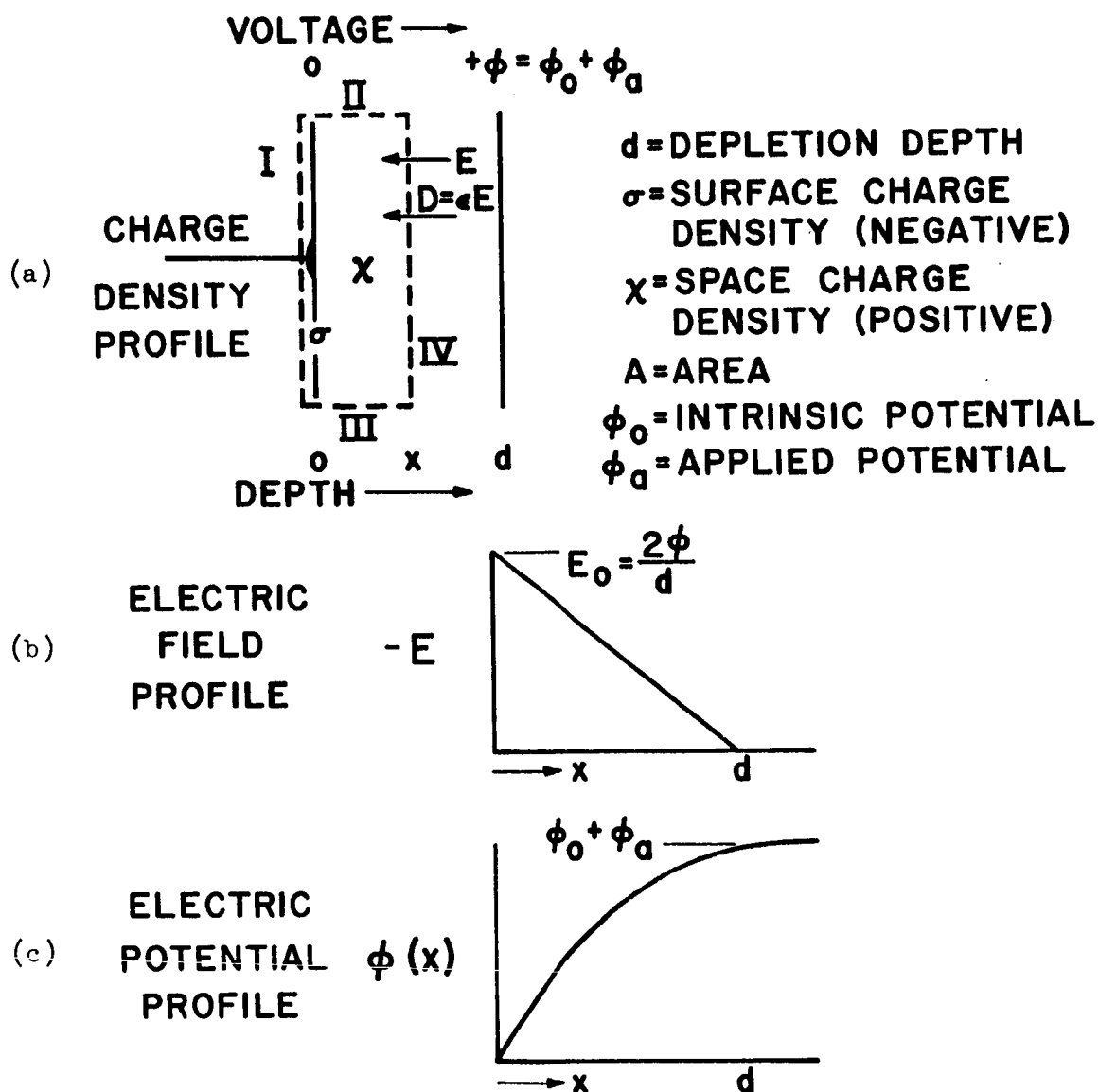
(a)



**N-TYPE SILICON SURFACE BARRIER DIODE
EXTERNAL BIAS APPLIED**

(b)

Figure 1



THE SPACE-CHARGE REGION

Figure 2 (a), (b), and (c).

SILICON DIODE NOMOGRAPH

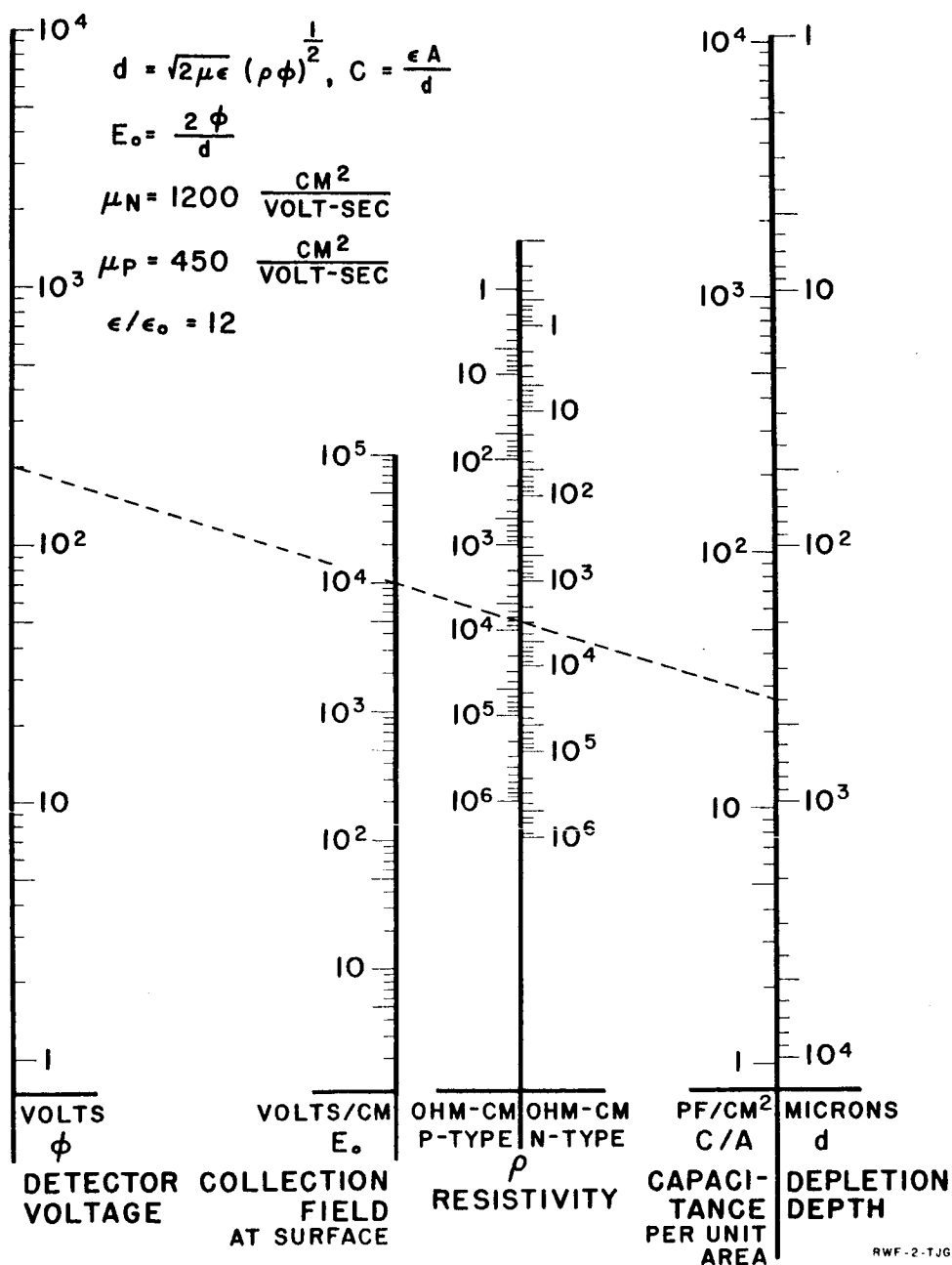


Figure 3

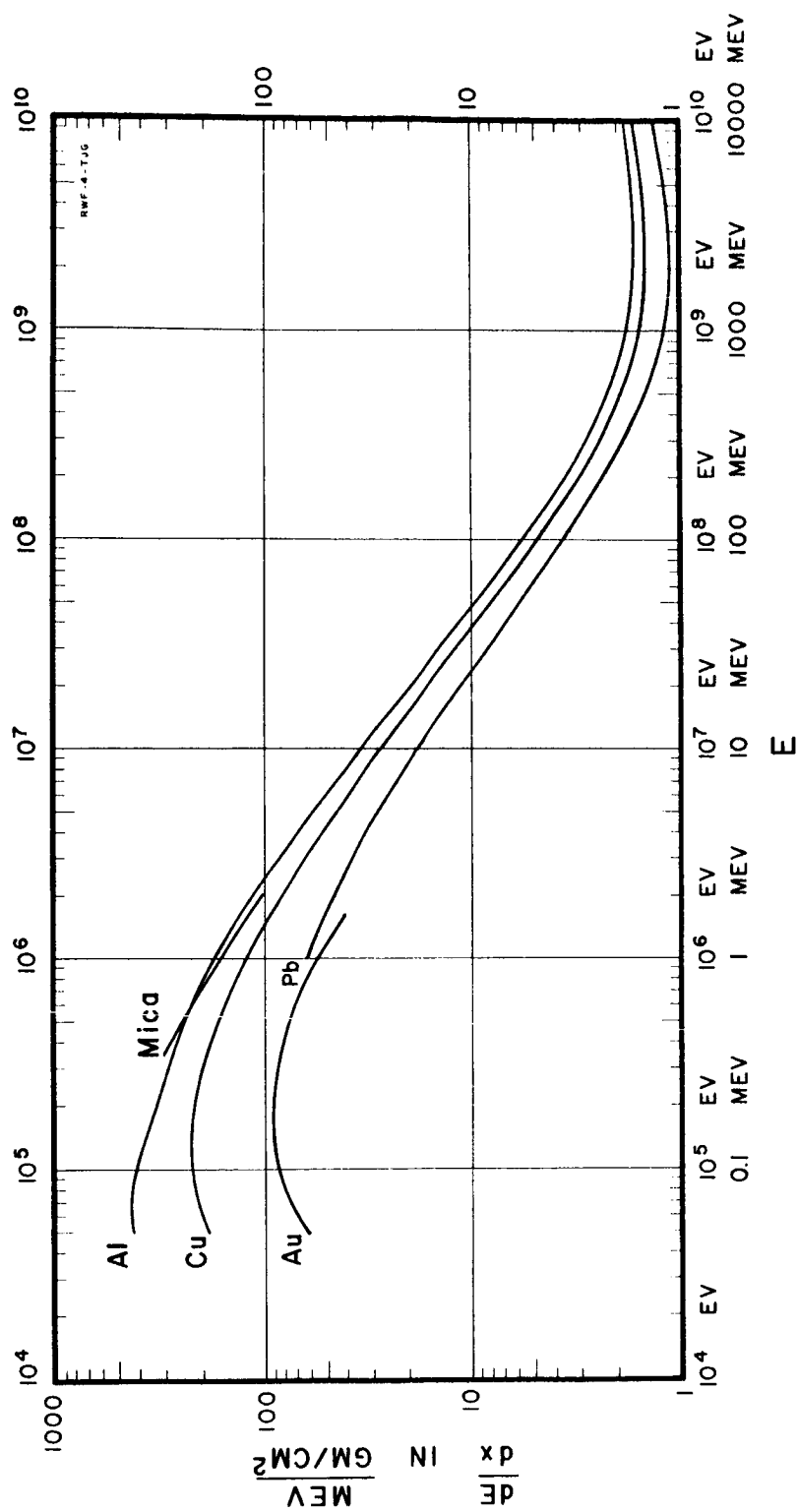


Figure 4

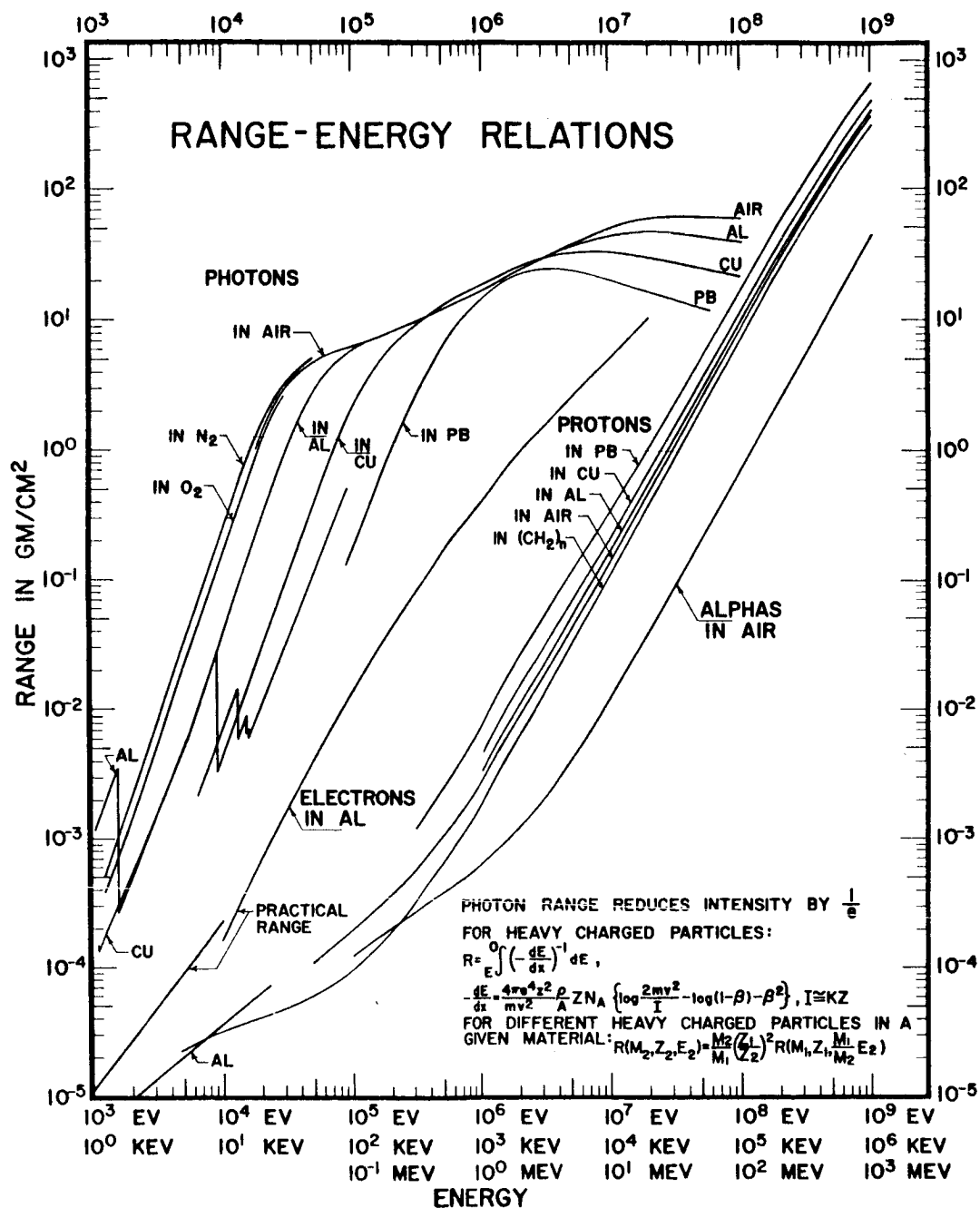


Figure 5

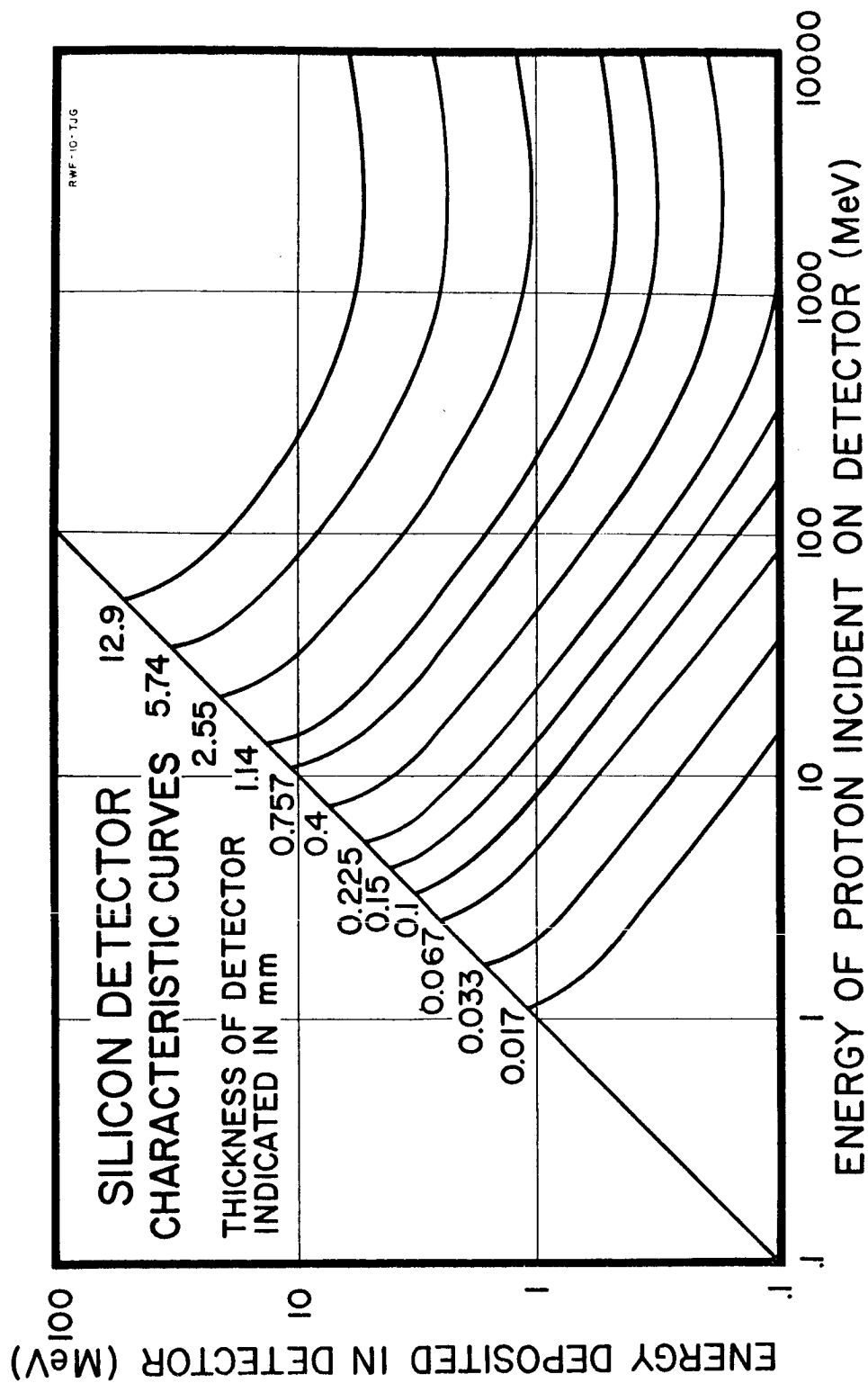


Figure 6

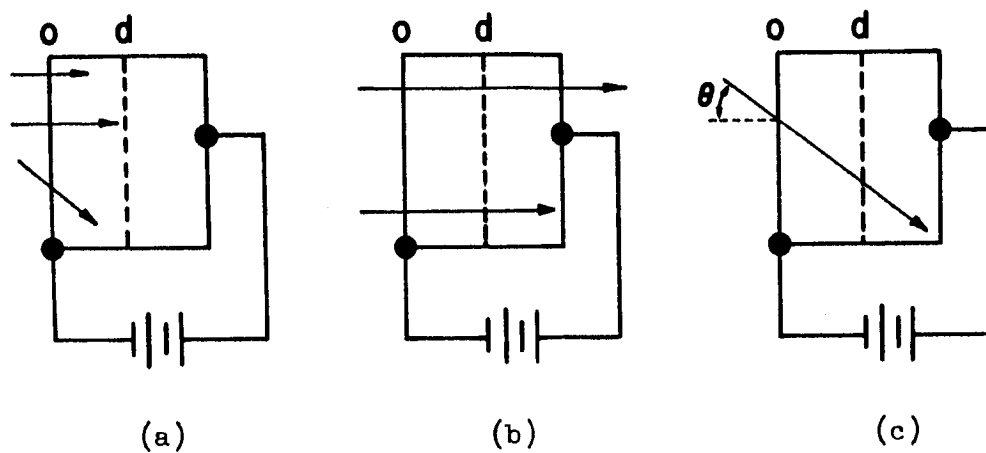


Figure 7

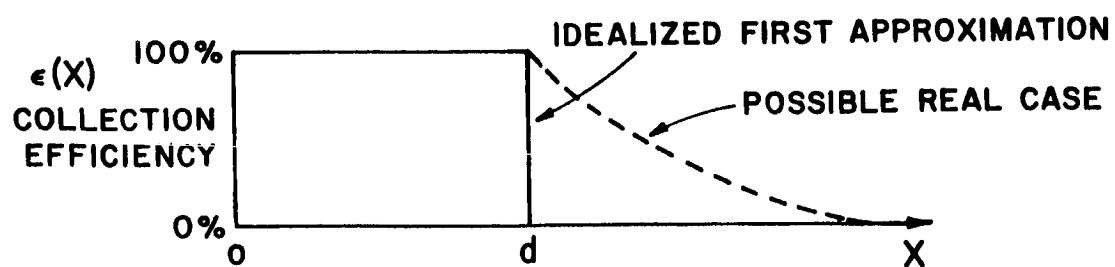


Figure 8

DIFFUSION COLLECTION IN DIODE DETECTOR

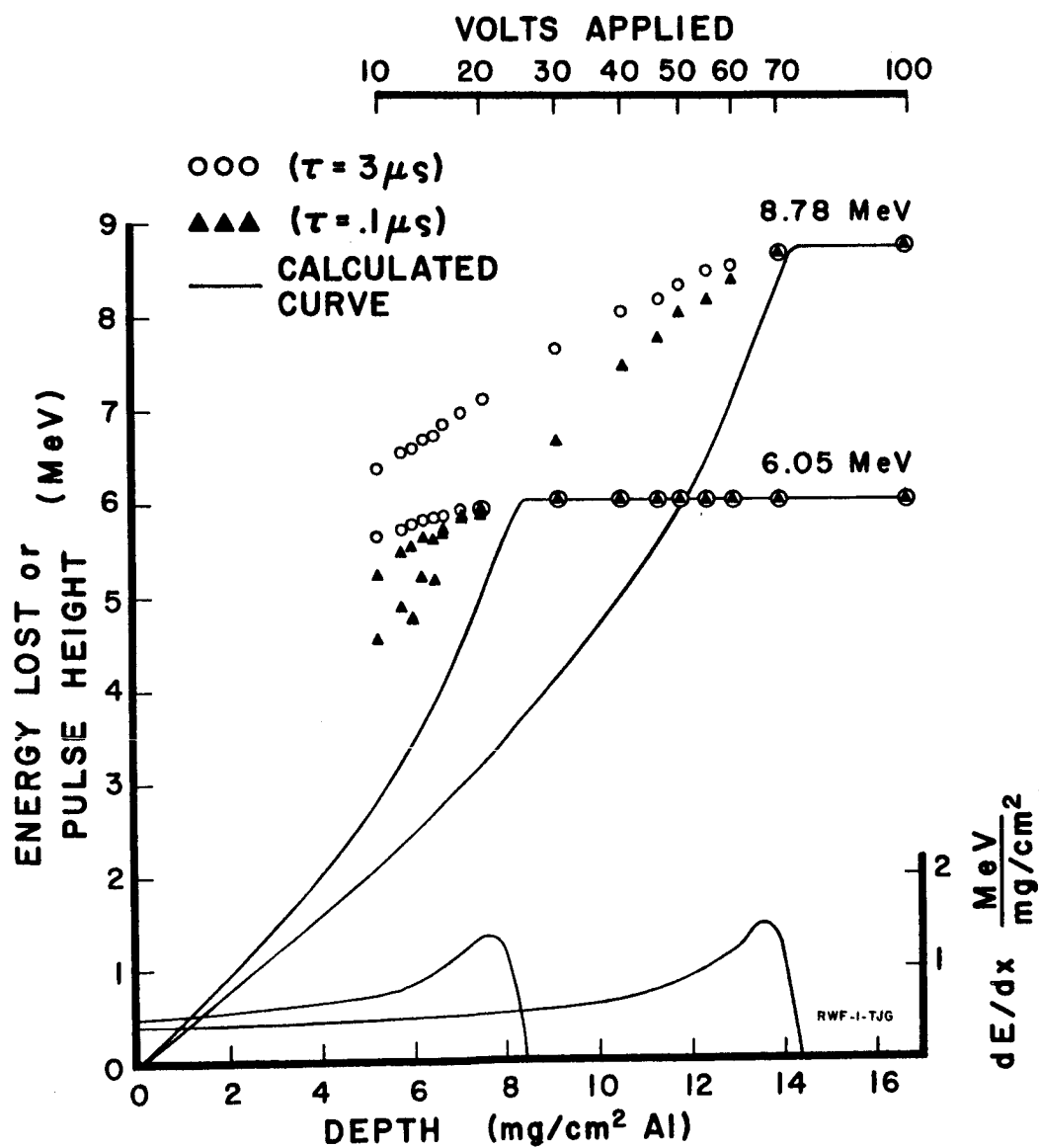


Figure 9

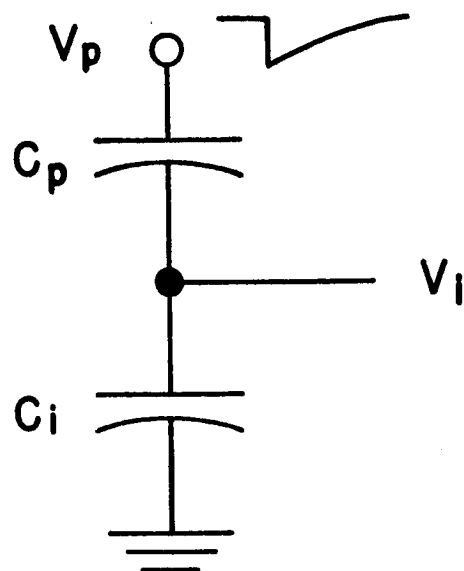


Figure 10 (a)

$$C_p \ll C_i$$

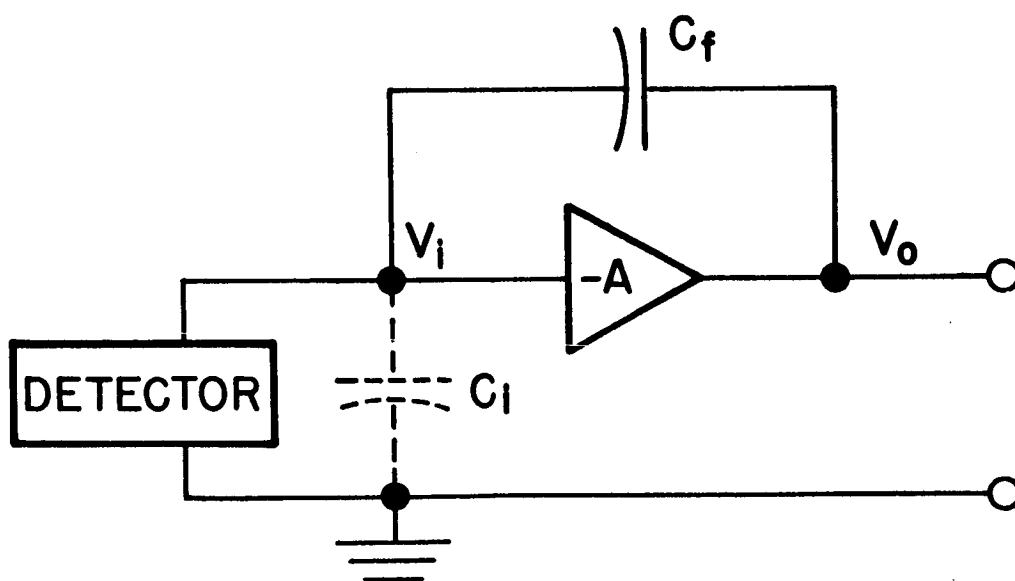


Figure 10 (b)

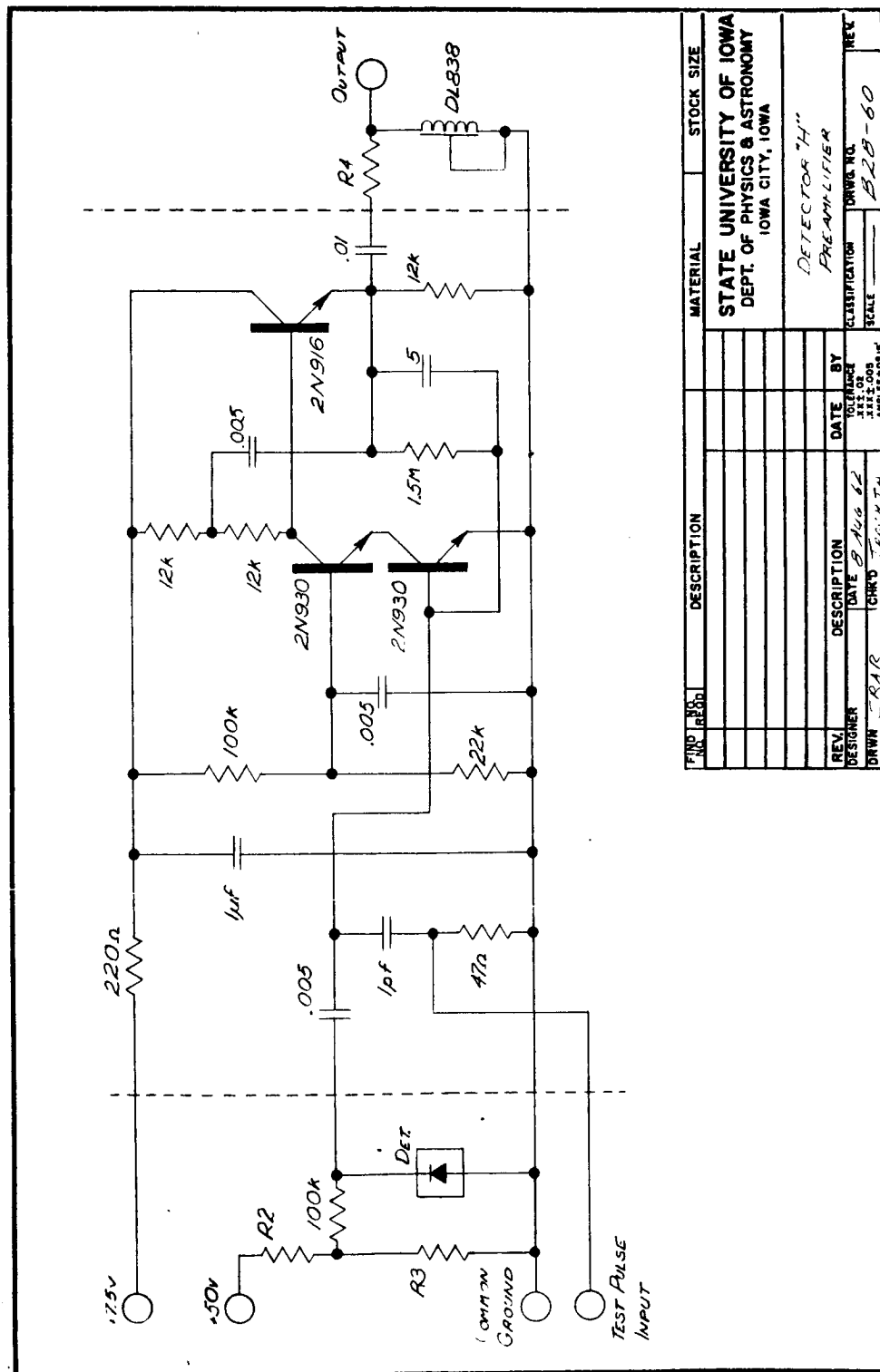


Figure 11

63-337

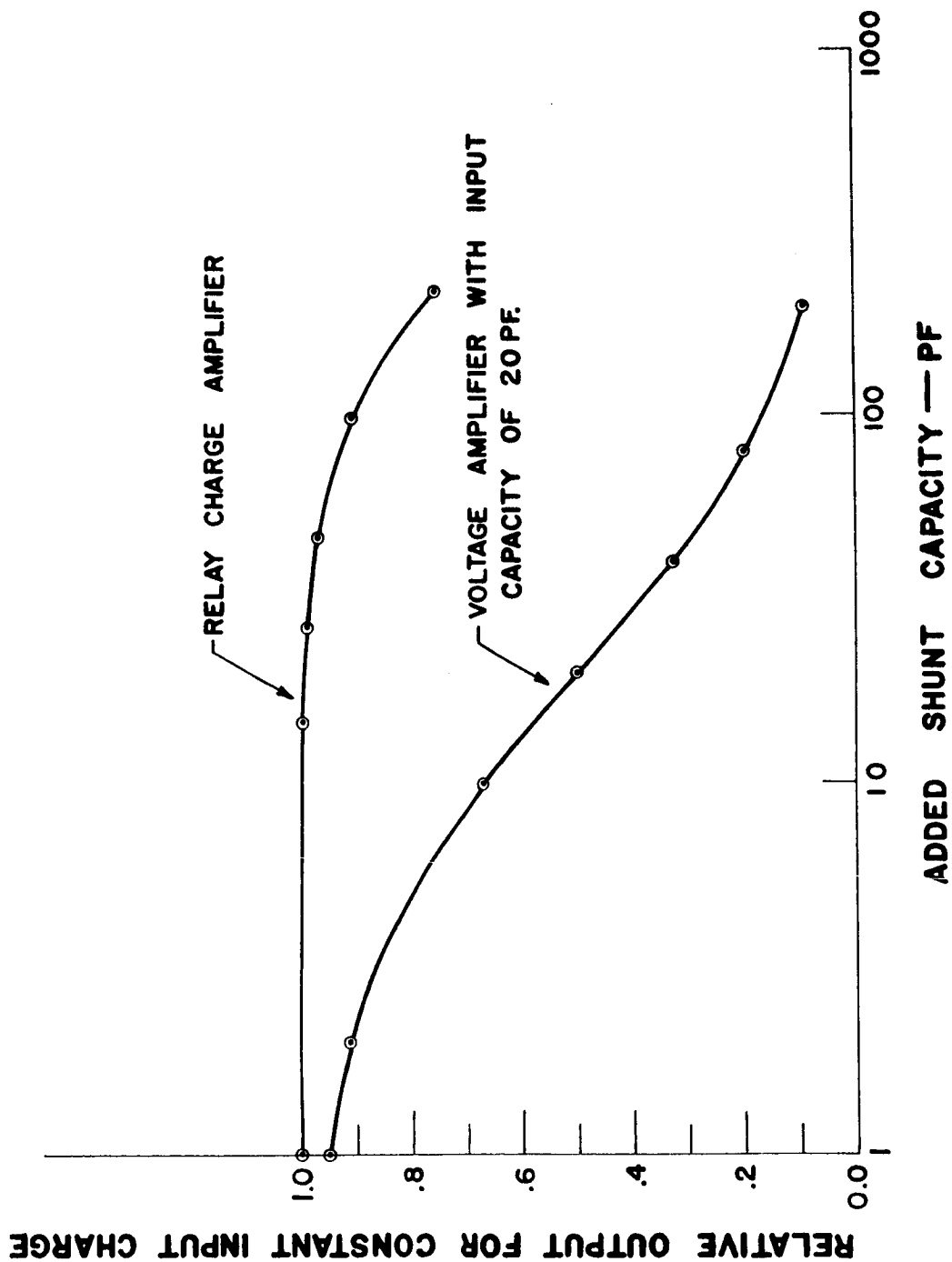


Figure 12

PREAMPLIFIER AND DETECTOR ENERGY RESOLUTION

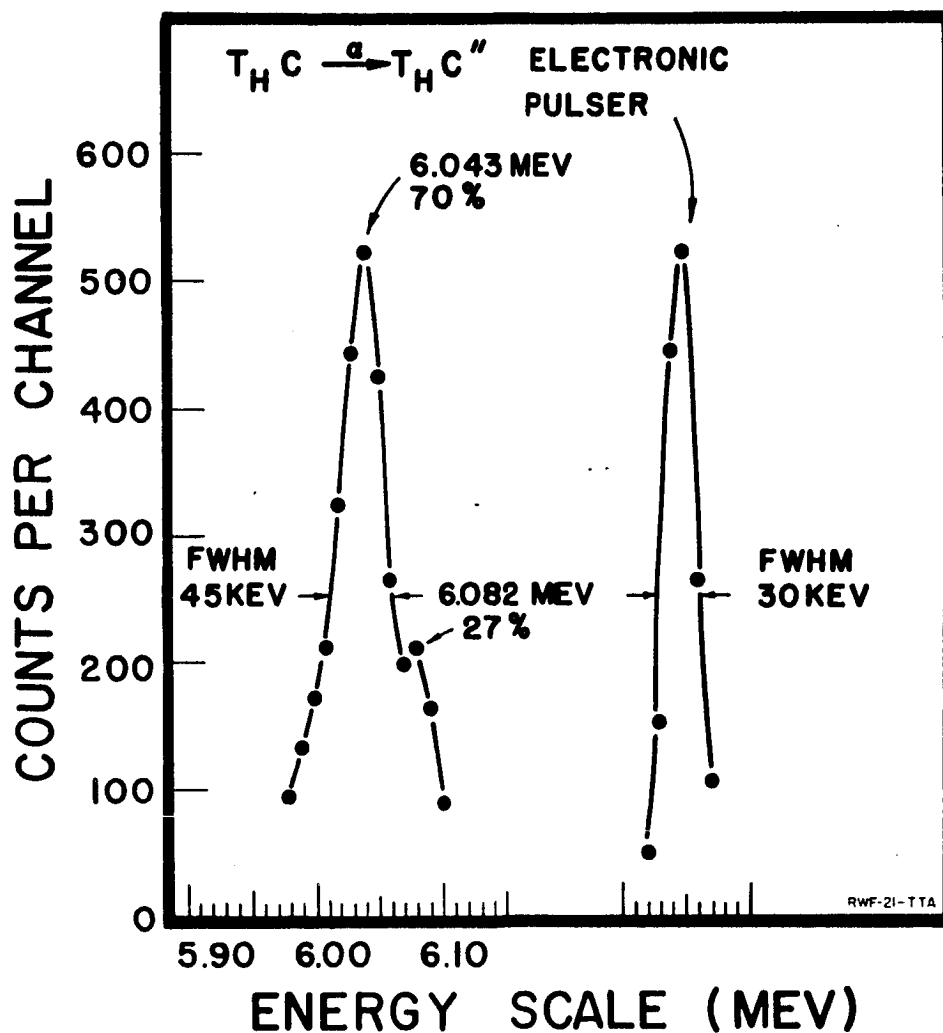


Figure 13

EOGO DETECTOR H CHANNEL α DISCRIMINATION LEVEL

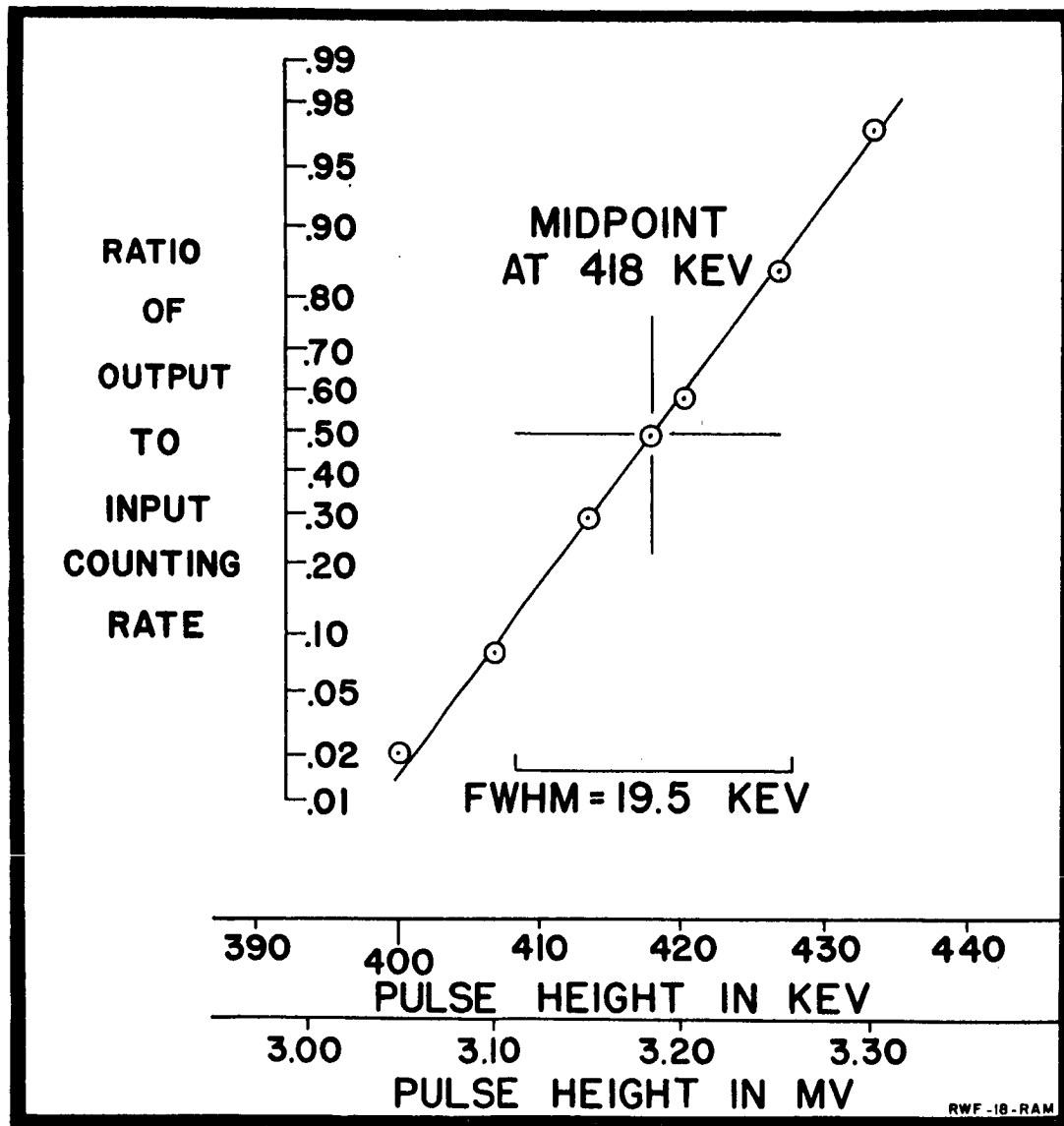
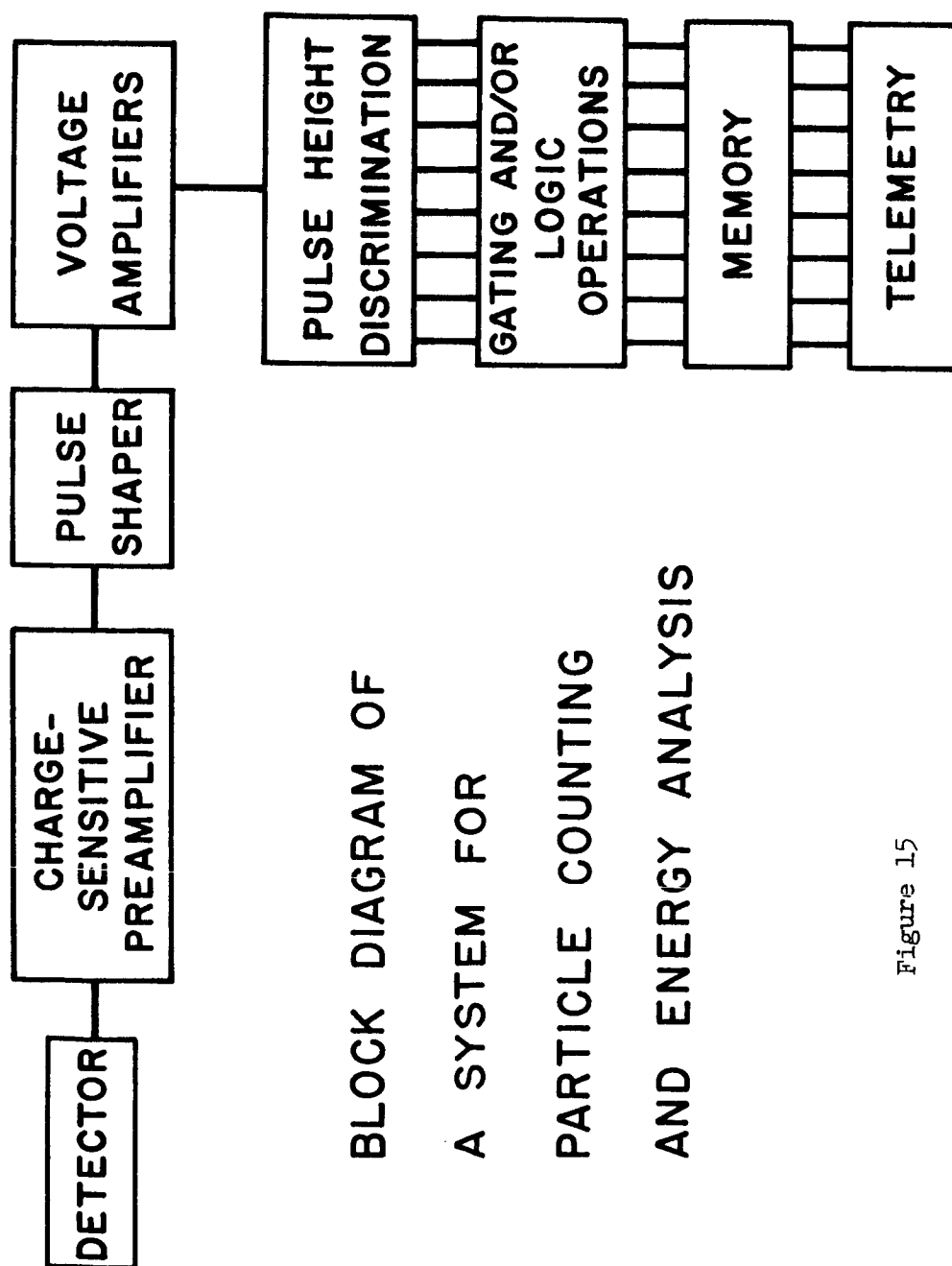


Figure 14



BLOCK DIAGRAM OF
A SYSTEM FOR
PARTICLE COUNTING
AND ENERGY ANALYSIS

Figure 15

RELAY DETECTOR B

PULSE HEIGHT ANALYSIS SCHEME

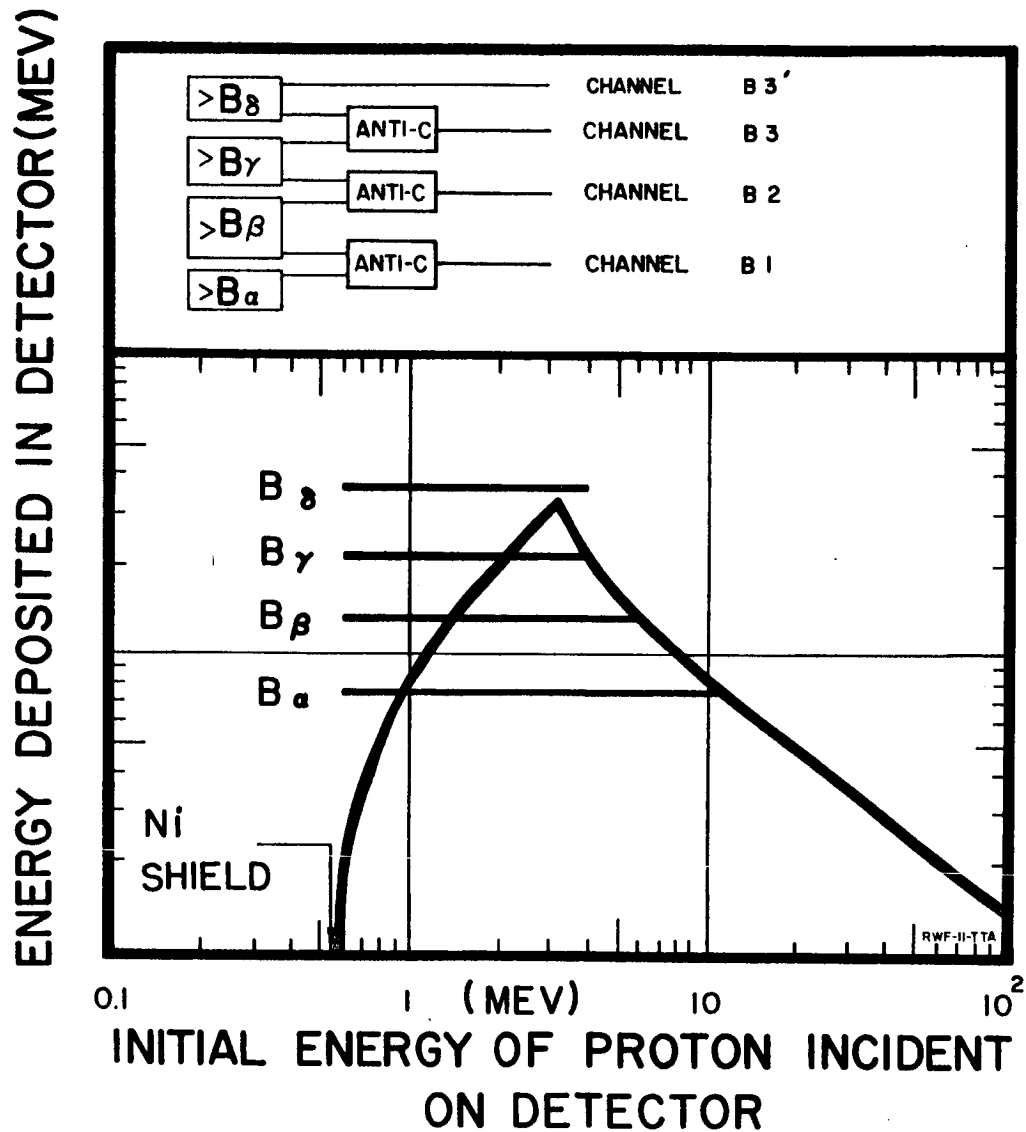


Figure 16

EOGO DETECTOR H

PULSE HEIGHT ANALYSIS SCHEME

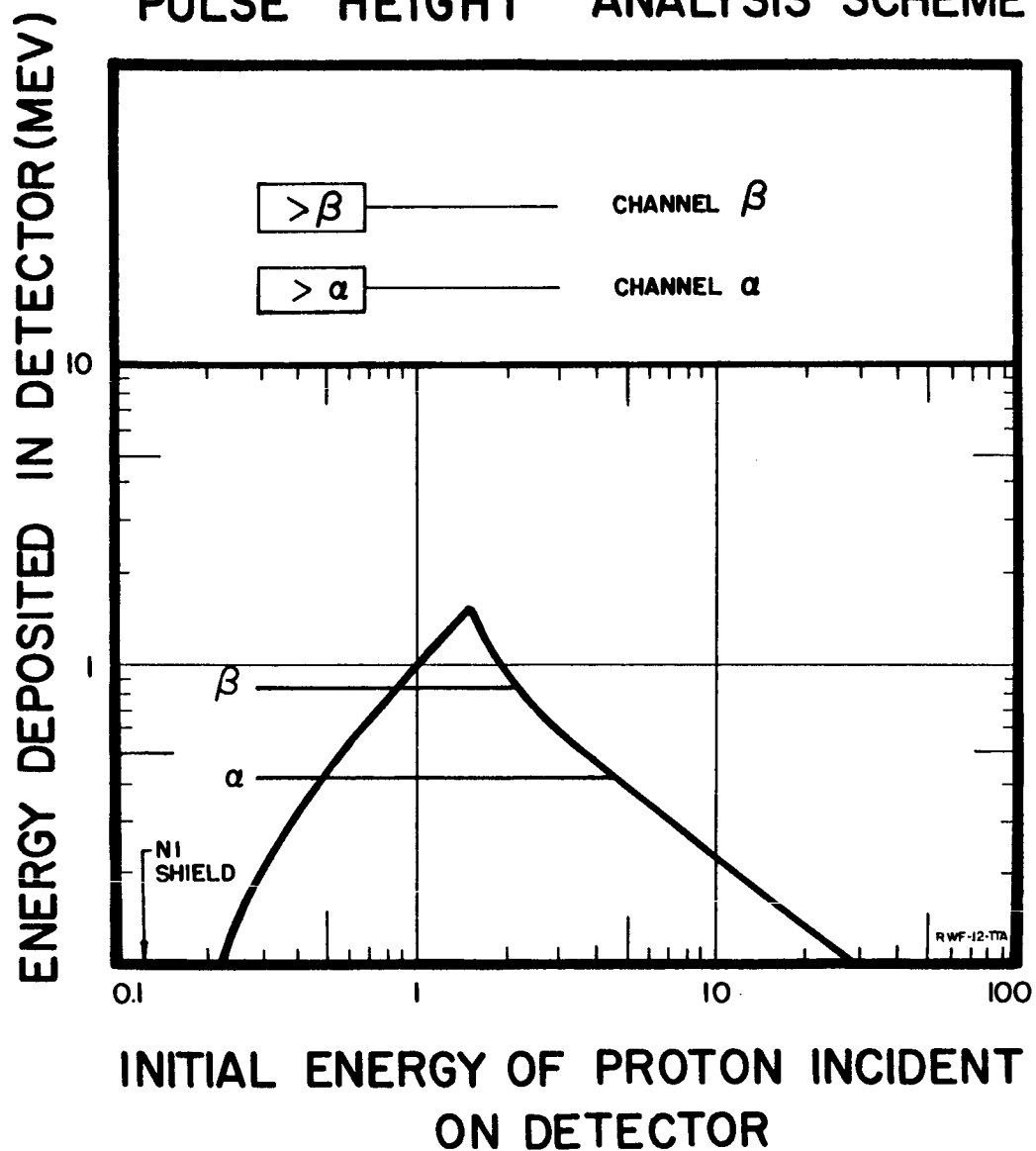
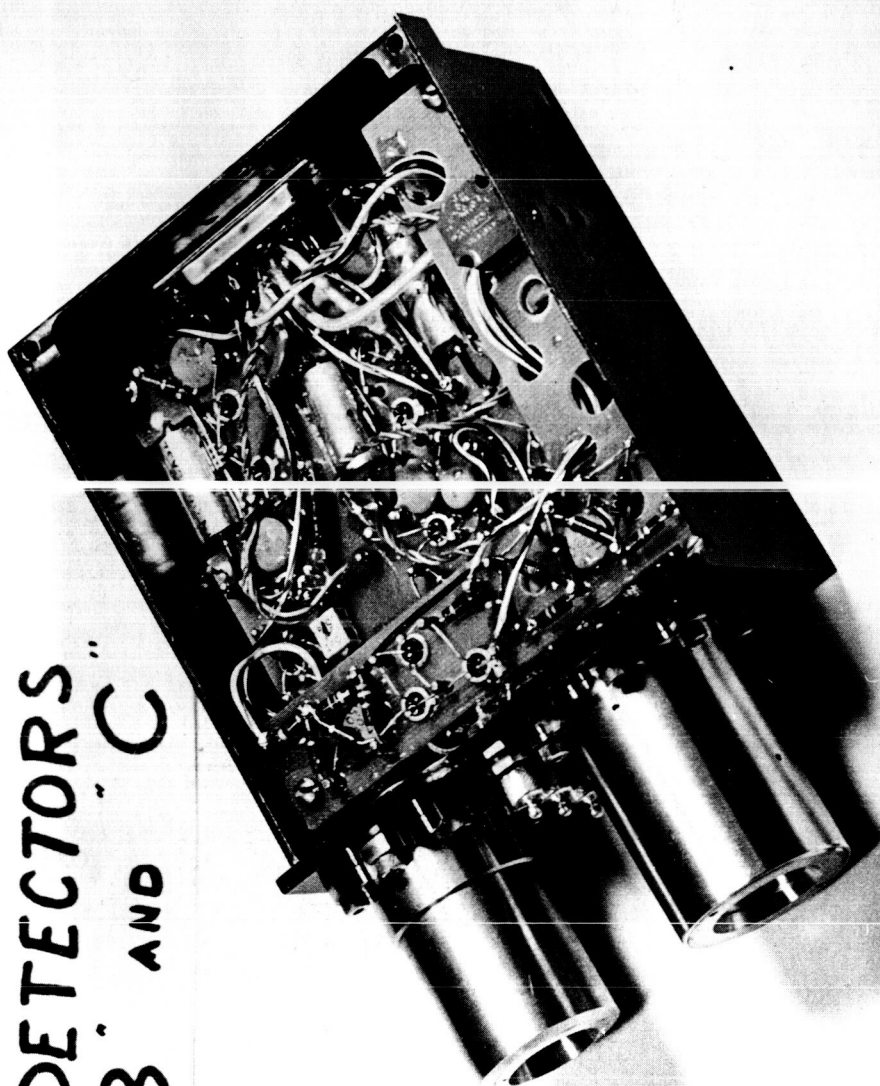


Figure 17



DETECTORS
"B" AND "C"

Figure 18

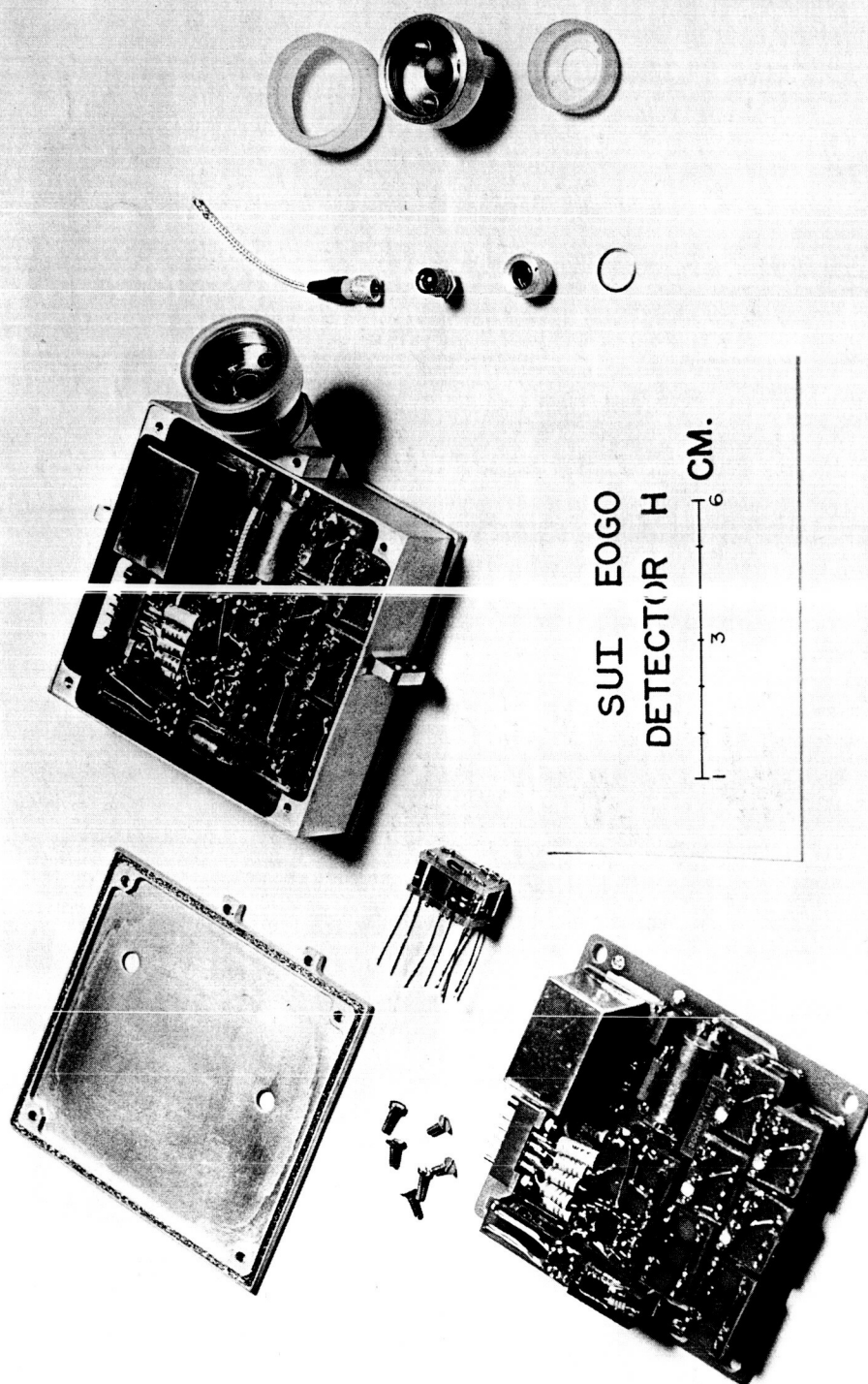


Figure 19

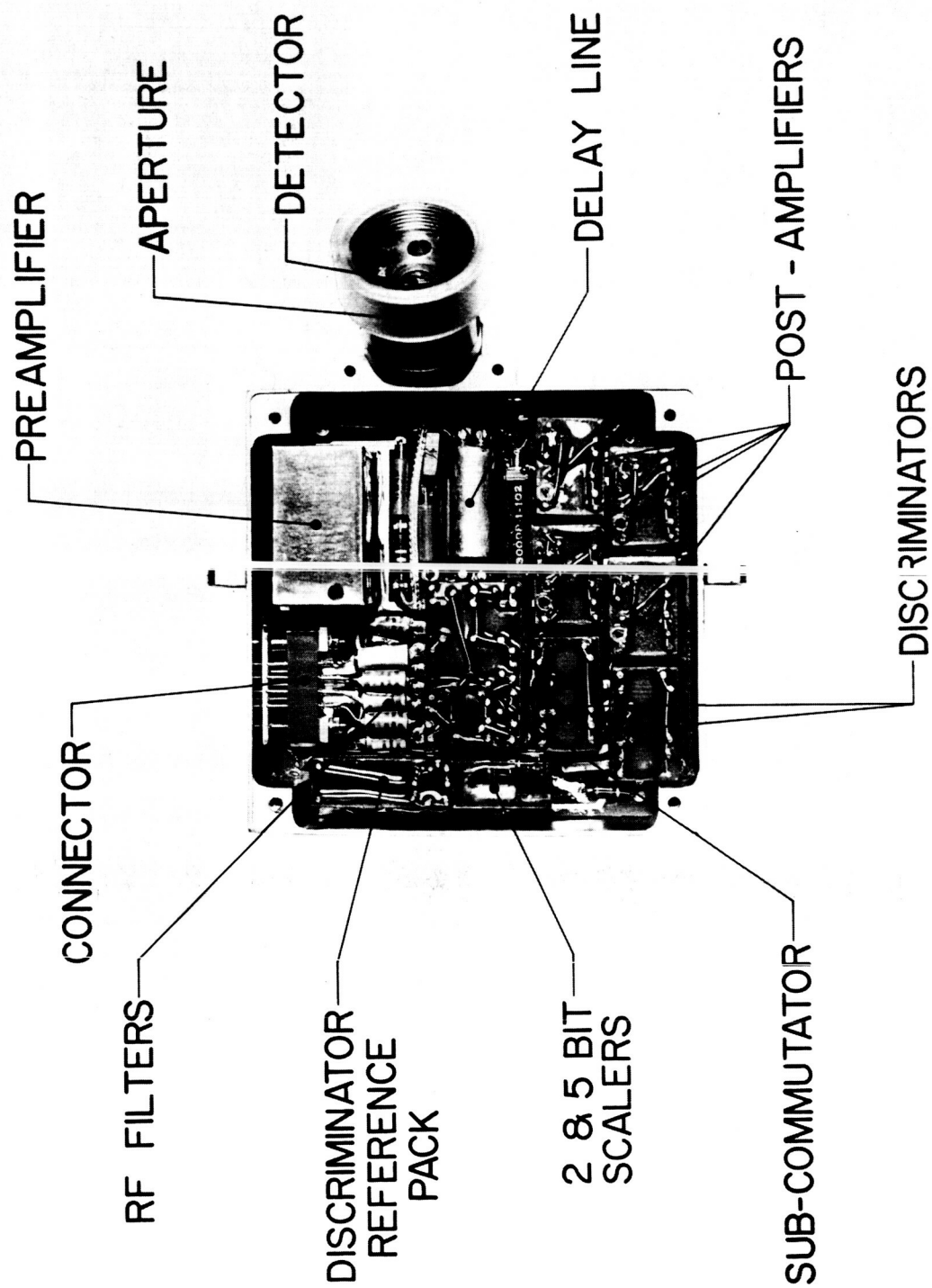
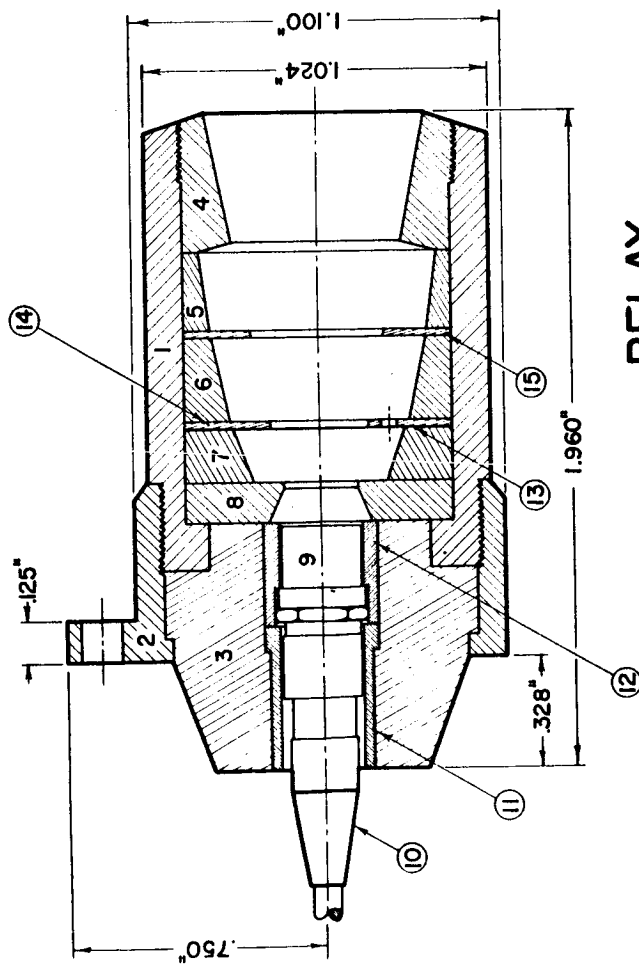


Figure 20



RELAY
Detector "B" Aperture

Figure 21

NO.	DESCRIPTION	MAT.
1	Main Housing	Brass
2	Mounting Ring	Brass
3	Rear Shield	Brass
4	Aperture Defining Ring	Brass
5	Upper Spacer	Brass
6	Second Spacer	Brass
7	Rear Spacer	Brass
8	Source Mount	Brass
9	Ortec Surface Barrier Detector	
10	Microdot Plug	Teflon
11	Connector Insulator	Teflon
12	Detector Holder	Teflon
13	Light-tight Foil	Nickel
14	Electron Baffle	Brass
15	Electron Baffle	Brass

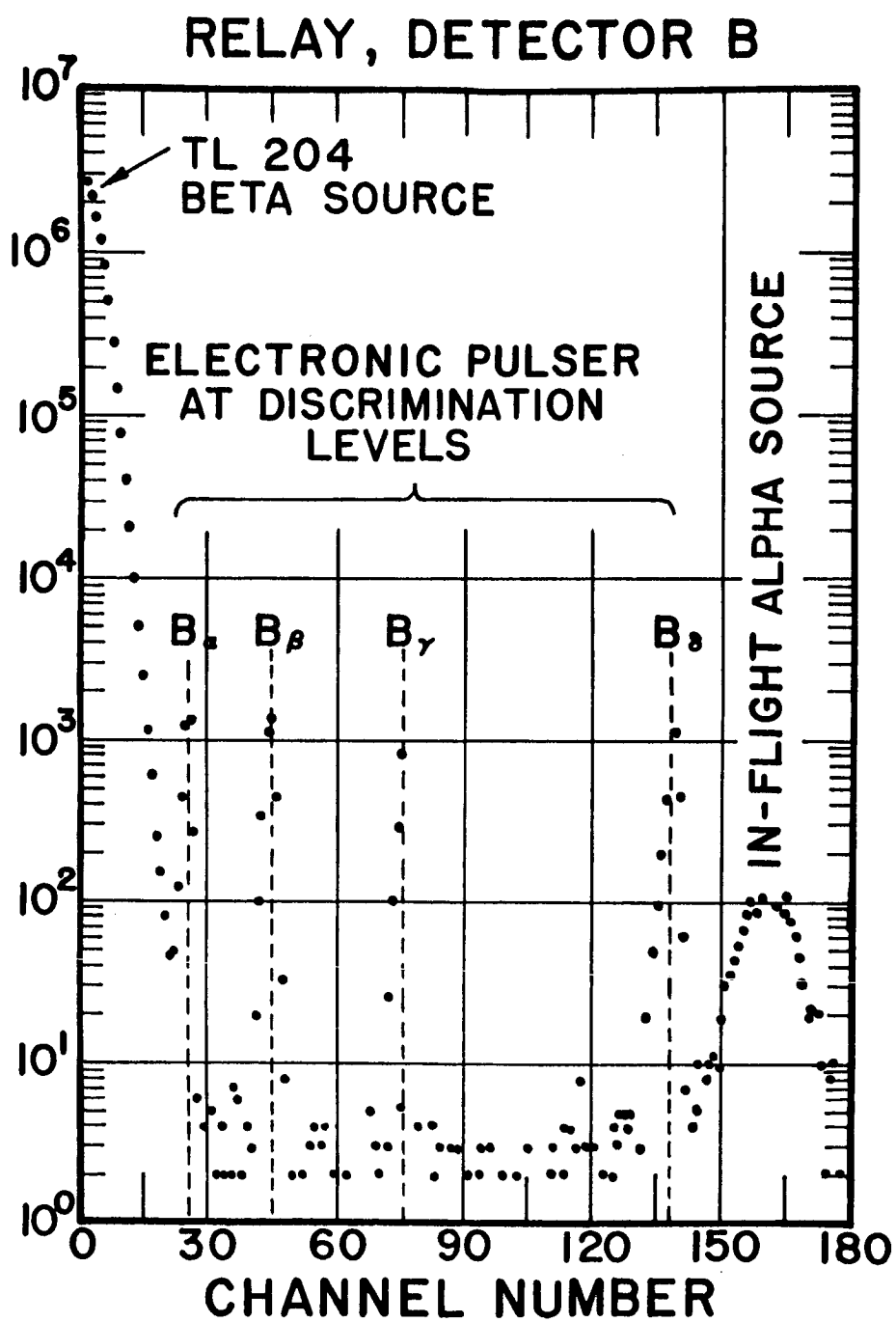


Figure 22

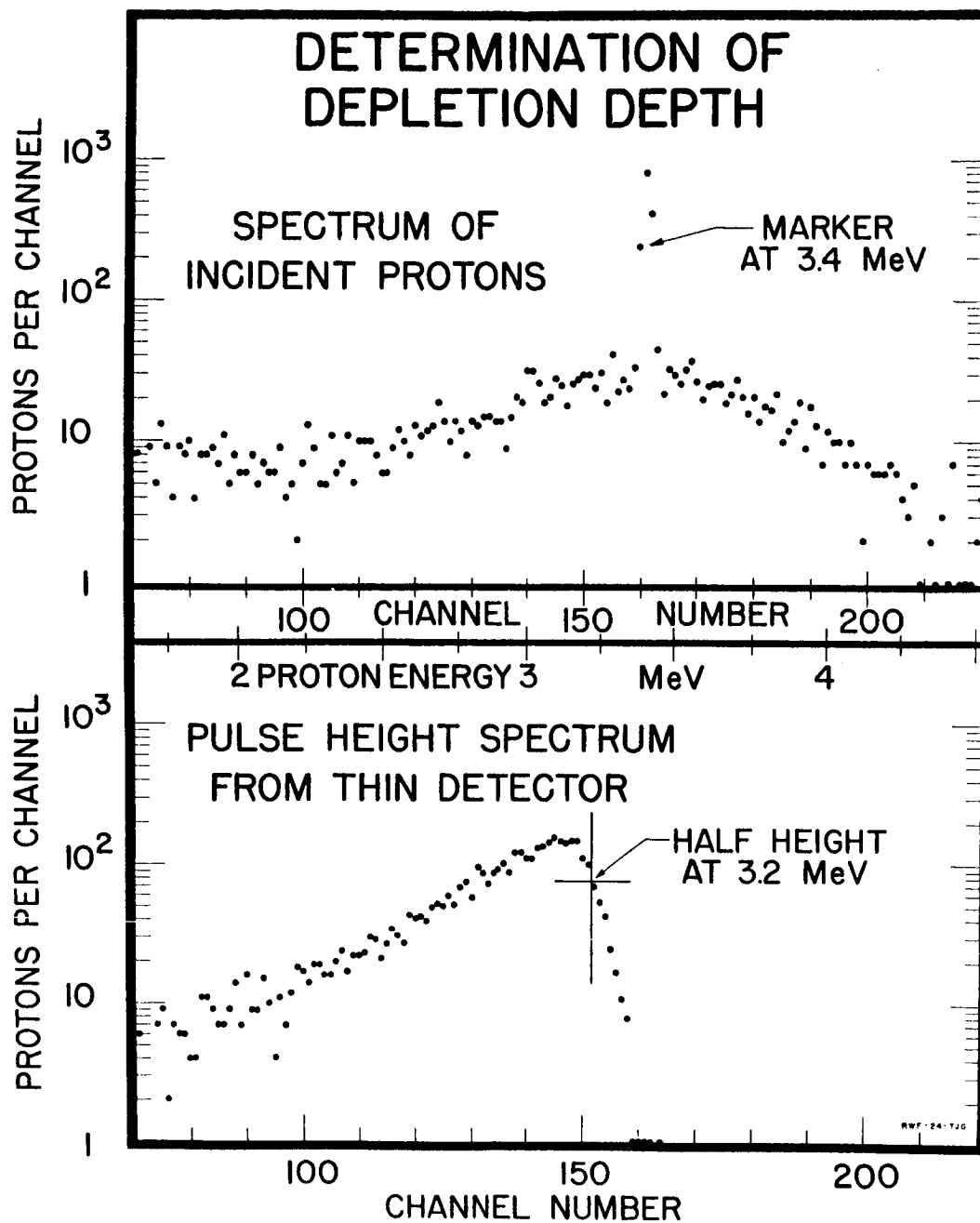


Figure 23

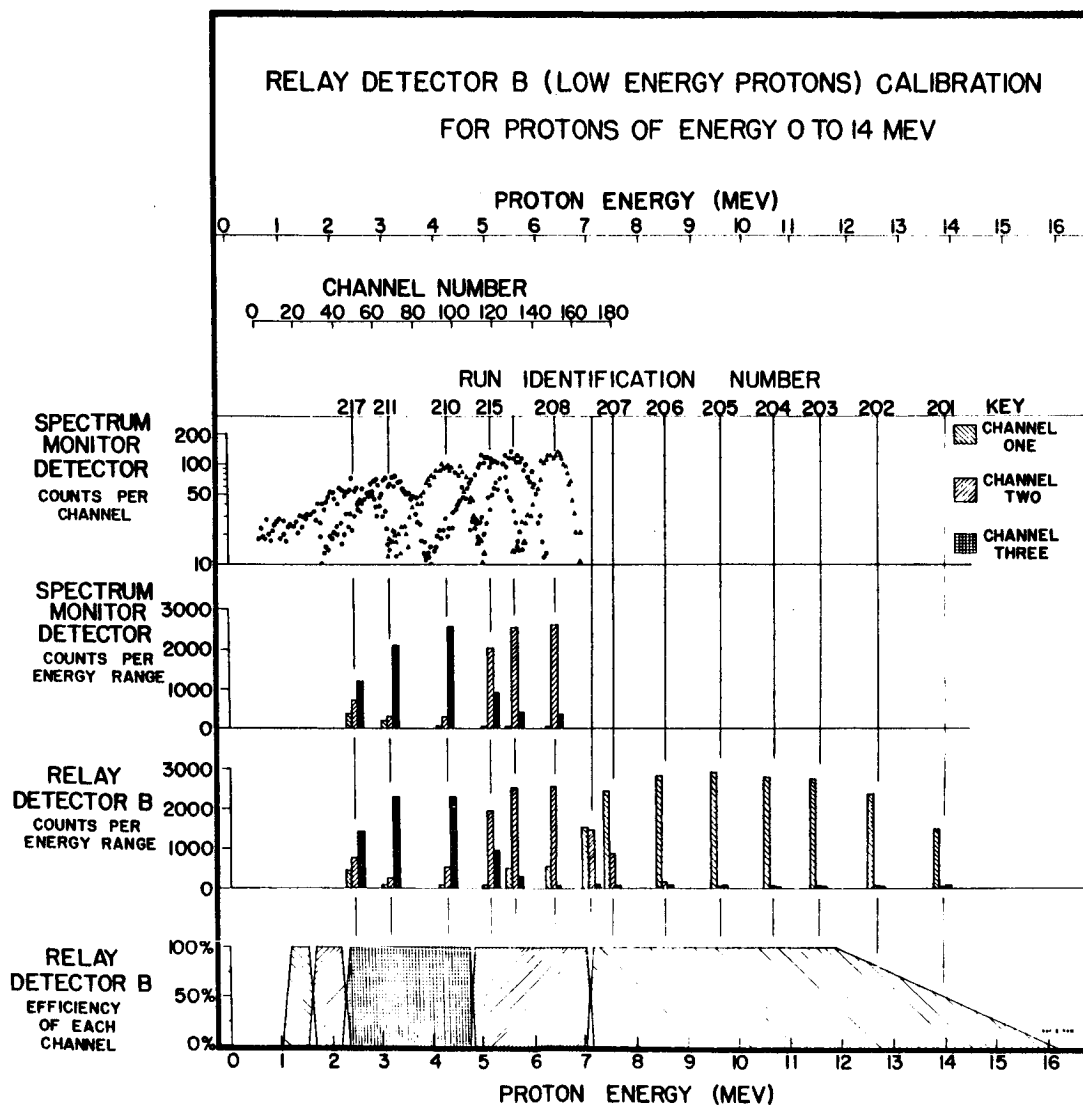


Figure 24

EFFECT OF A HIGH FLUX OF ELECTRONS ON THE LOWEST DISCRIMINATION LEVEL

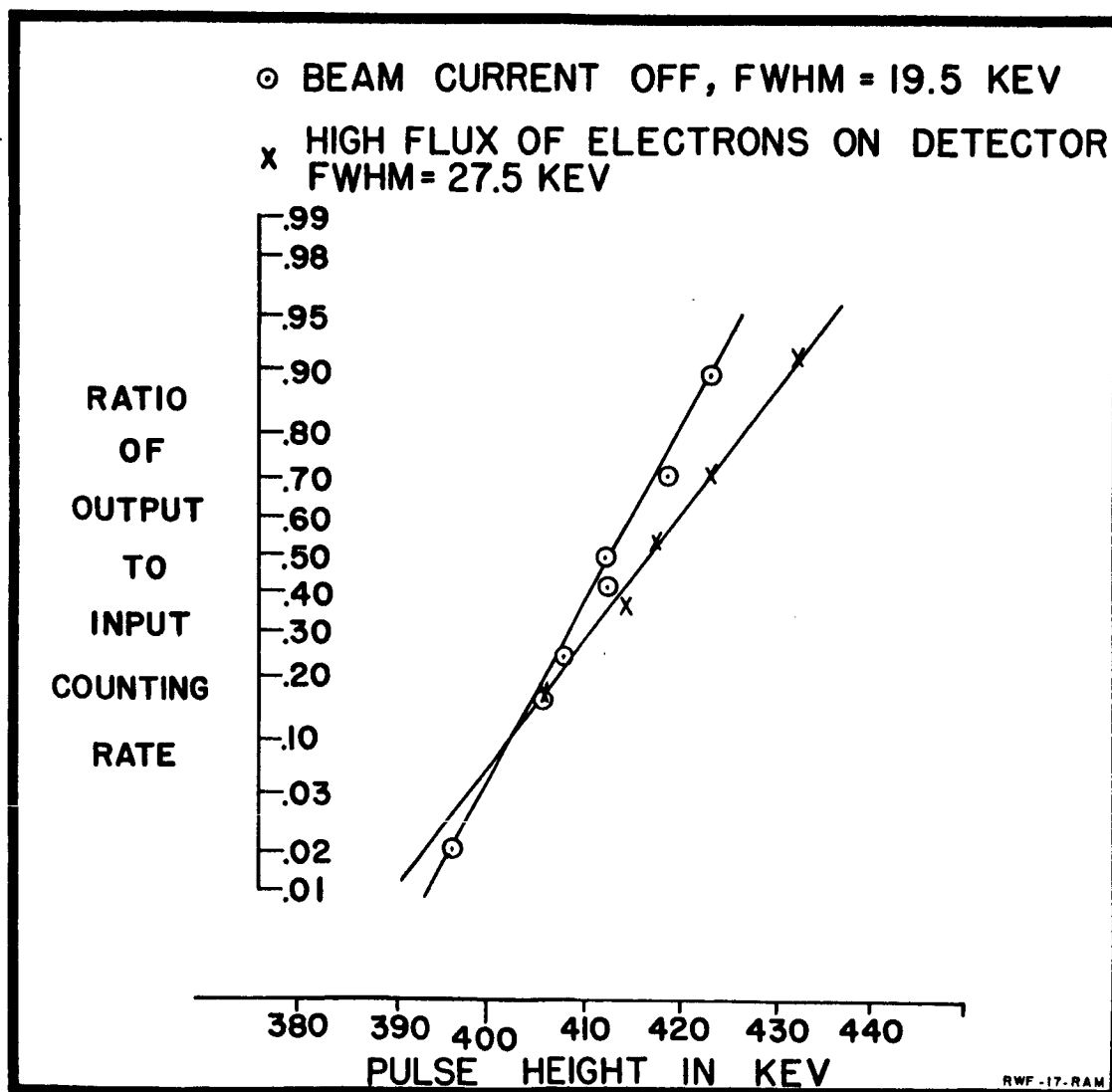


Figure 25

COMPUTED
VALUES OF
 xP_n vs x

$$x = \nu \tau$$

$$CR = \frac{1}{\tau} (xP_n)$$

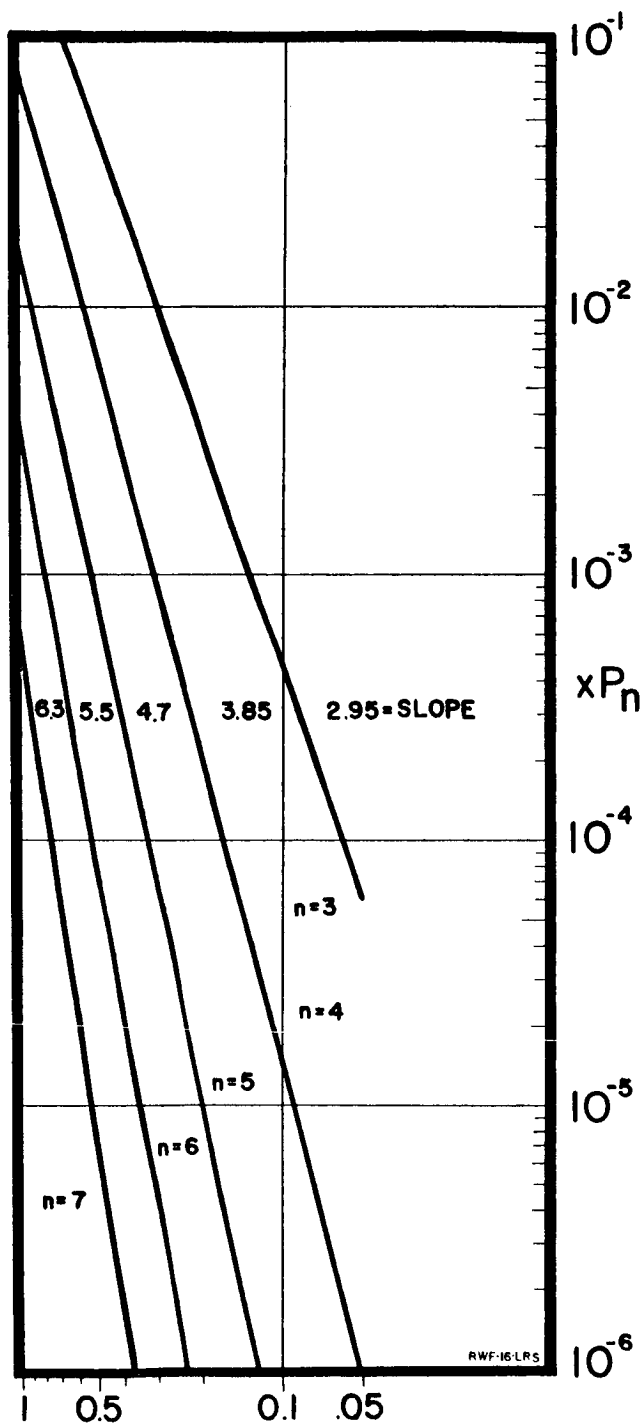


Figure 26

COUNTING RATE vs CURRENT FOR ELECTRON PILEUP

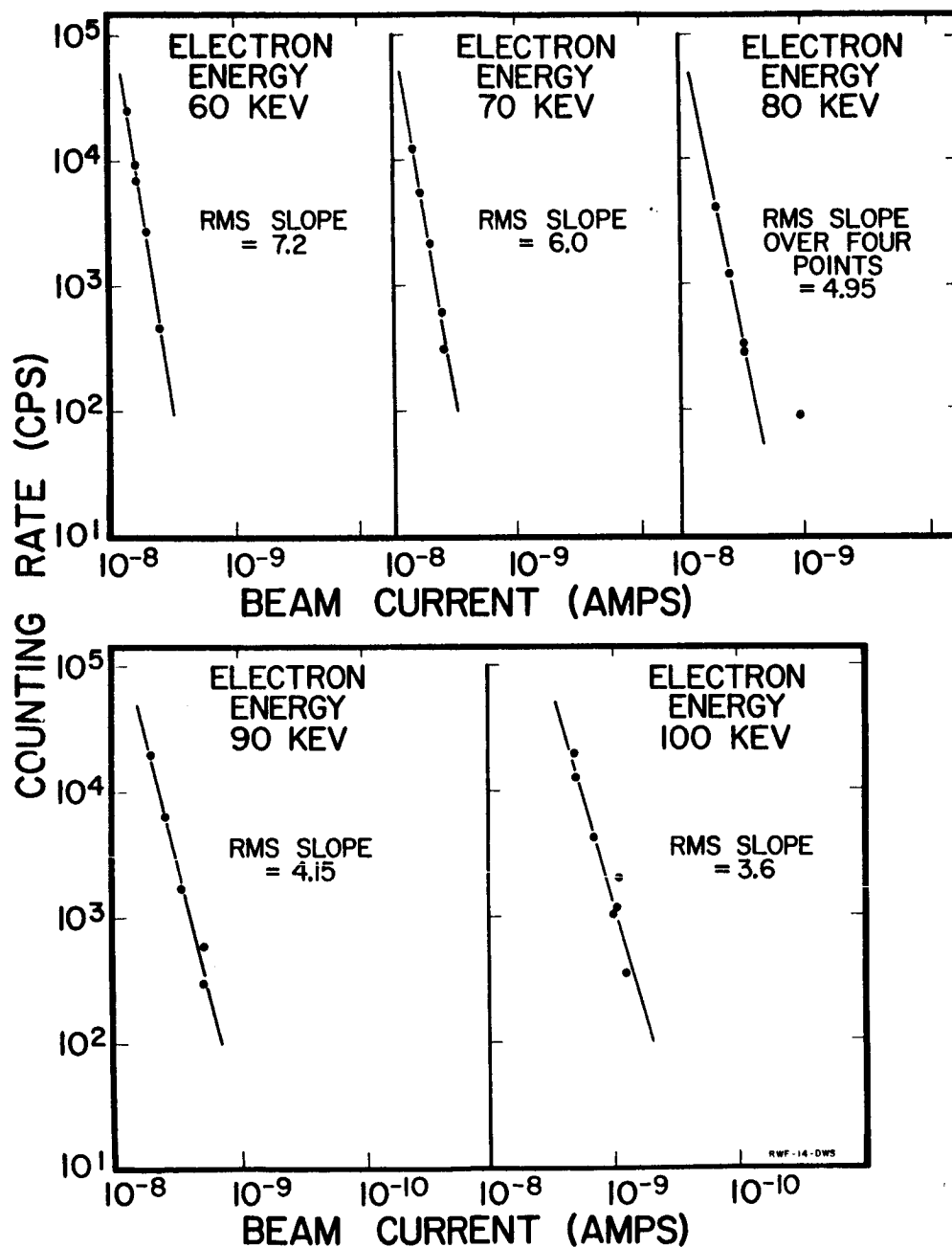
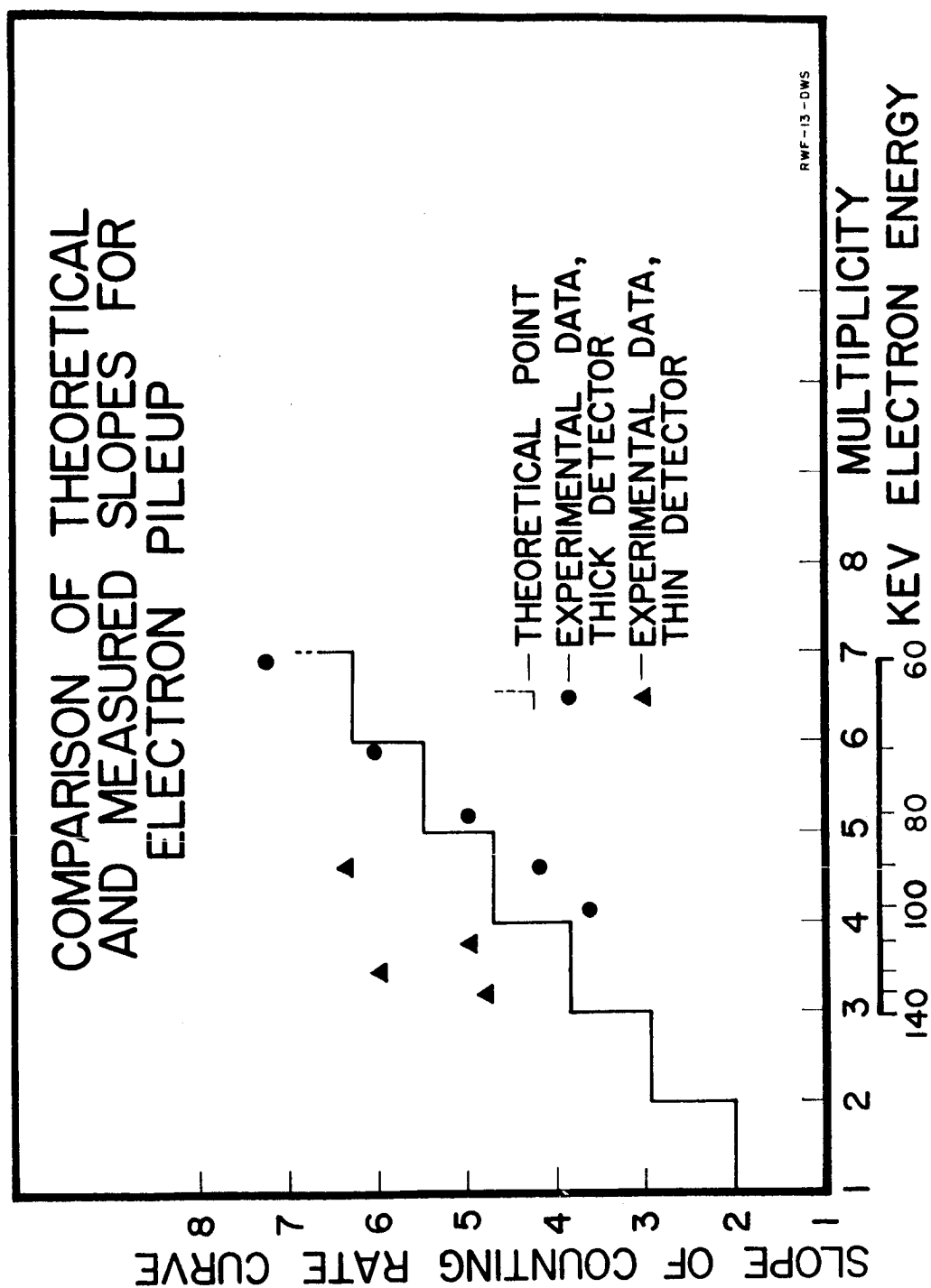


Figure 27



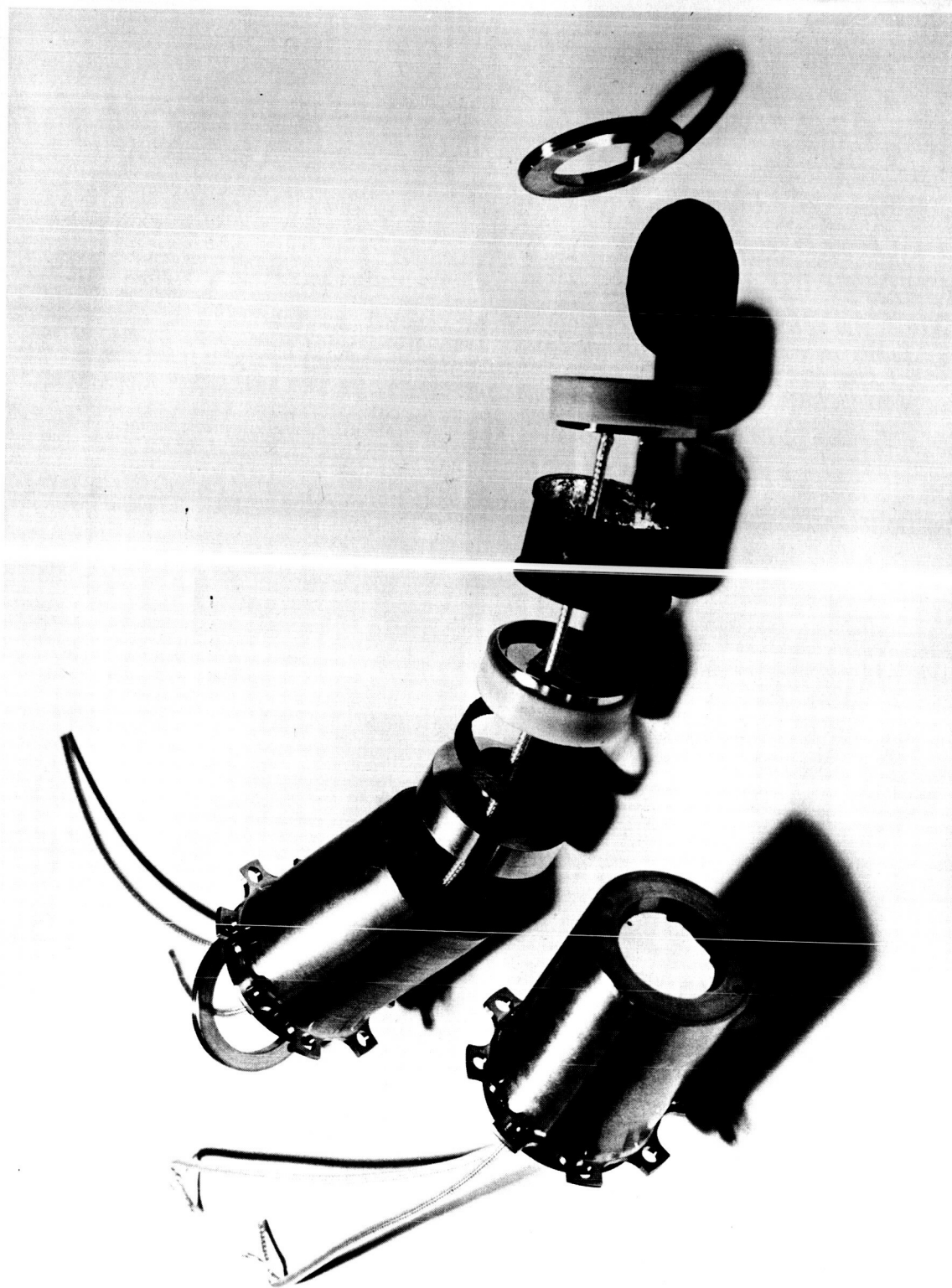


Figure 29

TELESCOPE DETECTOR C PULSE-HEIGHT CHARACTERISTICS & BLOCK LOGIC

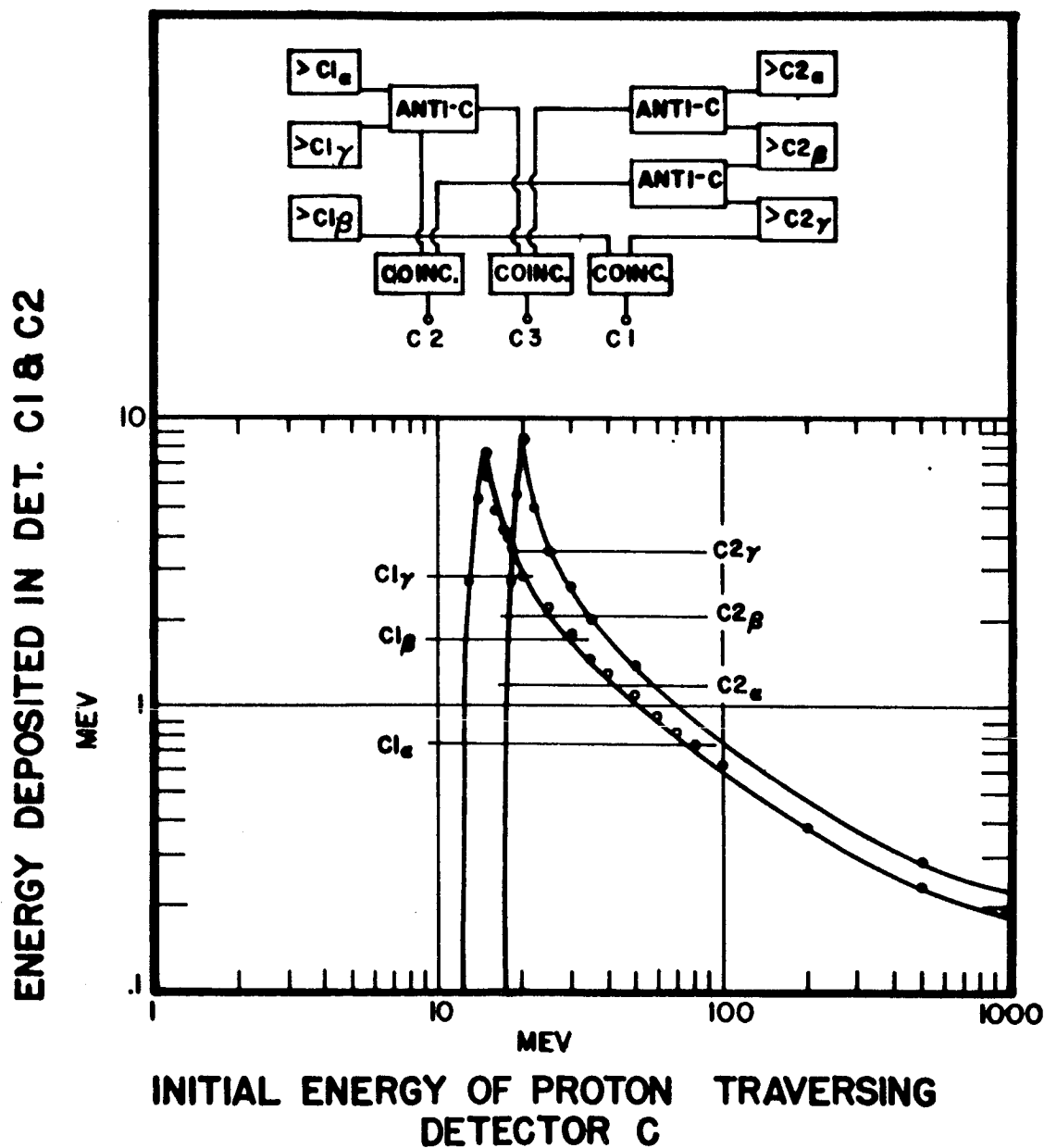


Figure 30

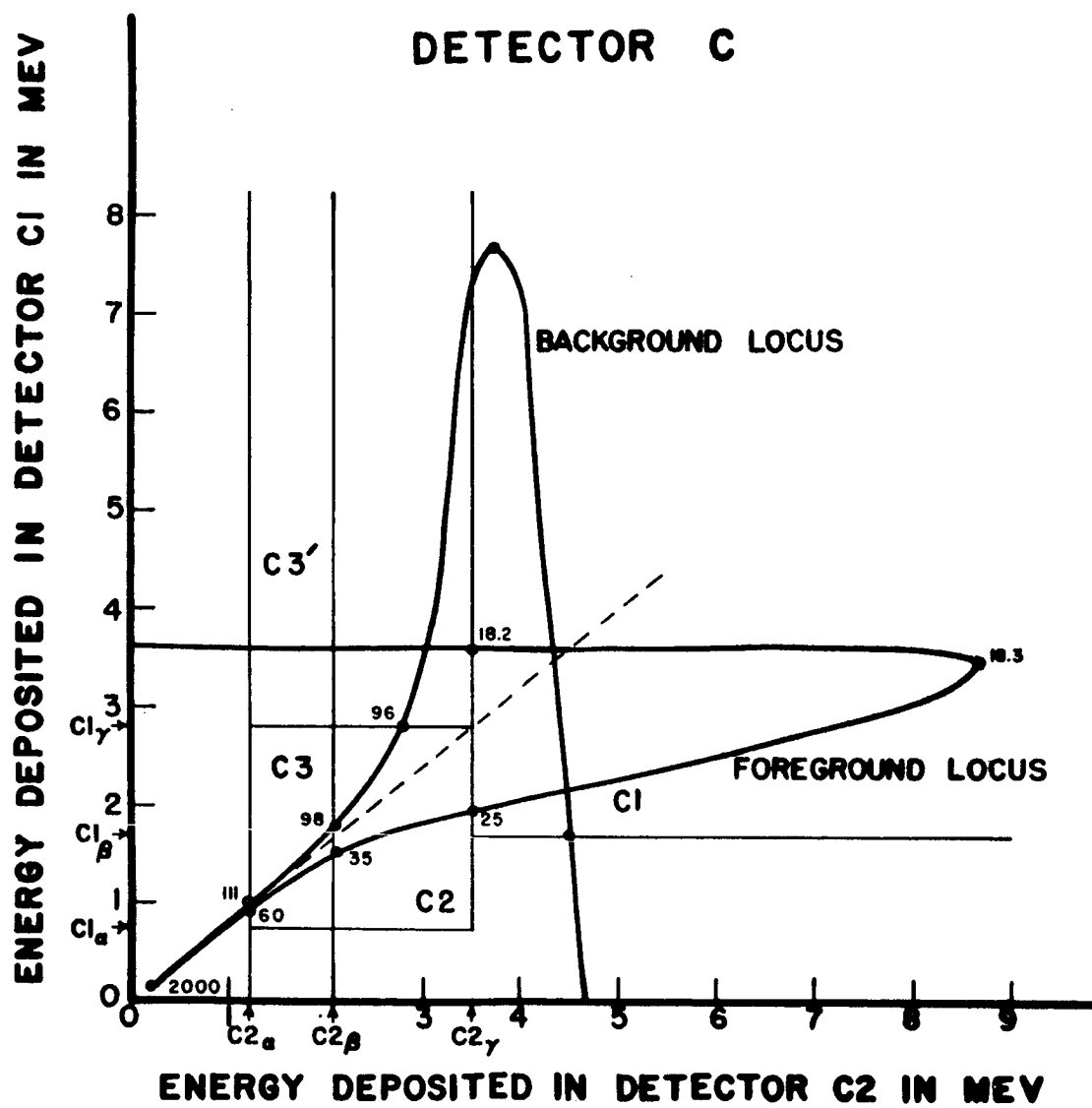
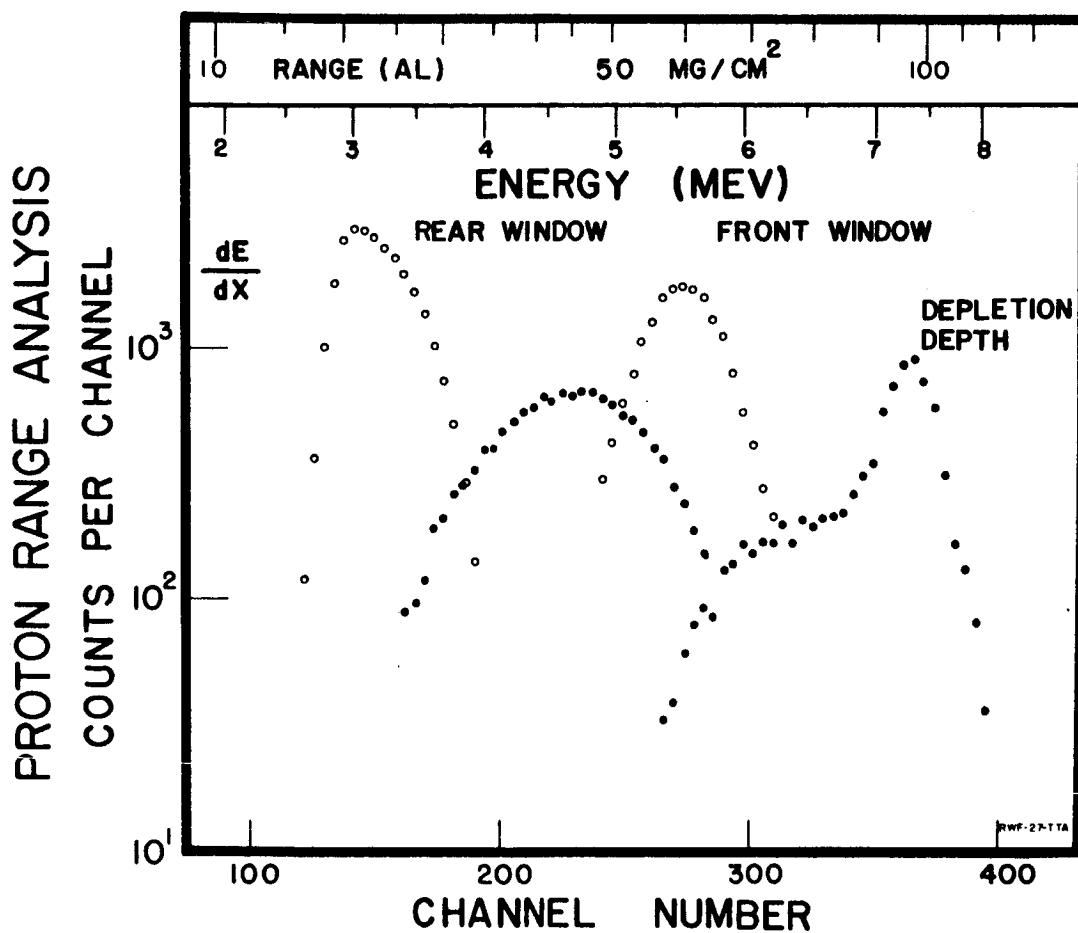


Figure 31

DETERMINATION OF LI-DRIFT DETECTOR
PARAMETERS

RELAY HIGH-ENERGY PROTON CALIBRATION GEOMETRY

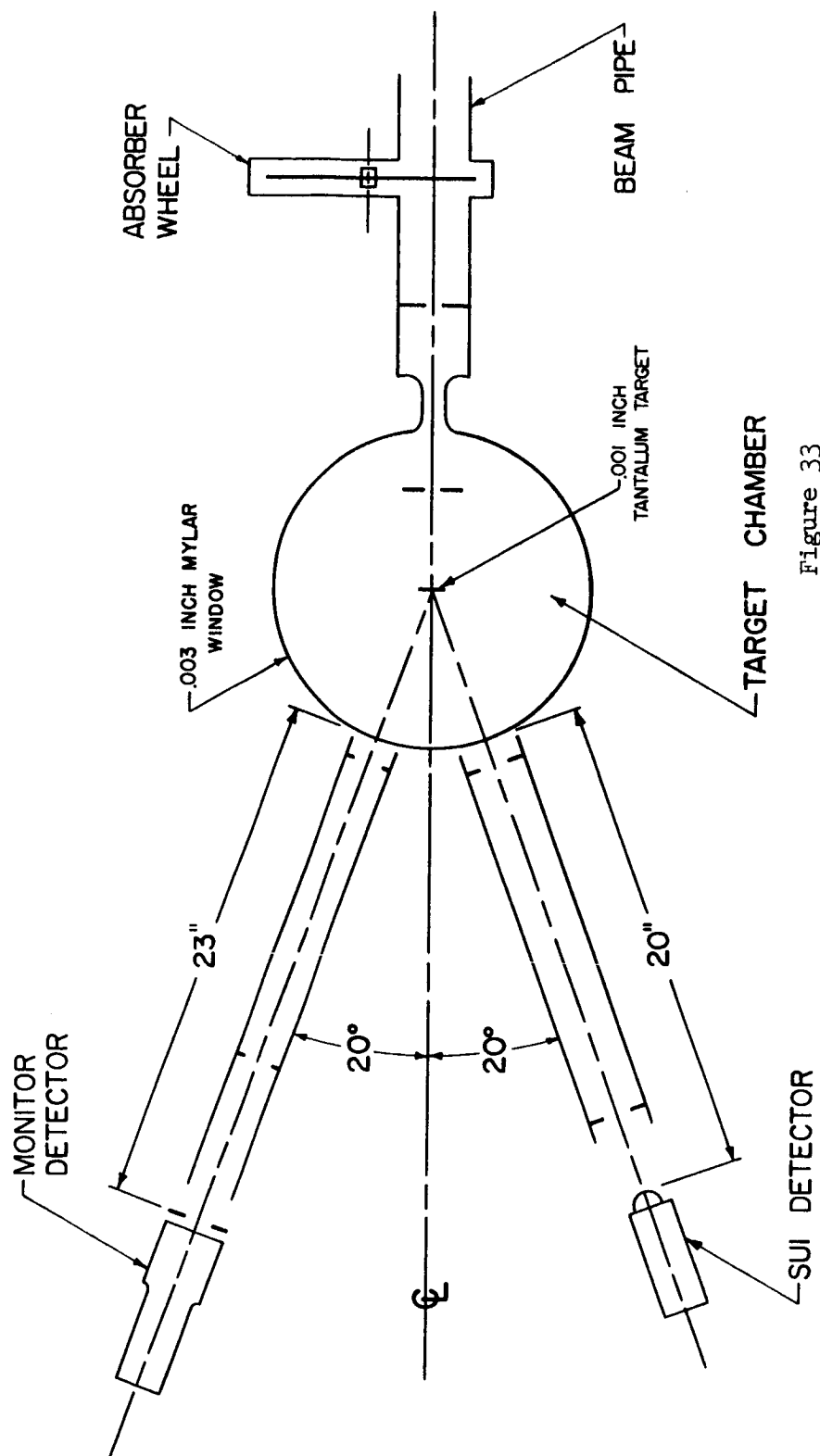


Figure 33

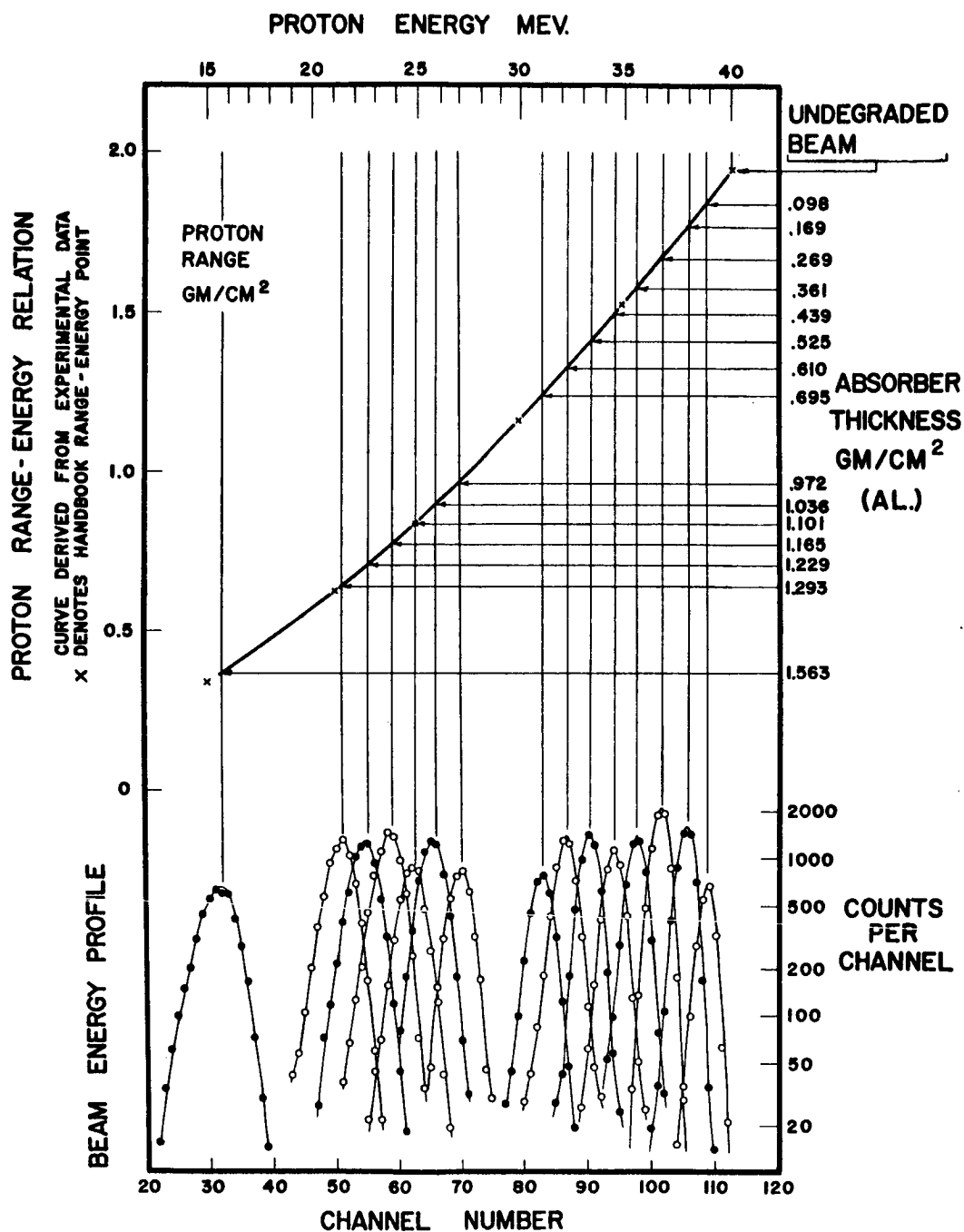


Figure 34

RELAY HIGH-ENERGY PROTON CALIBRATION

THE USE OF ABSORBERS TO DEGRADE THE
BEAM ENERGY AND THE BEAM ENERGY PROFILE
OBTAINED WITH EACH ABSORBER.

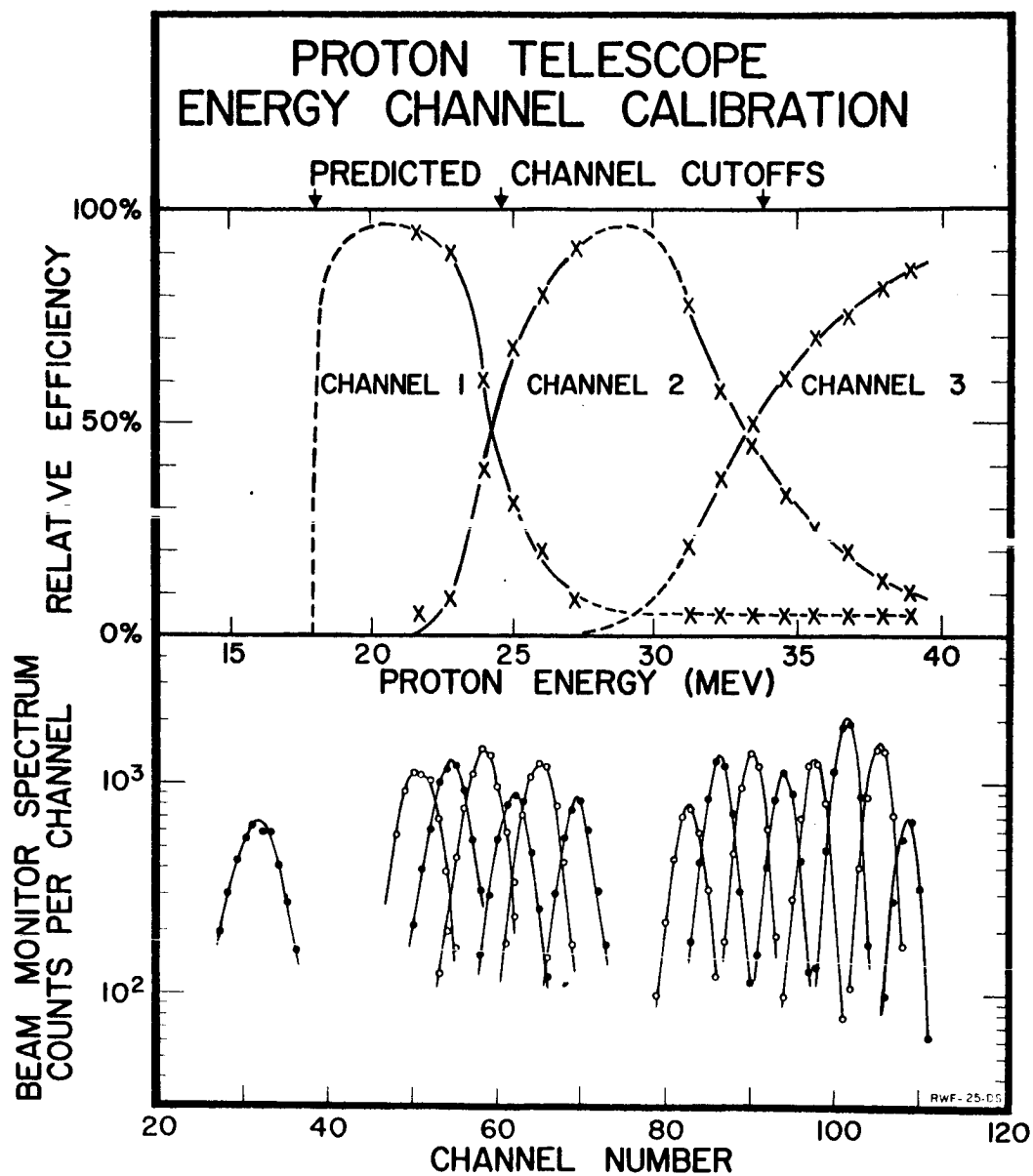


Figure 35

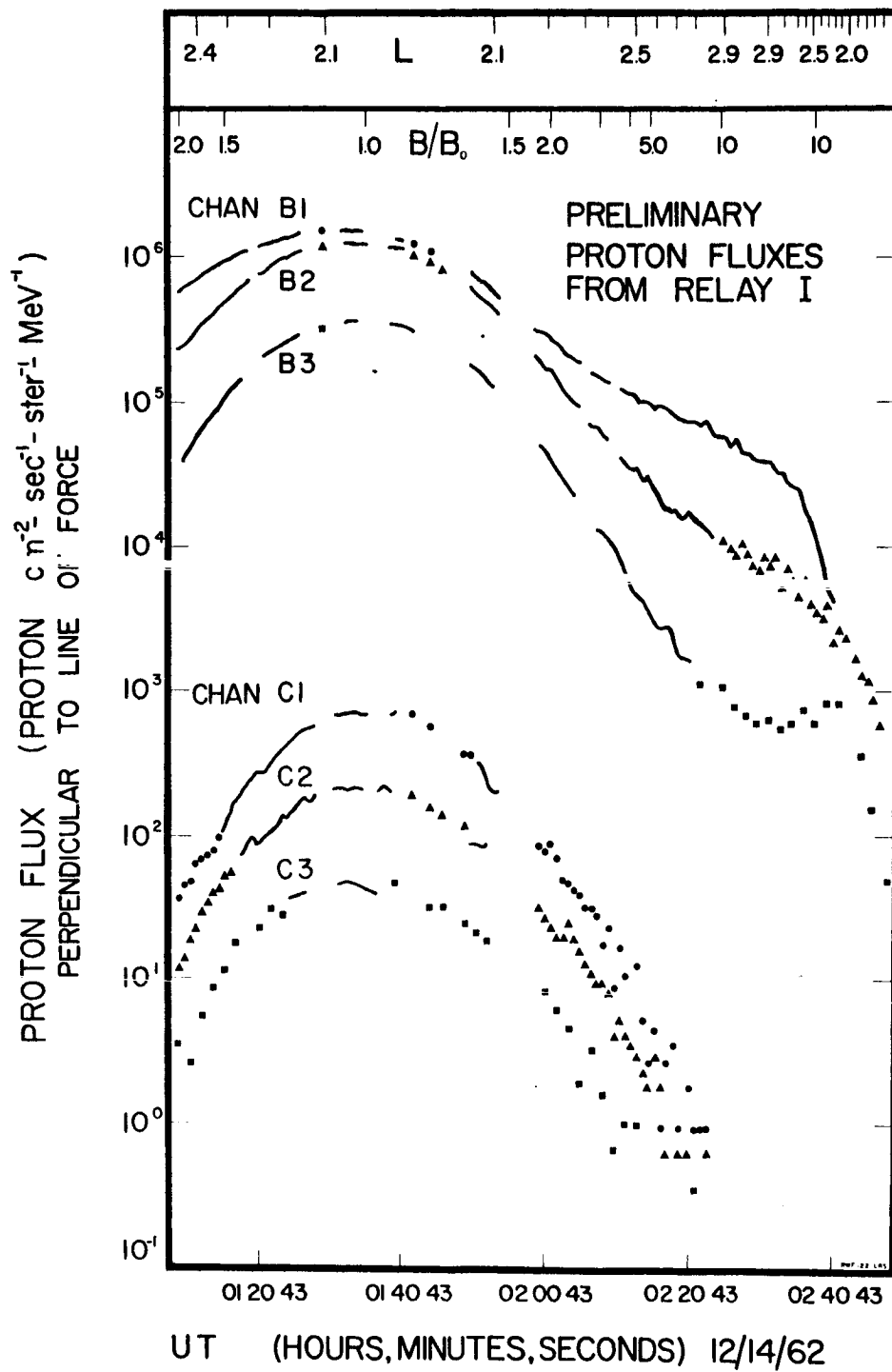


Figure 36

ENERGY SPECTRA OF TRAPPED PROTONS RELAY DETECTORS B AND C

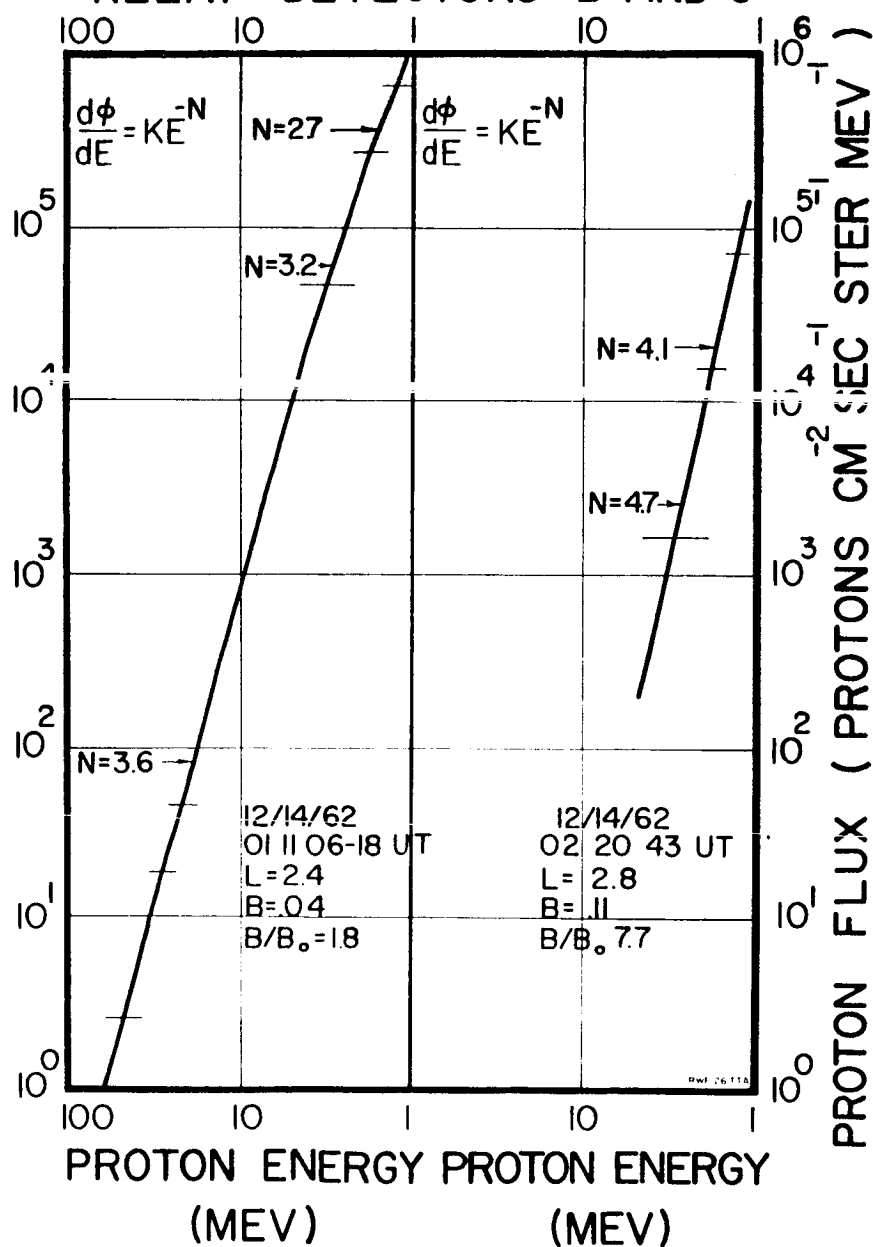


Figure 37